

**AN EDGE-BASED FINITE ELEMENT FORMULATION OF
MAGNETOHYDRODYNAMICS AT HYPERSONIC SPEEDS**

Wenbo Zhang

Department of Mechanical Engineering

McGill University, Montreal

June 2020

A thesis submitted to McGill University
in partial fulfillment of the requirements for the degree of
DOCTOR OF PHILOSOPHY

© Wenbo Zhang 2020

Preface

Chapters 1-3 and 6 is an original intellectual product of the author, Wenbo Zhang.

A version of Chapter 4 has been published as Zhang, W., Habashi, W.G., Ben Salah, N., Isola, D. and Baruzzi, G.S., Edge-based finite element formulation of hypersonic flows under an imposed magnetic field. *AIAA Journal*, 2018. 56(7): pp. 2756-2768.

A version of Chapter 5 has been published as Zhang, W., Habashi, W.G., Ben Salah, N., Isola, D. and Baruzzi, G.S., Edge-based finite element formulation of magnetohydrodynamics at high Mach numbers. *AIAA Journal*, 2019. 57(7): pp. 3003-3013.

Acknowledgements

I would like to most sincerely express my gratitude to my supervisor Prof. Wagdi G. Habashi, for his support and guidance in every aspect of my academic career throughout the PhD studies. I would like to thank Drs. Dario Isola and Guido Baruzzi, and Professors Nizar Ben Salah and Marco Fossati for extensive technical discussions. Thanks to my colleagues Drs. Song Gao and Vincent Casseau, Mr. Jory Seguin and Ms. Marie-Ève Dumas, with whom I discussed many technical problems. I would like to thank my late father Jinping Zhang, my mother Qiuling He and my wife Chu Xu. This project was financially supported by the NSERC-Lockheed Martin-Bell Industrial Research Chair for Multiphysics Analysis and Design of Aerospace Systems at the McGill CFD Lab. Compute Canada and CLUMEQ have given access to their computational resources that facilitated this work.

Table of Contents

Preface.....	II
Acknowledgements	III
Table of Contents	IV
List of Figures.....	VII
List of Tables	XII
List of Symbols	1
Abstract.....	6
Résumé.....	7
1 Introduction.....	9
1.1 Applications of Magnetogasdynamics at High Mach Numbers	9
1.2 Physical Modeling and Numerical Issues	10
1.3 Review of Related Works.....	11
1.4 Review of Numerical Approaches	14
1.5 Thesis Objectives	17
1.6 Thesis Contributions	17
1.7 Thesis Outline	18
2 Mathematical Formulation	19
2.1 Resistive MHD Model	19
2.2 Magnetic Reynolds Number Approximation	21
3 Numerical Modeling	23
3.1 Lumped Mass Matrix.....	23
3.2 Inviscid Fluxes	24
3.2.1 Viscous Fluxes.....	25
3.3 Magnetic Induction Equation (Resistive MHD Model)	25
3.4 Current Continuity Equation.....	26
3.5 Solution Strategy	28
3.6 Parallelization	28

4	Low-Magnetic Reynolds Number Formulation	30
	4.1 Code Validation for Solving the Current-Continuity Equation.....	30
	4.2 Mach 5 Inviscid Flow Past a Sphere	35
	4.3 Mach 4.75 Laminar Flow Past a Sphere.....	42
	4.4 Introducing Anisotropic Mesh Optimization.....	47
	4.5 Apollo-like Re-entry Capsule	50
	4.6 Laminar Flow over a Sphere (Mach 21.38).....	57
	4.7 Turbulent flow over Orbital Re-entry Experiment (OREX) Capsule (Mach 17.61).....	64
5	Resistive MHD Model.....	73
	5.1 Hartmann Flow.....	73
	5.2 MGD Converging Channel Accelerator	76
	5.3 2D MHD Energy Bypass Scramjet Engine (Inviscid)	79
	5.4 3D Bypass MHD Energy Bypass Scramjet Engine (Laminar).....	86
6	Conclusion and Suggested Future Development.....	91
	References	95
	Appendix A: Vector and Tensor Identities.....	101

List of Figures

Figure 1. Sequence of solutions of the segregated approach.....	28
Figure 2. MHD channel flow through singly-paired electrodes	31
Figure 3. MHD channel flow through singly-paired electrodes: electric potential (V) contours between the electrodes with $\beta = 0$	33
Figure 4. MHD channel flow through singly-paired electrodes: electric potential (V) contours between the electrodes with $\beta = 1$	33
Figure 5. MHD channel flow through singly-paired electrodes: electric potential distribution at $x = 0.05\text{m}$ with $\beta = 1$	34
Figure 6. MHD channel flow through singly-paired electrodes: convergence history for $\beta = 1, 5, 10$	34
Figure 7. Mach 5 inviscid flow past a sphere: the coarse grid (G2).....	37
Figure 8. Mach 5 inviscid flow past a sphere: comparison of static temperature across the shock wave with different meshes, expressed in Kelvins.	38
Figure 9. Mach 5 inviscid flow past a sphere: impact of correction term; static temperature profiles across the shock wave with different meshes, expressed in Kelvins.....	38
Figure 10. Mach 5 inviscid flow past a sphere: contour plots of static temperature (K) for $St = 0$ and $St = 6$	39
Figure 11. Mach 5 inviscid flow past a sphere: contour plots of pressure (Pa) for $St = 0$ and $St = 6$	39
Figure 12. Mach 5 inviscid flow past a sphere: contour plots of Mach number for $St = 0$ and $St = 6$	40
Figure 13. Mach 5 inviscid flow past a sphere: contour plots of electric potential (V) and the induced electric field (V/m) for $St = 6$	40
Figure 14. Mach 5 inviscid flow past a sphere: shock standoff distance in terms of the Stuart number, St	41
Figure 15. Mach 5 inviscid flow past a sphere: L_2 norm of residual in terms of Newton iterations $St = 6$	41
Figure 16. Grid used for the simulation of Mach 4.75 viscous flow past a sphere.....	43
Figure 17. Mach 4.75 laminar flow past a sphere: contour plots of temperature (K) at $St = 0$ and $St = 6$	44

Figure 18. Mach 4.75 laminar flow past a sphere: contour plots of pressure (Pa) at $St = 0$ and $St = 6$	44
Figure 19. Mach 4.75 laminar flow past a sphere: contour plots of Mach number at $St = 0$ and $St = 6$	44
Figure 20. Mach 4.75 laminar flow past a Sphere: contour plots of electric potential (V) and the induced electric field (V/m) for $St = 6$	45
Figure 21. Mach 4.75 laminar flow past a sphere: shock standoff distance in terms of the Stuart number, St	46
Figure 22. Mach 4.75 laminar flow past a sphere: peak heat flux in terms of the Stuart number, St	46
Figure 23. Mach 4.75 laminar flow past a Sphere: L_2 norm of residual in terms of Newton iterations.....	47
Figure 24. Arbitrary grid of a box (left); optimized grid based on a solution with uniform second order derivative (right).....	49
Figure 25. Apollo-like re-entry capsule: schematic drawing of the outer mold line of AS-202 ..	50
Figure 26. Apollo-like re-entry capsule: initial mesh (left) and optimal one (right) after 4 adaptation cycles, $St = 0$	52
Figure 27. Apollo-like re-entry capsule: contour plots of temperature for $St = 0$, with the initial mesh (left) and with the adapted one (right), expressed in Kelvins.....	52
Figure 28. Apollo-like re-entry capsule: adapted meshes after 4 adaptation cycles for $St = 0$ (left) and $St = 6$ (right).....	53
Figure 29. Apollo-like re-entry capsule: contour plots of temperature for $St = 6$, with the initial mesh (left) and with the adapted one (right), expressed in Kelvin.	54
Figure 30. Apollo-like re-entry capsule: contour plots of pressure (Pa, left) and Mach number (right) for $St = 6$	54
Figure 31. Apollo-like re-entry capsule: static temperature across the shock wave, expressed in Kelvins.....	55
Figure 32. Apollo-like re-entry capsule: shock standoff distance in terms of the Stuart number St for the Apollo capsule.....	56
Figure 33. Apollo-like re-entry capsule: peak heat flux in terms of the Stuart number St for the Apollo capsule..	56

Figure 34. Apollo-like re-entry capsule: L_2 norm of residual in terms of Newton iterations.....	57
Figure 35. Mach 21.38 viscous flow over a sphere: convergence of Mach number along stagnation line during mesh optimization (Case 3).....	58
Figure 36. Mach 21.38 viscous flow over a sphere: resulting meshes with different optimization strategies: (a) Original mesh; (b) Case 1 (flow only); (c) Case 2 (EM only); (d) Case 3 (flow+EM)	59
Figure 37. Mach 21.38 viscous flow over a sphere: pressure contours (Pa) obtained from original and optimized meshes: (a) Original mesh; (b) Case 1 (flow only); (c) Case 2 (EM only); (d) Case 3 (flow+EM).. ..	61
Figure 38. Mach 21.38 viscous flow over a sphere, electric potential (V) contours from original and optimized meshes: (a) Original mesh; (b) Case 1 (flow only); (c) Case 2 (EM only); (d) Case 3 (flow+EM)	62
Figure 39. Mach 21.38 viscous flow over a sphere, Mach number contours from original and optimized meshes: (a) Original mesh; (b) Case 1 (flow only); (c) Case 2 (EM only); (d) Case 3 (flow+EM).	63
Figure 40. Mach 21.38 viscous flow over a sphere: (a) Electric potential and (b) Mach number distributions along stagnation line.	64
Figure 41. OREX geometry and computational domain.	65
Figure 42. Viscous flow over OREX capsule: convergence of Mach number along stagnation line (line-A in Figure 13) during mesh optimization (Case 3).....	66
Figure 43. Viscous flow over OREX capsule, velocity vectors from original and optimized meshes: (a) Original mesh; (b) Case 1 (flow only); (c) Case 2 (EM only); (d) Case 3 (flow+EM).	67
Figure 44. Viscous flow over OREX capsule, meshes with different optimization strategies: (a) Original mesh; (b) Case 1 (flow only); (c) Case 2 (EM only); (d) Case 3 (flow+EM).. ..	69
Figure 45. Viscous flow over OREX capsule, electric potential (V) contours from original and optimized meshes: (a) Original mesh; (b) Case 1 (flow only); (c) Case 2 (EM only); (d) Case 3 (flow+EM).	70
Figure 46. Viscous flow over OREX capsule, Mach number contours from original and optimized meshes: (a) Original mesh; (b) Case 1(flow only); (c) Case 2 (EM only); (d) Case 3 (flow+EM)	71

Figure 47. Viscous flow over OREX capsule: (a) Mach number distribution along stagnation line (line-A in Figure 39); (b) Electric potential distribution along $y=1.1$ m, $z=0$ m (line-B in Figure 39).	72
Figure 48. Sketch of the Hartmann flow configuration	73
Figure 49. Hartmann flow inside a two-dimensional channel: velocity for different Hartmann numbers and unitary magnetic Reynolds number at $x = 45$ m.	75
Figure 50. Hartmann flow inside a two-dimensional channel: induced magnetic field for different Hartmann numbers and unitary magnetic Reynolds number at $x = 45$ m.	75
Figure 51. Sketch of the converging channel accelerator	76
Figure 52. MGD converging channel accelerator: x-component of the induced magnetic field (T) b_x .	77
Figure 53. MGD converging channel accelerator: y-component of the induced magnetic field (T) b_y .	77
Figure 54. MGD converging channel accelerator: pressure (in Pa) contours.	78
Figure 55. MGD converging channel accelerator: Mach number contours.	78
Figure 56. MGD converging channel accelerator: x component of the velocity u/u_0 along the centerline $y = 0$.	79
Figure 57. Sketch of the simplified MHD energy bypass scramjet engine with the applied electro/magnetic fields.	80
Figure 58. 2D MHD energy bypass scramjet engine: the distribution of the imposed magnetic field (top) and the imposed electric field (bottom) along the x axis.	80
Figure 59. 2D MHD energy bypass scramjet engine: initial mesh and adapted one (Optimization Case 2) after 5 adaptation cycles.	82
Figure 60. 2D MHD energy bypass scramjet engine: the pressure profile along the horizontal axis $y = 0.4$ m.	82
Figure 61. 2D MHD energy bypass scramjet engine: Mach number contours for the scramjet with the initial mesh (top) and adapted (bottom).	84
Figure 62. 2D MHD energy bypass scramjet engine: pressure (Pa) contours for the scramjet with the adapted mesh.	84
Figure 63. 2D MHD energy bypass scramjet engine: x-component of the induced magnetic field (T) b_x for the MHD energy bypass scramjet engine.	85

Figure 64. 2D MHD energy bypass scramjet engine: y-component of the induced magnetic field (T) b_y for the MHD energy bypass scramjet engine.....	86
Figure 65. 2D MHD energy bypass scramjet engine: estimated error contours with the initial (top) and adapted (bottom) meshes.....	86
Figure 66. 3D MHD energy bypass scramjet engine: initial mesh and adapted one after 3 adaptation cycles.....	87
Figure 67. 3D MHD energy bypass scramjet engine: Mach number contours in the cross section $z = 0$ m for the scramjet with the initial mesh (top) and adapted mesh (bottom).....	88
Figure 68. 3D MHD energy bypass scramjet engine: pressure profile along the horizontal axis $y = 0.40$ m.....	89
Figure 69. 3D MHD energy bypass scramjet engine: pressure contours in the cross section $z = 0$ m; top: 2D with adapted mesh (Optimization Case 2), bottom: 3D with adapted mesh.....	89
Figure 70. 3D MHD energy bypass scramjet engine: x-component of the induced magnetic field (T) b_x for the MHD energy bypass scramjet engine.....	90
Figure 71. 3D MHD energy bypass scramjet engine: y-component of the induced magnetic field (T) b_y for the MHD energy bypass scramjet engine.....	90

List of Tables

Table 1. Strength of the applied dipole for Mach 5 inviscid flow over a sphere.....	35
Table 2. Strength of the applied dipole for Mach 4.75 laminar flow over a sphere	43
Table 3. Mach 21.38 laminar flow over a sphere, mesh adaptation setup	58
Table 4. Turbulent flow over OREX capsule, mesh adaptation setup.....	66
Table 5. 2D MHD energy bypass scramjet engine, the mesh-optimization cases	81
Table 6. Normalized thrust at the exit of the 3D MHD energy bypass scramjet engine for different meshes.	83

List of Symbols

English letters

\mathbf{A}	Jacobian matrix
\mathbf{B}	Total magnetic field (T)
\mathbf{B}_0	Imposed magnetic field (T)
B_0	Magnitude of imposed magnetic field (T)
\mathbf{b}	Induced magnetic field (T)
BT	Boundary term
CT	Edge-based correction of the Laplacian term
\mathbf{d}_{ij}	Edge coefficients
\mathbf{d}_{ij}^A	Anti-symmetric part of \mathbf{d}_{ij}
\mathbf{d}_{ij}^S	Symmetric part of \mathbf{d}_{ij}
\mathbf{E}	Electric field (V/m)
\mathbf{E}_0	Imposed electric field (V/m)
E_i	Set of elements sharing the i -th vertex
e_t	Total energy per unit mass
$error_{rel}$	Square root of the machine precision
F_i	Set of boundary faces sharing the i -th vertex
\mathbf{F}^A	Inviscid flux vector
\mathbf{f}^L	Lorenz force
F_x^A	Inviscid flux in x direction
F_y^A	Inviscid flux in y direction
F_z^A	Inviscid flux in z direction
\tilde{F}_x^A	Inviscid flux of momentum equation in x direction
\mathbf{F}^V	Viscous flux vector
\mathbf{F}^B	Short-hand for $\mathbf{V} \times \mathbf{B}$ (T·m/s)
\mathbf{F}^{EA}	Short-hand for $\boldsymbol{\sigma}^A \cdot \nabla \phi$
F_x^V	Viscous flux vector in x direction
F_y^V	Viscous flux vector in y direction

F_z^V	Viscous flux vector in z direction
\mathbf{F}_{ij}^V	Viscous flux between node i and node j
G_e	Set of Gauss integration points belonging to the e -th element
H_{ij}	Consistent mass matrix correction term for i -th and j -th vertices
h	Half of channel height in Hartmann flow (m)
\mathbf{I}	Identity tensor
\mathbf{j}	electric current density (A/m ²)
K_e	Set of nodes of the e -th element
K_i	Set of nodes connected to i -th vertex
l	Characteristic length (m)
L_i	Lumped mass matrix for i -th vertex
$\hat{\mathbf{m}}$	Magnetic dipole moment (J/T)
m_e	Mass of a single electron
N_G	Total number of nodes in the grid
\mathbf{n}	Normal unit vector
N_i	Linear Lagrangian shape function
n_e	Electron number density
p	Total pressure
Q	Conservative variables vector
ΔQ	Update of conservative variables vector
\mathbf{q}	Heat flux vector (W/m ²)
\mathbf{R}	Residual vector
$\tilde{\mathbf{R}}$	Low-order approximation of the residual
\mathbf{S}^L	Electromagnetic source term
T	Temperature (K)
t	Physical time (s)
T_w	Wall temperature (K)
U^*	x component of the non-dimensional velocity of Hartmann flow
u	Velocity component in x direction
u_M	x component of Hartmann flow velocity along channel axis

V^e	Volume of e -th element
V	Entire volume domain
\mathbf{V}	Velocity
V_0	Characteristic velocity (m/s)
v	Velocity component in y direction
W_i	Linear Lagrangian test function
w	Velocity component in z direction
x_g	Coordinates of Gauss points
\mathbf{x}_i	Coordinates of node i

Greek letters

β	Hall parameter
ε	Elemental charge
$\boldsymbol{\eta}_{ij}$	Edge coefficients
μ	Mixture viscosity
μ_0	Vacuum magnetic permeability (H/m)
μ_T	Turbulent viscosity (kg/m·s)
ν	Magnetic diffusivity (m ² /s)
ν_m	Electron-neutral particle momentum transfer collision frequency
ξ_i	Nodal boundary coefficient
ρ	Mixture density
Ω	Computational domain
γ	Gas heat capacity ratio
σ	Electrical conductivity (S/m)
$\boldsymbol{\sigma}$	Tensor electrical conductivity (S/m)
$\boldsymbol{\tau}$	Viscous stress tensor
$\Delta\tau$	Pseudo-time step
Φ^{num}	Numerical flux at edge ij midpoint
ϕ	Electric potential (V)
$\boldsymbol{\chi}_{ij}$	Edge coefficients
ω	Gauss weight

Non-Dimensional Numbers

Re	Flow Reynolds number
Re_m	Magnetic Reynolds number
Kn	Knudsen number
Mach	Mach number
CFL	Courant-Friedrichs-Lewy number
St	Stuart (magnetic interaction) number
Ha	Hartmann number

Abbreviations

AUSM	Advection Upstream Splitting Method
CFD	Computational Fluid Dynamics
EM	Electro-Magnetic
FEM	Finite Element Method
FMFD	Full Magnetofluid Dynamics
FVM	Finite Volume Method
HALO3D	High Altitude Low Orbit 3D Code
HLL	Harten-Lax-Van Leer
ILU	Incomplete LU Factorization
LeMANS	Michigan Aerothermodynamic Navier-Stokes Solver
MGD	Magnetogasdynamics
MHD	Magnetohydrodynamics
MPD	Magnetoplasmdynamics
MPI	Message Passing Interface
MUSCL	Monotonic Upstream-centered Scheme for Conservation Laws
OREX	Orbital Re-entry Experiment
PETSc	Portable, Extensible Toolkit for Scientific Computation
PISO	Pressure-Implicit with Splitting of Operators
LHS	Left-hand side
RANS	Reynolds-Averaged Navier-Stokes
RCM	Reverse Cuthill-McKee

RHS	Right-hand side
TPS	Thermal Protection System
TVD	Total Variation Diminishing

Abstract

This thesis presents an edge-based FE solver for magnetohydrodynamic (MHD) problems. It is considered a major building block of HALO3D (High Altitude Low Orbit 3D), a Finite Element Method (FEM) hypersonic flows solver developed at the McGill CFD Lab under an NSERC Industrial Chair. Two formulations are implemented with their applicability gauged by the magnetic Reynolds number. The resistive MHD model is presented as a coupled system, composed of the Reynolds-Averaged Navier-Stokes (RANS) equations and the magnetic induction equation, while the low-magnetic Reynolds number formulation neglects the induced magnetic field and replaces the magnetic induction equation with the current-continuity equation cast in terms of a scalar electric potential. The anisotropic Hall effect is introduced through an asymmetric electrical conductivity tensor. For both formulations, the spatial discretization uses an edge-based FE formulation with stabilization achieved through a Roe scheme, on both structured and unstructured grids. The steady-state solution is obtained by an implicit integration in time. A loosely-coupled strategy is used in which each of the systems is solved separately via a generalized minimal residual (GMRES) method with an incomplete LU factorization (ILU) preconditioner. Calculation of flow through segmented electrodes and external flow past spheres, over an Apollo-like re-entry capsule and the OREX re-entry vehicle are carried out to assess the accuracy and efficiency of the low-magnetic Reynolds number formulation. The resistive MHD model is validated by the Hartmann flow and by inviscid and viscous flows through an MHD accelerator and a scramjet engine. Good agreement is demonstrated with experimental and other numerical data in the literature. The 3D unstructured hybrid meshes used in these cases are optimized with a highly anisotropic methodology based on the Hessian of the solution, using multi-physics combined adaptation criteria such as density, pressure, temperature, velocity, turbulent viscosity and the electric potential/induced magnetic field. Unlike uniform mesh refinement or gradient-based mesh enrichment, this approach greatly improves accuracy without increasing mesh size. The improvement is so dramatic that it could even be concluded that calculations of hypersonic flows over complex geometries carried out without mesh optimization, preferably anisotropic, could yield doubtful results.

Résumé

Cette thèse s'inscrit comme la composante magnétohydrodynamique du solveur hypersonique HALO3D (High Altitude Low Orbit 3D), développé au Laboratoire CFD de McGill sous l'égide d'une chaire industrielle du CSRNG. Deux approches ont été implémentées et leur domaine de validité respectif est déterminé par le nombre de Reynolds magnétique. Le modèle de la MHD résistive est introduit comme un système d'équations couplées, composé des équations Navier-Stokes moyennées par Reynolds (RANS) et de l'équation d'induction. La formulation dite à faible nombre de Reynolds magnétique néglige le champ magnétique induit et remplace l'équation de l'induction par l'équation de continuité du courant, écrite en termes de champ de gradient. De plus, l'effet de Hall, intrinsèquement non-isotrope, est introduit à l'aide du tenseur asymétrique de la conductivité électrique. La discrétisation spatiale pour des maillages structurés ou non-structurés est réalisée avec une formulation FEM par arêtes, stabilisée avec le schéma de Roe. La solution stationnaire est quant à elle obtenue par une intégration temporelle implicite. Une stratégie dite de couplage faible est employée dans laquelle chaque système est résolu séparément par minimisation du résidu (GMRES) avec un pré-conditionneur par factorisation incomplète (ILU). Des simulations numériques mettant en jeu des écoulements internes à travers des électrodes segmentées et des écoulements externes autour d'une sphère, d'une capsule de réentrée atmosphérique de type Apollo et du véhicule OREX, sont effectuées pour évaluer la précision et la performance de la formulation à faible nombre de Reynolds magnétique. Le modèle de la MHD résistive est également validé pour un écoulement de Hartmann et des écoulements visqueux et non-visqueux à travers un accélérateur MHD et un statoréacteur à combustion supersonique. Un bon accord est obtenu avec les solutions disponibles dans la littérature. Les maillages hybrides 3D non-structurés utilisés pour ces simulations sont optimisés sur la base des matrices Hessiennes de la solution, ce qui leur confère un caractère très anisotrope. Les critères d'adaptation multi-physiques utilisés sont les champs de densité, pression, température, vitesse, viscosité turbulente, et potentiel électrique / champ magnétique induit. À l'inverse des méthodes de raffinement adaptées aux maillages uniformes ou basées sur le gradient des champs, cette approche améliore grandement la précision des calculs sans pour autant augmenter le nombre de points du maillage. L'amélioration des résultats est telle que l'on pourrait même conclure que tout calcul hypersonique autour de formes

complexes n'utilisant pas de maillage adaptatif, préférablement anisotrope, donnerait des résultats douteux.

1 Introduction

1.1 Applications of Magnetogasdynamics at High Mach Numbers

Commercial space flight is witnessing a resurgence of interest in utilizing devices based on magnetogasdynamics (MGD) to manage the stability and control of futuristic hypersonic aircraft (*e.g.* aerodynamic control, drag reduction, communication, thermal protection, *etc.*) [1-3]. During atmospheric re-entry, extremely high temperatures trigger dissociation and ionization of the air as it traverses the bow shock in front of the vehicle. The ionization makes the adoption of electromagnetic technologies very effective in improving aerodynamic performance and reducing heat fluxes in this flight regime. The Thermal Protection System (TPS) of re-entry vehicles is perhaps the most important application [4], protecting the craft's structure from thermal damage [5]. At the basis of these technologies, there is the application of a magnetic field to the conductive shock layer such that the Lorentz force will directly impact the aerothermodynamic interaction between the gas and the aircraft. The Lorentz force opposes the fluid motion across magnetic field lines, and by slowing down the flow near the body, reduces skin friction and heat transfer near the stagnation point. This idea, called MHD-heat shield, was proposed in the 1950s in the midst of the space race [6]. Numerous concepts emerged including large-scale self-powered MGD configurations that would reduce the overall heat load of re-entry vehicles [7], hypersonic flow control utilizing asymmetric forces [8] or Hall effects [7], and heat transfer mitigation combining ablation and electromagnetic mechanisms [9]. Enthusiasm for practical electromagnetic TPS waned in the 70s as it was concluded that the magnetic field strength required to address flows with low conductivity levels called for a magnet that was not efficient in terms of weight when compared to other cooling systems [10]. In the last five decades, tremendous advances in the area of flight-weight MHD technologies, especially those related to superconducting magnets and artificial electrical conductivity enhancement, have brought these techniques back to the sight of the aerospace community. Recently, an alternative approach called Electron Transpiration Cooling (ETC) [11], utilizing thermionic materials that emit electrons, was proposed to potentially induce a cooling effect most effective in protecting against elevated convective heating rates.

Another application category is drag reduction and aerodynamic control [12]. While the most desirable geometries for hypersonic vehicles are long thin bodies with sharp leading edges,

manufacturing risk and availability of suitable thermal protection materials greatly limit their applicability [13]. Blunting the leading edge can circumvent these difficulties, but leads to a much larger wave drag [14]. Advances in MHD technologies demonstrated promises in reducing drag on blunt nose bodies by utilizing plasma injection [15]. Conventional aerodynamic control is achieved by means of mechanically driven control surfaces (flaps) the movement of which is limited because of the interfering bow shock surrounding the vehicles. Plasma actuators provide possibilities in tackling these problems since they have no moving parts and can easily be switched on and off. These advantages motivated explorations of plasma actuators in various hypersonic configurations to provide steering moments [16, 17], control of flow separation [18], and local heat mitigation [19].

Many research efforts have also been dedicated to MGD-based propulsion systems. In these systems, the presence of an externally applied electric field creates the circulation of an electric current and produces a Lorentz force that accelerates the propulsion agent exiting the device through interactions with the imposed magnetic field [20]. Among various ideas in the context of MGD-based propulsion devices, the concept of MHD energy bypass scramjet engine has drawn the attention of the scientific community since it has the potential of expanding the Mach number envelope of traditional engines and enhance the performance of scramjet combustors [21]. Other research activities in this area include MHD blackout prevention [22] and MHD power extraction [23].

The above-mentioned applications typically involve complex physical phenomena due to high kinetic energy and the existence of charged particles. To fully understand the hypersonic flow regime, it is necessary to perform a comprehensive study of the physics behind it.

1.2 Physical Modeling and Numerical Issues

The most complete model used in MGD simulations for aerospace applications consists of the Maxwell equations coupled with the mass, momentum and energy conservation equations for an electrically conducting fluid subject to an electromagnetic field. This model is referred to as the full magnetofluid dynamics (FMFD) equations [23, 24]. Simplifying the FMFD system by enforcing the MHD assumptions (based on the assumption of negligible displacement current, negligible convection current and applicability of the generalized Ohm's law), one obtains the (resistive) MHD equations. In the MHD model, the diffusive-convective magnetic induction equation takes the place of the Maxwell equations. Dropping the displacement current from the

FMFD system effectively renders the electromagnetic and flow timescales comparable with the consequent MHD model being significantly less stiff [25]. Solving the MHD equations is, however, still not a straightforward task at low levels of electrical conductivity (which is usually the case for aerodynamic applications), even for two-dimensional or axisymmetric configurations [26]. It is the diffusion term in the magnetic induction equation that causes severe numerical difficulties at low levels of ionization, since magnetic diffusivity is inversely proportional to electrical conductivity. As a result, the order of magnitude of the diffusion term is much larger than other terms of the induction equation, necessitating small Courant-Friedrichs-Lewy (CFL) numbers.

Most computational work in this area makes use of the low-magnetic Reynolds number approximation that prevails in common aerodynamic applications. In this formulation, the magnetic induction equation is omitted by noting that the induced magnetic field associated with the induced current density is negligible compared to the imposed magnetic field. In cases where the electric field is known or trivial, a further simplification can be made that reduces the system to source terms added in the Navier-Stokes equations. However, it is necessary in general to obtain the electric field appearing in Ohm's law for the current in a self-consistent manner by solving the current continuity equation [2]. Thus, the low-magnetic Reynolds number formulation eases the trouble of dealing with the extreme stiffness of the complete Maxwell equations, but also shows limited applicability.

In the simpler case with constant electrical conductivity, the current continuity equation reduces to a standard Poisson equation. Although similar formulations make their appearance in various physical models, such as the flow potential equation and the electric potential equation with known spatial charge distribution, the current continuity equation distinguishes itself from others in several aspects. Firstly, the large imposed magnetic field required to yield observable electromagnetic interaction introduces non-negligible Hall and ion-slip effects. To account for these effects, a tensor electrical conductivity must be adopted. Secondly, one must treat sharp gradients in the flow field caused by shocks as well as others in the electrical potential near insulator/electrode junctures [2].

1.3 Review of Related Works

Among the earliest aerodynamic applications of the interaction of an electrically conducting fluid and electromagnetic field, Bush provided an approximate analytical solution for hypersonic

flow over a blunt body [27]. He considered an inviscid incompressible flow, with constant electrical conductivity, and predicted a significant “braking” effect in the presence of a strong magnetic field. Coakley and Porter presented the first CFD simulations of the MHD blunt body problem by means of a model analogous to Bush’s, and reported qualitatively similar results [28]. Because of limited computational resources at that time, these simulations adopted significant simplifications by assuming that the gas was ideal, inviscid and chemically non-reacting.

Ziemer conducted the first experimental work focusing on measuring shock standoff distance and reported reasonable agreement with Bush’s analytical work [29]. Another hypersonic experimental work was reported by Bulen *et al.*, who investigated shock standoff distance and heat transfer mitigation for viscous flow over axisymmetric geometries under significant Hall effect [30]. These experiments exhibited increased shock standoff distance, as well as increased total drag caused by the presence of a magnetic dipole. An unexpected increase in total heating, attributed to the Hall effect, was reported contradicting the semi-analytic models. Regardless of this unexpected outcome, concerns pertaining to the magnet weight hindered further research efforts and the enthusiasm for MGD technologies waned in the 70s. It was not until the 90s that interest in MGD-based hypersonic flow control techniques started to resurge.

While recent experimental studies have provided new insights into electromagnetic effects on hypersonic flows and additional validation resources for MGD codes [31-33], their scope is limited by their prohibitively high cost. Meanwhile, computational approaches have gained considerable ground in the design and optimization of hypersonic vehicles. Palmer was one of the first to reevaluate MGD technologies using modern CFD tools [34]. First-order simulations of a Mars return aerobrake vehicle entering the Earth’s atmosphere were carried out by solving the coupled Maxwell and Navier-Stokes equations.

The three formulations mentioned in the preceding section, namely, the FMFD model, the (resistive) MHD model and the low-magnetic Reynolds number approximation have by now been extensively investigated. Gaitonde and Poggie utilized the MHD model to simulate inviscid flow over two- and three-dimensional cylindrical bodies with non-uniform magnetic field distribution and observed an increase in shock standoff distance and a decrease in surface heat transfer rate. The electrical conductivity of the fluid was identified as the most important parameter in the fluid-magnetic field interaction [35]. In a subsequent study, Poggie and Gaitonde used the low-magnetic Reynolds number formulation to investigate inviscid and

viscous flows over a hemisphere [2]. An increase in shock standoff distance caused by the applied magnetic field was again observed in both cases, as well as a reduction in wall heat flux. It was concluded that viscosity has little impact on the effects of the applied magnetic field [26].

Pàscoa *et al.* [36] present a numerical approach for MGD thrusters and Faraday generators employing the low-magnetic Reynolds number formulation. The flow equations were solved using the PISO algorithm and the electromagnetic problem was approximated by a Poisson-like equation for the electric potential. At each iteration, the magnetic field was corrected by the gradient of the electric potential to ensure the divergence-free constraint. Results were reported for the Hartmann flow and for cylindrical flows subject to an axial magnetic field.

Chelem and Groll [37] developed a finite volume formulation of the MHD model using the coupling strategy of the modified AUSM-MHD [38]. The PISO algorithm for magnetic pressure correction was employed and mixed with a semi-discrete non-staggered central scheme for flux calculation [39]. The authors introduced a magnetic potential into the magnetic induction equation to ensure a divergence-free magnetic field, similar to Reference [40]. Results were presented for an MHD shock tube and the Villani-H thruster.

Takeda and Yamamoto [41] investigated the case of supersonic MPD viscous flows with partial ionization using the resistive MHD model. The model presented was based on the axisymmetric compressible Navier-Stokes equations with Lorentz force and Joule heating, the magnetic induction equation and the continuity equation of electrons. The effects of the inlet temperature, the total current and the rate of ionization were investigated, and results were partially compared with experiments.

Miki *et al.* [42] conducted a Large Eddy Simulation in an MHD energy bypass scramjet engine by solving the unsteady compressible Navier-Stokes equations and the magnetic induction equation. The numerical approach for the MHD equations was based on an approximate Harten-Lax-Van Leer (HLL) Riemann solver. Results were obtained for both non-reacting and reacting flows without ionization and were in good agreement with experimental data. The authors also presented results for plasma-assisted combustion and investigated the effects of electromagnetic fields, temperature, density and mass fractions.

Bityurin *et al.* investigated MHD flow and flight control, both experimentally and computationally, over several geometries such as circular cylinder, wedge, cowl-wedge, blunt body and re-entry airfoil [19, 32, 86, 87]. In Reference [32], the low-magnetic Reynolds number

approximation was utilized to simulate a two-dimensional cylinder with azimuthal magnetic field distribution. Two types of electrical conductivity models were investigated in Reference [19]: an equilibrium model that assumed ionization existed only behind the shock, and a frozen ionization model that assumed a fully-ionized medium in the entire domain. The equilibrium model was employed to represent conditions encountered by a re-entry vehicle, whereas the frozen ionization model corresponded to situations in the ground test wind tunnel facility used for their experimental work. It was observed that the applied magnetic field had stronger effects on flow structure when the equilibrium ionization was utilized. In addition, the Hall effect was significant for cases employing the frozen ionization model and reduced the overall MHD control efficiency, whereas cases with the equilibrium ionization model found the Hall effect negligible.

Bobashev and Golovachov [43] performed numerical studies of MHD flows in a supersonic intake based on a Godunov-type finite volume scheme and the low-magnetic Reynolds number approximation. The results assessed the possibility of the deceleration of plasma flows down to subsonic speeds by the application of a magnetic field. The authors found out that the performance of this Faraday-type device was more effective when the Hall effect was suppressed.

Simulations employing the FMFD model have also been reported. MacCormack [44, 45] used a modified Steger-Warming method, combined with artificially-scaled Maxwell flux vectors, and presented results for the Hartmann flow, an MGD accelerator, an MGD generator and a simplified two-dimensional MHD energy bypass scramjet engine. It was shown that the low-magnetic Reynolds number approximation failed to capture significant phenomena during the transient regime and that the utilization of the full MGD equations was necessary. Because of the computational cost caused by the distinct characteristics of the electromagnetic and flow fields, this approach has been applied to only simple two-dimensional or axisymmetric geometries.

1.4 Review of Numerical Approaches

The numerical simulation of hypersonic flow begins with the discretization of the governing equations. The temporal discretization may be either explicit or implicit. Explicit approaches were used in the 1980s due to their moderate computational requirements, but the stiffness resulting from the chemical reaction terms may restrict the permissible time step to an extremely small number, resulting in long simulation times. Nowadays, implicit methods are preferred

because they are more stable and, as a result, the allowable time step is much larger than for explicit methods.

The spatial discretization can use either a finite volume method (FVM) or a finite element method (FEM), with the former being most dominant. In addition, both structured and unstructured meshes can be used, again with the former being most dominant. As an example of the variety of choices, the Michigan Aerothermodynamic Navier-Stokes Solver (LeMANS) [46] is a hypersonic FVM code designed for unstructured meshes. The calculations of numerical fluxes are computed by a modified Steger-Warming flux splitting method and the linear system solved using a line relaxation method, with an algorithm to find the line direction in unstructured meshes. The low-magnetic Reynolds number approximation is adopted to simplify the Maxwell equations and a finite difference scheme utilized to compute electric and current fields.

The incompatibility in eigenvalues of electromagnetism and fluid dynamics is a major issue in MGD simulations using the FMFD model. In an effort to solve the FMFD equations in the FVM framework, MacCormack [45] proposed a novel scaling of the Maxwell flux vectors that balanced the numerical dissipation with the magnitude of the elements of the Maxwell flux vector itself. D'Ambrosio *et al.* proposed a method based on altering the magnitude of speed of light in the Maxwell equations to render the characteristic time scale of electromagnetism comparable with the one of gasdynamics [3].

Employing the low-magnetic Reynolds number approximation, Gaitonde [2] developed a high-order approximately factored compact-difference-based method to solve the three-dimensional current continuity equation. The general case of spatially varying, tensorial electrical conductivity due to the presence of Hall and ion-slip effects was addressed, and compatible high-order boundary conditions are proposed for electrodes and insulators.

Computational hypersonic codes have also been developed in the finite element context. Djaffar and Habashi [47] developed a fully-implicit FEM code for two-dimensional flows, adopting the two-temperature and finite-rate chemical models. To reduce the computation to a manageable level, this code utilizes a loosely-coupled approach that segregates the hypersonic system into gasdynamic, thermo-chemical non-equilibrium subsystems that are solved sequentially. In addition, an anisotropic mesh optimization technique was introduced for the first time to accurately capture shock waves.

The tensorial characteristic of electrical conductivity significantly affects the convergence of numerical schemes in solving the current continuity equation. Cristofolini *et al.* proposed a modified reverse Cuthill-McKee (RCM) procedure based on FEM that took into account the relation between the mesh geometry and magnetic direction [48]. Both original and modified RCM procedures have improved the convergence rate of the GMRES solver, and the modified RCM showed a higher convergence rate for strong anisotropies.

Despite many advantages of FEM, such as good representation of complex geometries, natural imposition of boundary conditions, reduced sensitivity to high-aspect-ratio cells and second-order discretization of viscous terms, significant difficulties remain in the design of shock-capturing second-order stabilization terms [49] for the inviscid fluxes. Alternately, the edge-based Galerkin formulation of Selmin [50] takes advantage of upwinding schemes primarily developed in the FVM context. In Selmin's formulation, the matrix assembly is carried out by looping over edges, instead of looping over elements, substantially reducing the indirect memory addressing required for unstructured meshes and yielding considerable computational savings for 3D problems.

As previously mentioned, the majority of numerical simulations in the supersonic and hypersonic regimes utilize structured meshes [51, 52]. Unstructured meshes, despite flexibility in discretizing complex geometries and ease of generation, are often associated with loss of accuracy in shocks and boundary layers. This is most visible in derived quantities such as the heat flux distribution in the vicinity of the stagnation point in hypersonic simulations. By their very nature, unstructured meshes are not aligned with any flow feature. At high Mach numbers, mesh irregularities across shocks induce enthalpy oscillations, which are then transported downstream and through the boundary layer, inducing oscillations in the surface heat flux distribution. In all fairness, however, it should be noted that similar difficulties can easily be encountered with structured grids when they are not aligned with shocks or entropy discontinuities, for example with oblique shocks or multiple shocks, which is generally the case for complex geometries.

Many attempts have been made to eliminate this problem by improving shock-grid alignment [53-55] or improving the numerical schemes (e.g. improved flux reconstruction [56], use of high-order algorithms [57], shock fitting [58] etc.). Habashi *et al.* [59] have effectively shown that the key to accurate use of unstructured grids is automatic anisotropic mesh

optimization, and demonstrated accurate hypersonic calculations on both structured [47] and unstructured [60] grids.

Mesh-flow misalignment problems are further compounded in multidisciplinary applications. For example, flow and electro-magnetic (EM) quantities have disparate time/length scales and are not aligned in space. Thus, mesh optimization of only the flow field may cause insufficient resolution of the EM field, especially when discontinuities typical of high-speed flows are present. In the present work, the edge-based mesh optimization methodology of [60] is generalized for multi-disciplinary applications to simultaneously optimize the mesh according to flow field variables such as pressure, density, temperature, turbulence and velocity, as well as the electric potential. Results demonstrate that such anisotropic mesh optimization produces absolutely necessary complex node/element distributions, impossible to anticipate at the mesh generation stage, leading to high resolution despite the disparity of length scales.

1.5 Thesis Objectives

The CFD Lab at McGill University is developing an all-Mach number hypersonic code for civil aviation, HALO3D (High Altitude Low Orbit 3D), in collaboration with ANSYS and funded by Lockheed Martin under an NSRC Industrial Chair. This thesis is the very essential electro-magnetic module of HALO3D for conductive flows. It aims to provide an approach, compatible to the CFD part, that preserves good computational efficiency, robustness, and accuracy. This work focuses on the resistive MHD and low-magnetic Reynolds number models. The effects of thermal/chemical non-equilibrium, ablation, catalysis and radiation are tackled by parallel efforts at the CFD Lab.

1.6 Thesis Contributions

The engineering contribution is to provide an easy-to-use software toolkit that can simulate electromagnetic effects, their interaction with flows, and their unique applications in hypersonics. A graphical user interface is provided that can set up flow and EM configurations efficiently. In the toolkit, there are dedicated tools to monitor the convergence history, to visualize the solution, and to edit the grids. Installment guides and tutorials are also provided. Most of the above-mentioned functionalities were developed by former students at the CFD Lab and experts from ANSYS. Thanks to their contributions, it is possible to update the numerical technologies and develop new physical models in the HALO3D framework without reinventing the wheel.

The author's specific contributions are summarized as follows:

1. Development of an edge-based FEM solver for the low-Magnetic Reynolds number approximation;
2. Introduction of Hall effects and development of a hybrid edge/element-based assembly strategy to address challenges of asymmetric tensorial electrical conductivity;
3. Development of an edge-based FEM solver for the resistive MHD model;
4. Development of anisotropic mesh optimization strategies for heterogeneous physical quantities of flow and EM fields.

1.7 Thesis Outline

This thesis is organized as follows: in Chapter 2 the mathematical modeling is given for both the resistive MHD model and the low-magnetic Reynolds number approximation. Chapter 3 describes the edge-based FEM numerical formulations. Chapters 4 and 5 presents the numerical results of hypersonic flows obtained with the low-magnetic Reynolds number approximation and the resistive MHD model, respectively. Chapter 6 provides concluding remarks and future developments.

2 Mathematical Formulation

2.1 Resistive MHD Model

Hypersonic flows under an imposed magnetic field are often modeled by the compressible RANS equations and the magnetic induction equation (resistive MHD model). The former express the conservation of mass, momentum and energy of the fluid, while the latter is derived from the Maxwell equations under the MGD assumptions [61]. The RANS equations can be written as

$$\begin{aligned} \frac{\partial \rho}{\partial t} + \nabla \cdot (\rho \mathbf{V}) &= 0 \\ \frac{\partial \rho \mathbf{V}}{\partial t} + \nabla \cdot (\rho \mathbf{V} \mathbf{V} + p \mathbf{I}) - \nabla \cdot \boldsymbol{\tau} &= \mathbf{j} \times \mathbf{B} \\ \frac{\partial \rho e_t}{\partial t} + \nabla \cdot ((\rho e_t + p) \mathbf{V}) - \nabla \cdot (\mathbf{V} \cdot \boldsymbol{\tau}) + \nabla \cdot \mathbf{q} &= \mathbf{j} \cdot \mathbf{E} \end{aligned} \quad (2.1)$$

where $\mathbf{V} \mathbf{V}$ is a tensor computed as the outer product, and $\mathbf{V} \cdot \boldsymbol{\tau}$ is a vector resulting from the product between a vector and a tensor. Using Einstein's notation, one gets

$$(\mathbf{V} \mathbf{V})_{ik} = V_i V_k \quad (\mathbf{V} \cdot \boldsymbol{\tau})_i = V_k \tau_{ik}$$

The total magnetic field, \mathbf{B} , is equal to sum of the imposed magnetic field \mathbf{B}_0 and the induced magnetic field \mathbf{b} . The electromagnetic body force and Joule heating terms appearing on the RHS of the momentum and energy equations require the prior knowledge of the electromagnetic quantities \mathbf{j} , \mathbf{B} and \mathbf{E} . These can be computed by the following set of equations, assuming that the electrical conductivity σ is a scalar

$$\mathbf{j} = \sigma (\mathbf{E} + \mathbf{V} \times \mathbf{B}) \quad (2.2)$$

$$\frac{\partial \mathbf{B}}{\partial t} - \nabla \times (\mathbf{V} \times \mathbf{B}) + \nu \nabla \times (\nabla \times \mathbf{B}) = \mathbf{0} \quad (2.3)$$

$$\nabla \cdot \mathbf{B} = 0 \quad (2.4)$$

Eq. (2.2) is Ohm's law and relates the electric current density to the electric, magnetic, and velocity fields; Eq. (2.3) is the magnetic induction equation directly derived from the Maxwell equations under the MHD assumptions, while Eq. (2.4) expresses the conservation of the magnetic field. The Helmholtz form of Eq. (2.3) [62, 63] can be derived from Eq. (2.3) while implicitly respecting the magnetic field free-divergence constraint expressed by Eq. (2.4), i.e.

$$\frac{\partial \mathbf{B}}{\partial t} - \nabla \times (\mathbf{V} \times \mathbf{B}) - \nu \nabla^2 \mathbf{B} = \mathbf{0} \quad (2.5)$$

By introducing the following non-dimensional variables

$$\mathbf{x}^* = \frac{\mathbf{x}}{l}, \quad \mathbf{B}^* = \frac{\mathbf{B}}{B_0}, \quad t^* = \frac{tV_0}{l}, \quad \mathbf{V}^* = \frac{\mathbf{V}}{V_0} \quad (2.6)$$

the magnetic induction equation (2.5) is expressed as

$$\frac{\partial \mathbf{B}^*}{\partial t^*} - \nabla^* \times (\mathbf{V}^* \times \mathbf{B}^*) - \frac{1}{\text{Re}_m} \nabla^2 \mathbf{B}^* = \mathbf{0} \quad (2.7)$$

where the magnetic Reynolds number denotes the ratio of the magnetic field convection to its diffusion and is defined as

$$\text{Re}_m = \frac{V_0 l}{\nu} \quad (2.8)$$

For cases where the magnetic Reynolds number is of the order of unity and above, the full set of Eqs. (2.9-10) should be considered for adequate modeling of the coupled phenomena

$$\begin{aligned} \frac{\partial \rho}{\partial t} + \nabla \cdot (\rho \mathbf{V}) &= \mathbf{0} \\ \frac{\partial \rho \mathbf{V}}{\partial t} + \nabla \cdot (\rho \mathbf{V} \mathbf{V} + p \mathbf{I}) - \nabla \cdot \boldsymbol{\tau} &= \mathbf{j} \times \mathbf{B} \\ \frac{\partial \rho e_t}{\partial t} + \nabla \cdot ((\rho e_t + p) \mathbf{V}) - \nabla \cdot (\mathbf{V} \cdot \boldsymbol{\tau}) + \nabla \cdot \mathbf{q} &= \mathbf{j} \cdot \mathbf{E} \\ \frac{\partial \mathbf{B}}{\partial t} - \nabla \times (\mathbf{V} \times \mathbf{B}) - \nu \nabla^2 \mathbf{B} &= \mathbf{0} \end{aligned} \quad (2.9)$$

$$(2.10)$$

For steady-state, this system can be written in compact form as

$$\nabla \cdot (\mathbf{F}^A(Q) - \mathbf{F}^V(Q, \nabla Q)) = \mathbf{S}^L \quad (2.11)$$

where Q is

$$Q = (\rho, \rho \mathbf{V}, \rho e_t)^T \quad (2.12)$$

and \mathbf{S}^L is

$$\mathbf{S}^L = (0, \sigma (\mathbf{E} + \mathbf{V} \times \mathbf{B}) \times \mathbf{B}, \sigma (\mathbf{E} + \mathbf{V} \times \mathbf{B}) \cdot \mathbf{E})^T \quad (2.13)$$

The inviscid flux vector, the viscous flux vector and the electromagnetic source terms in Cartesian coordinates are expressed as

$$\mathbf{F}_x^A = \begin{Bmatrix} \rho u \\ \rho u^2 + p \\ \rho uv \\ \rho uw \\ u(\rho e_t + p) \end{Bmatrix}, \quad \mathbf{F}_y^A = \begin{Bmatrix} \rho v \\ \rho uv \\ \rho v^2 + p \\ \rho vw \\ v(\rho e_t + p) \end{Bmatrix}, \quad \mathbf{F}_z^A = \begin{Bmatrix} \rho w \\ \rho uw \\ \rho vw \\ \rho w^2 + p \\ w(\rho e_t + p) \end{Bmatrix} \quad (2.14)$$

$$\mathbf{F}_x^V = \begin{Bmatrix} 0 \\ \tau_{xx} \\ \tau_{xy} \\ \tau_{xz} \\ \mathbf{V}\tau_x + q_x \end{Bmatrix}, \quad \mathbf{F}_y^V = \begin{Bmatrix} 0 \\ \tau_{yx} \\ \tau_{yy} \\ \tau_{yz} \\ \mathbf{V}\tau_y + q_y \end{Bmatrix}, \quad \mathbf{F}_z^V = \begin{Bmatrix} 0 \\ \tau_{zx} \\ \tau_{zy} \\ \tau_{zz} \\ \mathbf{V}\tau_z + q_z \end{Bmatrix} \quad (2.15)$$

$$\mathbf{S}^L = \sigma \begin{Bmatrix} 0 \\ E_y B_z - E_z B_y + w B_x B_z + v B_x B_y - u(B_y^2 + B_z^2) \\ E_z B_x - E_x B_z + u B_y B_x + w B_y B_z - v(B_x^2 + B_z^2) \\ E_x B_y - E_y B_x + u B_z B_x + v B_z B_y - w(B_x^2 + B_y^2) \\ (E_x + v B_z - w B_y)E_x + (E_y + w B_x - u B_z)E_y + (E_z + u B_y - v B_x)E_z \end{Bmatrix} \quad (2.16)$$

In the steady state regime, Eq. (2.10) can be expressed in Cartesian coordinates as

$$\begin{cases} \frac{\partial}{\partial z}(w B_x - u B_z) - \frac{\partial}{\partial y}(u B_y - v B_x) - \nu \left(\frac{\partial^2 B_x}{\partial x^2} + \frac{\partial^2 B_x}{\partial y^2} + \frac{\partial^2 B_x}{\partial z^2} \right) = 0 \\ \frac{\partial}{\partial x}(u B_y - v B_x) - \frac{\partial}{\partial z}(v B_z - w B_y) - \nu \left(\frac{\partial^2 B_y}{\partial x^2} + \frac{\partial^2 B_y}{\partial y^2} + \frac{\partial^2 B_y}{\partial z^2} \right) = 0 \\ \frac{\partial}{\partial y}(v B_z - w B_y) - \frac{\partial}{\partial x}(w B_x - u B_z) - \nu \left(\frac{\partial^2 B_z}{\partial x^2} + \frac{\partial^2 B_z}{\partial y^2} + \frac{\partial^2 B_z}{\partial z^2} \right) = 0 \end{cases} \quad (2.17)$$

2.2 Low-Magnetic Reynolds Number Approximation

When the magnetic Reynolds number, Re_m , is less than unity, the magnetic convection can be neglected compared to its diffusion and Eq. (2.3) becomes Laplacian-like, expressing the diffusion of a magnetic field that vanishes as it approaches the external boundaries. In this case, the induced magnetic field, \mathbf{b} , can be neglected compared to the imposed one, \mathbf{B}_0 , and Eq. (2.10) can be replaced by the current-continuity equation [64], obtained by taking the divergence of the Ampere-Maxwell law:

$$\nabla \cdot (\nabla \times \mathbf{B}) = \mu_0 \nabla \cdot \mathbf{j} = 0 \quad (2.18)$$

The electric potential ϕ is introduced through $\mathbf{E} = -\nabla\phi$, yielding

$$\nabla \cdot [\boldsymbol{\sigma} \cdot (-\nabla\phi + \mathbf{V} \times \mathbf{B}_0)] = 0 \quad (2.19)$$

which is a scalar equation. Note that $\boldsymbol{\sigma}$ is the electrical conductivity tensor, a compact way of accounting for ion-slip and the Hall effect. Adopting the formulation of Gaitonde and Poggie [4], Eq. (2.20) gives the electrical conductivity tensor with the Hall effect

$$\boldsymbol{\sigma} = \frac{\sigma}{D} \begin{bmatrix} B^2 + \beta^2 B_x^2 & \beta(\beta B_y B_x - B B_z) & \beta(\beta B_z B_x + B B_y) \\ \beta(\beta B_y B_x + B B_z) & B^2 + \beta^2 B_y^2 & \beta(\beta B_z B_y + B B_x) \\ \beta(\beta B_z B_x - B B_y) & \beta(\beta B_z B_y + B B_x) & B^2 + \beta^2 B_z^2 \end{bmatrix} \quad (2.20)$$

where $D = B^2(1 + \beta^2)$. The Hall parameter β is defined as:

$$\beta = \frac{\varepsilon B}{m_e v_m} \quad (2.21)$$

where ε is the elemental charge $\varepsilon = 1.6022 \times 10^{-19} C$, $m_e = 9.11 \times 10^{-31} kg$ is the mass of a single electron, and v_m is the electron-neutral particle momentum transfer collision frequency related to the electrical conductivity:

$$v_m = \frac{\varepsilon^2 n_e}{m_e \sigma} \quad (2.22)$$

where n_e is the electron number density. Using Eq. (2.22) to substitute v_m in Eq. (2.21), the Hall parameter β can be directly related to the fluid properties:

$$\beta = \frac{\sigma B}{\varepsilon n_e} \quad (2.23)$$

3 Numerical Modeling

The weak-Galerkin formulation of Eq. (2.1) is obtained by multiplication with a linear test function W_i , followed by integration by parts [65]

$$\int_{\Omega} W_i \frac{\partial \mathbf{Q}}{\partial t} - \int_{\Omega} \nabla W_i \cdot (\mathbf{F}^A - \mathbf{F}^V) + \int_{\partial\Omega} W_i \mathbf{n} \cdot (\mathbf{F}^A - \mathbf{F}^V) = \int_{\Omega} W_i \mathbf{S}^L \quad (3.1)$$

The symbol “ \cdot ” denotes the inner product between vectors (Appendix A). A linear shape function is selected since a smooth higher-order shape function cannot capture discontinuities, such as shocks and contact discontinuities. The conservative variables \mathbf{Q} and the source term \mathbf{S}^L are interpolated by means of a linear shape function N_i at node i . The inviscid fluxes \mathbf{F}^A are discretized by group representation:

$$\mathbf{Q}(x, t) = \sum_{j=1}^{N_G} N_j(x) \mathbf{Q}_j(t), \quad \mathbf{F}^A(x, t) = \sum_{j=1}^{N_G} N_j(x) \mathbf{F}_j^A(t), \quad \mathbf{S}^L(x, t) = \sum_{j=1}^{N_G} N_j(x) \mathbf{S}_j^L(t) \quad (3.2)$$

where N_G is the total number of nodes, Q_j , \mathbf{F}_j^A and \mathbf{S}_j^L are the nodal values only dependent on time. Substituting Eq. (3.2) into Eq. (3.1) yields

$$\begin{aligned} & \sum_{e \in E_i} \sum_{j \in K_e} \int_{V^e} W_i N_j \frac{dQ_j}{dt} dV - \sum_{e \in E_i} \sum_{j \in K_e} \int_{V^e} N_j \nabla W_i \cdot \mathbf{F}_j^A dV + \sum_{e \in E_i} \int_V \nabla W_i \cdot \mathbf{F}^V dV \\ & + \sum_{e \in F_i} \int_A W_i \mathbf{n} \cdot (\mathbf{F}^A - \mathbf{F}^V) dA = \sum_{e \in E_i} \sum_{j \in K_e} \int_{V^e} W_i N_j \mathbf{S}_j^L dV \end{aligned} \quad (3.3)$$

where E_i is the set of elements sharing the i -th vertex, F_i is the set of boundary faces sharing the i -th vertex, K_e is the set of nodes of the e -th element, V is the whole volume domain, and V^e is the volume of e -th element.

3.1 Lumped-Mass Matrix

Introducing the lumped-mass matrix and the consistent-mass matrix,

$$L_i = \sum_{e \in E_i} \int_{V^e} W_i dV \quad H_{ij} = \sum_{e \in E_i} \int_{V^e} W_i W_j dV \quad (3.4)$$

the temporal term in Eq. (3.3) can then be written as

$$\sum_{e \in E_i} \sum_{j \in K_e} \int_{V^e} W_i N_j \frac{dQ_j}{dt} dV = L_i \frac{dQ_i}{dt} + \sum_{j \in K_i} H_{ij} \frac{Q_j - Q_i}{2} \quad (3.5)$$

The source term in Eq. (3.3) reads

$$\sum_{e \in E_i} \sum_{j \in K_e} \int_{V^e} W_i N_j \mathbf{S}_j^L dV = L_i \mathbf{S}_j^L + \sum_{j \in K_i} H_{ij} \frac{\mathbf{S}_j^L - \mathbf{S}_i^L}{2} \quad (3.6)$$

3.2 Inviscid Fluxes

The edge-based Galerkin formulation, first introduced by Selmin [50], consists of a summation over pairs of nodes during assembly, such that solution-dependent quantities are factored out from quantities dependent on the spatial discretization. Consequently, the edge coefficients associated with the geometrical characteristics of the mesh can be computed in a pre-processing phase and not at each solution iteration [66]. The edge-based assembly also handles hybrid meshes with a unique data structure that is computationally more efficient than its element-based counterpart [67]. Edge-based assembly also permits Total Variation Diminishing (TVD) schemes to stabilize the advection terms. Moreover, a one-to-one analogous relation has been reported between the edge-based FEM and FVM for both simplicial [68] and non-simplicial [69] meshes.

The domain assembly of the inviscid fluxes \mathbf{F}^A in Eq. (3.3) can be reformulated in an edge-based fashion [50]

$$-\sum_{e \in E_i} \sum_{j \in K_e} \int_{V^e} N_j \nabla W_i \cdot \mathbf{F}_j^A dV = \sum_{j \in K_i} \boldsymbol{\eta}_{ij} \cdot \frac{\mathbf{F}_i^A + \mathbf{F}_j^A}{2} - \sum_{j \in K_i} \boldsymbol{\chi}_{ij} \cdot \frac{\mathbf{F}_j^A - \mathbf{F}_i^A}{2} \quad (3.7)$$

where K_i is the set of nodes connected to i -th vertex via an element, $\boldsymbol{\eta}_{ij}$ and $\boldsymbol{\chi}_{ij}$ are edge coefficients, defined as

$$\boldsymbol{\eta}_{ij} = \sum_{e \in E_i} \int_{V^e} (W_i \nabla N_j - N_j \nabla W_i) dV \quad \boldsymbol{\chi}_{ij} = \sum_{e \in E_i} \int_A W_i N_j \mathbf{n} dA \quad (3.8)$$

Note that the coefficient $\boldsymbol{\chi}_{ij}$ is only defined for boundary edges. In Eq. (3.7), the first term on the RHS is an arithmetic average of inviscid fluxes between node i and node j . To provide stabilization for advection-dominated flows, the vector of inviscid fluxes \mathbf{F}^A is replaced with a numerical counterpart, $\boldsymbol{\Phi}^{\text{num}}$ evaluated at the edge's midpoint, i.e.

$$\boldsymbol{\eta}_{ij} \cdot \frac{\mathbf{F}_i^A + \mathbf{F}_j^A}{2} = \boldsymbol{\Phi}^{\text{num}}(Q_i, Q_j, \boldsymbol{\eta}_{ij}) \quad (3.9)$$

The numerical inviscid fluxes used in this Thesis are the Roe fluxes [70], being nonlinear functions of the nodal variables and of the edge coefficients.

3.2.1 Viscous Fluxes

The domain assembly of the viscous fluxes \mathbf{F}^V in Eq. (3.3) is composed of the stress tensor, the inner product of stress tensor and velocity, and the heat flux. The stress tensor is assembled in an edge-based fashion as [68]

$$\sum_{e \in E_i} \int_V \nabla W_i \cdot \boldsymbol{\tau} dV = \sum_{j \in K_i} [(\mu_{ij} \text{tr}(\mathbf{d}_{ij}) \mathbf{I} + (\mu_{ij} + \lambda_{ij}) \mathbf{d}_{ij}^S + (\lambda_{ij} - \mu_{ij}) \mathbf{d}_{ij}^A)(\mathbf{v}_j - \mathbf{v}_i)] \quad (3.10)$$

The inner product between a vector and a second-order tensor is defined in Appendix A. The edge mid-point quantities, μ_{ij} and λ_{ij} , are calculated by the arithmetic average of the node values. The edge coefficient \mathbf{d}_{ij} is a second order tensor defined as

$$\mathbf{d}_{ij} = \sum_{e \in E_i} \int_{V^e} (\nabla W_i \nabla N_j) dV \quad (3.11)$$

$\text{tr}(\cdot)$ is the trace operator and \mathbf{d}_{ij}^S and \mathbf{d}_{ij}^A are the symmetric and anti-symmetric part of \mathbf{d}_{ij} , i.e.

$$\mathbf{d}_{ij}^S = \frac{\mathbf{d}_{ij} + (\mathbf{d}_{ij})^T}{2} \quad \mathbf{d}_{ij}^A = \frac{\mathbf{d}_{ij} - (\mathbf{d}_{ij})^T}{2} \quad (3.12)$$

Similarly, the inner product of stress tensor and velocity are assembled as

$$\begin{aligned} \sum_{e \in E_i} \int_V \nabla W_i \cdot (\boldsymbol{\tau} \cdot \mathbf{v}) dV \\ = \sum_{j \in K_i} [(\mu_{ij} \text{tr}(\mathbf{d}_{ij}) \mathbf{I} + (\mu_{ij} + \lambda_{ij}) \mathbf{d}_{ij}^S + (\lambda_{ij} - \mu_{ij}) \mathbf{d}_{ij}^A) : \mathbf{v}_{ij} (\mathbf{v}_j - \mathbf{v}_i)] \end{aligned} \quad (3.13)$$

The column product between two second-order tensors is defined in Appendix A. The heat fluxes of the translational-rotational energy mode are assembled as

$$\sum_{e \in E_i} \int_{V^e} \nabla W_i \cdot \mathbf{q} dV = - \sum_{j \in K_i} [k_{ij} \text{tr}(\mathbf{d}_{ij})(T_j - T_i)] \quad (3.14)$$

3.3 Magnetic Induction Equation (Resistive MHD Model)

For steady-state computations, the weak formulation of Eq. (2.10) is written as

$$\sum_{e \in E_i} \int_{V^e} W_i (\nabla \times \mathbf{F}^B + \nu \nabla^2 \mathbf{B}) dV = \mathbf{0} \quad (3.15)$$

where $\mathbf{F}^B = \mathbf{V} \times \mathbf{B}$ is introduced for simplicity. Noting that

$$W_i (\nabla \times \mathbf{F}^B) = \nabla \times (W_i \mathbf{F}^B) - (\nabla W_i \times \mathbf{F}^B) \quad (3.16)$$

and utilising the divergence theorem, Eq. (3.15) can be rewritten as

$$-\sum_{e \in E_i} \int_{V_e} ((\nabla W_i \times \mathbf{F}^B) - W_i \nu \nabla^2 \mathbf{B}) dV + \sum_{e \in F_i} \int_{A_e} W_i \mathbf{n} \times \mathbf{F}^B dA = \mathbf{0} \quad (3.17)$$

Analogous to the treatment of the inviscid flux \mathbf{F}^A in Eq. (3.7), the convection term (the first term) in Eq. (3.17) is cast in an edge-based fashion as

$$-\sum_{e \in E_i} \int_{V_e} \nabla W_i \times \mathbf{F}^B dV = \sum_{j \in K_i} \boldsymbol{\eta}_{ij} \times \frac{\mathbf{F}_j^B + \mathbf{F}_i^B}{2} - \boldsymbol{\chi}_{ij} \times \frac{\mathbf{F}_j^B - \mathbf{F}_i^B}{2} \quad (3.18)$$

Assuming the magnetic diffusivity coefficient ν to be constant, the diffusion term in Eq. (3.17) is first integrated by part, yielding

$$\sum_{e \in E_i} \int_{V_e} W_i \nu \nabla^2 \mathbf{B} dV = -\nu \sum_{e \in E_i} \int_{V_e} \nabla W_i \cdot \nabla \mathbf{B} dV + \nu \sum_{e \in F_i} \int_{A_e} W_i \mathbf{n} \cdot \nabla \mathbf{B} dA \quad (3.19)$$

Note also that the dot product of the gradient tensor and the normal vector corresponds to the normal derivative of the magnetic field, namely $\mathbf{n} \cdot \nabla \mathbf{B} = \partial \mathbf{B} / \partial n$. The edge-based assembly of Eq. (3.19) thus is

$$\sum_{e \in E_i} \int_{V_e} W_i \nu \nabla^2 \mathbf{B} dV_e = -\nu \sum_{j \in K_i} [\text{tr}(\mathbf{d}_{ij})(\mathbf{B}_j - \mathbf{B}_i) + \boldsymbol{\chi}_{ij} \cdot (\nabla \mathbf{B}_j - \nabla \mathbf{B}_i)] + \nu \boldsymbol{\xi}_i \cdot \nabla \mathbf{B}_i \quad (3.20)$$

where the edge coefficient $\boldsymbol{\xi}_i$, is computed as

$$\boldsymbol{\xi}_i = \sum_{e \in F_i} \int_{A_e} W_i \mathbf{n} dA \quad (3.21)$$

The discretization of the third term in Eq. (3.17) reads

$$\sum_{e \in F_i} \int_{A_f} W_i \mathbf{n} \times \mathbf{F}^B dA = \sum_{j \in K_i} \boldsymbol{\chi}_{ij} \times (\mathbf{F}_j^B - \mathbf{F}_i^B) + \boldsymbol{\xi}_i \times \mathbf{F}_i^B \quad (3.22)$$

Finally, recapitulating the above equations, the edge-based finite element formulation of the magnetic problem can be summarized as

$$\sum_{j \in K_i} \boldsymbol{\eta}_{ij} \times \frac{\mathbf{F}_j^B + \mathbf{F}_i^B}{2} - \boldsymbol{\chi}_{ij} \times \frac{\mathbf{F}_j^B - \mathbf{F}_i^B}{2} - \nu d_{ij} (\mathbf{B}_j - \mathbf{B}_i) + \boldsymbol{\xi}_i \cdot \nabla \mathbf{B}_i = \mathbf{0} \quad (3.23)$$

3.4 Current Continuity Equation (Low-Magnetic Reynolds Number Formulation)

The weak-Galerkin formulation of the current-continuity equation is written as

$$\sum_{e \in E_i} \int_{V_e} \nabla W_i \cdot (\boldsymbol{\sigma} \cdot \nabla \phi) dV_e + \sum_{e \in F_i} \int_{A_e} W_i \mathbf{n} \cdot \mathbf{j} dA_e - \sum_{e \in E_i} \int_{V_e} \nabla W_i \cdot (\boldsymbol{\sigma} \cdot \mathbf{F}^B) dV_e = 0 \quad (3.24)$$

Cast in an edge-based fashion, Eq. (3.24) becomes

$$\sum_{j \in K_i} \boldsymbol{\sigma}_{ij} : \boldsymbol{\eta}_{ij} \frac{\mathbf{F}_j^B + \mathbf{F}_i^B}{2} - \boldsymbol{\sigma}_{ij} : \boldsymbol{\chi}_{ij} \frac{\mathbf{F}_j^B - \mathbf{F}_i^B}{2} + \boldsymbol{\sigma}_{ij} : \mathbf{d}_{ij} (\phi_j - \phi_i) = 0 \quad (3.25)$$

Noting that

$$\boldsymbol{\sigma}_{ij} : \mathbf{d}_{ij} = \boldsymbol{\sigma}_{ij}^S : \mathbf{d}_{ij} + \boldsymbol{\sigma}_{ij}^A : \mathbf{d}_{ij} = \boldsymbol{\sigma}_{ij}^S : \mathbf{d}_{ij} \quad (3.26)$$

where $\boldsymbol{\sigma}_{ij}^S = \frac{\boldsymbol{\sigma} + \boldsymbol{\sigma}^T}{2}$ and $\boldsymbol{\sigma}_{ij}^A = \frac{\boldsymbol{\sigma} - \boldsymbol{\sigma}^T}{2}$ are the symmetric and skew-symmetric decompositions of $\boldsymbol{\sigma}$.

Eq. (3.25) is not applicable when the Hall effect is taken into account since the information stored in the skew-symmetric matrix of $\boldsymbol{\sigma}$ is lost during the assembly of the second-order derivative term, $\boldsymbol{\sigma}_{ij} : \mathbf{d}_{ij} (\phi_j - \phi_i)$. To address this drawback of edge-based assembly, we rewrite the first term in Eq. (3.24) as

$$\sum_{e \in E_i} \int_{V_e} \nabla W_i \cdot (\boldsymbol{\sigma} \cdot \nabla \phi) dV_e = \sum_{e \in E_i} \int_{V_e} \nabla W_i \cdot (\boldsymbol{\sigma}^S \cdot \nabla \phi) dV_e + \sum_{e \in E_i} \int_{V_e} \nabla W_i \cdot \mathbf{F}^{EA} dV_e \quad (3.27)$$

where \mathbf{F}^{EA} is defined as $\boldsymbol{\sigma}^A \cdot \nabla \phi$ and is treated as a flux vector. Eq. (3.25) therefore becomes

$$\sum_{j \in K_i} \boldsymbol{\sigma}_{ij} : \boldsymbol{\eta}_{ij} \frac{\mathbf{F}_j^B + \mathbf{F}_i^B}{2} - \boldsymbol{\sigma}_{ij} : \boldsymbol{\chi}_{ij} \frac{\mathbf{F}_j^B - \mathbf{F}_i^B}{2} + \boldsymbol{\sigma}_{ij}^S : \mathbf{D}_{ij} (\phi_j - \phi_i) + CT = 0 \quad (3.28)$$

where the edge-based correction term CT is defined as

$$CT = -\boldsymbol{\eta}_{ij} \frac{\mathbf{F}_j^{EA} + \mathbf{F}_i^{EA}}{2} + \boldsymbol{\chi}_{ij} \frac{\mathbf{F}_j^{EA} - \mathbf{F}_i^{EA}}{2} \quad (3.29)$$

When solving Eq. (3.28), \mathbf{F}^{EA} is evaluated using the solution of the previous time step since it involves the derivative of the electric potential. The solution algorithm therefore is only partially implicit and the convergence rate of the simulation is hampered. Moreover, the edge-based evaluation of derivatives is at best first-order accurate due to the approximation of a continuous variable by the edge's midpoint value. An alternative to the use of the edge-based correction term is obtained by reverting to the element-based assembly of the first term in Eq. (3.24)

$$\sum_{e \in E_i} \int_{V_e} \nabla W_i \cdot (\boldsymbol{\sigma} \cdot \nabla \phi) dV_e = \sum_{e \in E_i} \sum_{g \in G_e} \omega_g \nabla W_{ig} \cdot \left(\sum_{k \in K_e} N_{kg} \boldsymbol{\sigma}_k \cdot \sum_{k \in K_e} \nabla N_{kg} \phi_k \right) \quad (3.30)$$

Eq. (3.25) then becomes

$$\sum_{j \in Ki} \sigma_{ij} : \eta_{ij} \frac{\mathbf{F}_j^B + \mathbf{F}_i^B}{2} - \sigma_{ij} : \chi_{ij} \frac{\mathbf{F}_j^B - \mathbf{F}_i^B}{2} + \sum_{e \in Ei} \int_{V_e} \nabla W_i \cdot (\boldsymbol{\sigma} \cdot \nabla \phi) dV_e = 0 \quad (3.31)$$

yielding a mixed element-based and edge-based assembly.

3.5 Solution Strategy

Although Eqs. (3.23) and (3.28) are expressed for the steady-state case, the solution strategy makes use of a pseudo-transient continuation method where the original steady problem is transformed into a pseudo-unsteady one

$$\mathbf{A} \Delta \mathbf{Q}^{n+1} = -\mathbf{R}(\mathbf{Q}^n) \quad n = 0, 1, 2, \dots \quad (3.32)$$

with \mathbf{R} being the residual of Eq. (3.3), Eq. (3.23) or Eq. (3.28) and the Jacobian matrix \mathbf{A} is

$$\mathbf{A} = \left[\frac{1}{\Delta \tau} \mathbf{I} + \frac{\partial \tilde{\mathbf{R}}}{\partial \mathbf{Q}} \right]^n \quad (3.33)$$

The pseudo-time step $\Delta \tau^n$ is chosen to locally satisfy the CFL stability condition [71]. Small values of $\Delta \tau^n$ increase the diagonal dominance of the matrix, making its inversion easier and as $\Delta \tau^n$ increases, the first term on the RHS of Eq. (34) vanishes and the pseudo-unsteady system (33) reverts to a Newton method. Eq. (33) is solved by the GMRES method. To accelerate convergence, an ILU factorization of matrix \mathbf{A} is used as a right preconditioner [72]. The same $\Delta \tau^n$ is used for the flow and EM equations. Since a simultaneous solution approach would require substantial computing resources, a segregated approach is selected. The algorithm consists of computing a sequence of solutions of the two problems, as illustrated in Figure 1.

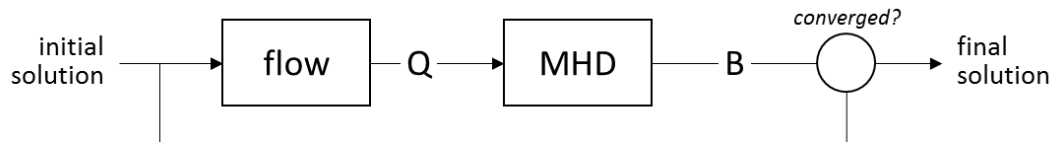


Figure 1. Sequence of solutions of the segregated approach.

3.6 Parallelization

Parallelization is realized by the standard message passing interface (MPI) [73]. ParMETIS [74] is used to partition the domain and minimize communication between processors. The domain is divided into partitions with one processor designated for each. The overlapping regions between partitions are updated with the solution is. A sparse parallel block AIJ format

matrix is assembled in the PETSc framework [75, 76]. Block Jacobi preconditioning [77] partitions the linear system into different blocks. By default, the number of blocks is the same as the number of processors. Since the blocks are used as preconditioners, it is not necessary to solve them exactly. Each block is solved approximately by applying its ILU [78] preconditioner of fill-in level zero with only one iteration. This procedure can be illustrated for Eq. (3.34), where n is the number of blocks, A_1, A_2, \dots, A_n are the block matrices from the linear system, b_1, b_2, \dots, b_n are the corresponding block vectors in the intermediate steps of GMRES, and P_1, P_2, \dots, P_n are the ILU preconditioners of A_1, A_2, \dots, A_n , respectively. Note that in the last step, the diagonal block A_i is approximately inverted by replacing it with the ILU preconditioner P_i .

4 Low-Magnetic Reynolds Number Formulation

In this chapter, results are presented under the low-magnetic Reynolds number formulation and the resistive MHD model will be covered in the next chapter. The flow and electro-magnetic libraries are loosely-coupled. In all of the solvers, the Jacobian is assembled and stored explicitly. Six test cases are presented. In Section 4.1, the current-continuity equation solver is first validated through a study of 2D segmented electrodes proposed by Zheng *et al.* [79]. The Hall effect is incorporated by utilizing a tensorial electrical conductivity. Sections 4.2 and 4.3 present, respectively, a Mach 5 inviscid flow and a Mach 4.75 laminar flow over a sphere. The first two test cases use structured grids, while the third test case is with an isotropic unstructured grid. These cases are used to examine the accuracy and performance of the proposed formulation.

Sections 4.5-4.7 present, respectively, a Mach 13.26 turbulent flow past an Apollo capsule with an angle of attack of 18.6° , a Mach 21.38 laminar flow over a sphere, and a Mach 17.61 turbulent flow over the Orbital Re-entry Experiment (OREX) capsule. Unstructured grids are used for these test cases, and an edge-based mesh optimization methodology as in [60] is used to adapt on an aggregate number of flow quantities (pressure, density, temperature, velocity and turbulent viscosity), as well as an EM quantity of interest (the electric potential in this chapter). The capabilities, and absolute necessity, of multi-disciplinary anisotropic mesh optimization are demonstrated in the last three cases using different solution optimization criteria.

4.1 Code Validation for Solving the Current-Continuity Equation

The validation of the current-continuity equation solver is performed by simulating ionized flow through singly-paired electrodes as shown in Figure 2. The tensor electrical conductivity σ is defined in Eq. (2.20).

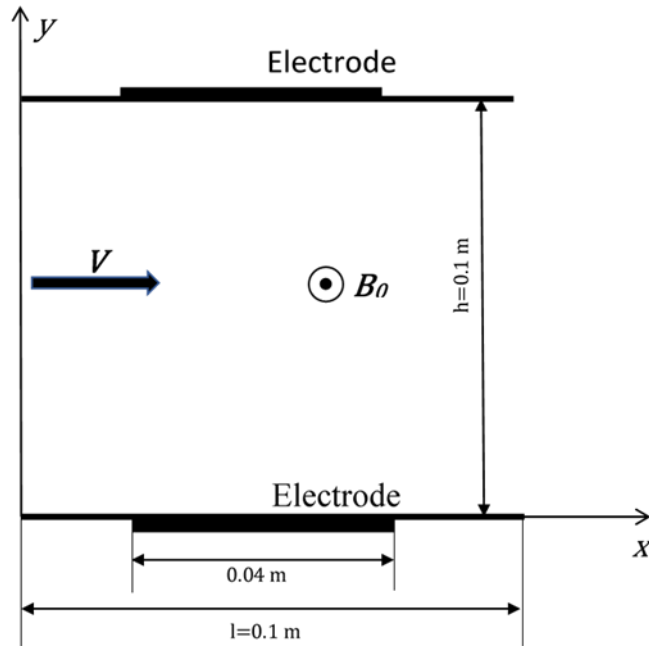


Figure 2. MHD channel flow through singly-paired electrodes.

The conductive flow has a uniform electrical conductivity σ_0 of $20 \Omega^{-1}m^{-1}$. This study utilizes a structured mesh with $300 \times 160 \times 1$ cells. The top and bottom walls are assumed to be adiabatic. The air is considered as a thermally perfect gas and the free-stream conditions are as follows:

$$T_\infty = 1000 \text{ K}, \quad p_\infty = 1.00 \times 10^5 \text{ Pa}, \quad V_\infty = 2535.75 \frac{\text{m}}{\text{s}}, \quad \gamma = 1.4, \quad Kn = 2.79 \times 10^{-6}$$

The magnetic induction is imposed along the z -axis and is set to 0.5 T . The current continuity solver assumes Dirichlet boundary conditions on the electrodes and the electric potential on the top and bottom electrodes is specified to be -30 V and 30 V , respectively.

Figure 3 and 4 show the contours of the electric potential with $\beta = 0$ and 1, obtained using the mixed assembly given by Eq. (3.31). The results capture the Hall effect and are in good agreement with Ref. [79]. Figures 3 and 4 show that the potential difference between the two electrodes is evidently smaller than between the insulators, due to the establishment of an electric current connecting the electrodes and the release of charged particles. Figure 4 additionally shows that the Hall effect, as anticipated, introduces asymmetry into the distribution of the electric potential.

In Figure 5, we compare between the distributions of electric potential for $\beta = 1$ at $x = 0.05m$ given by the mixed assembly and by the edge-based assembly with correction term. The CFL for both cases is 96. Figure 6 shows the convergence curves of the mixed assembly for $\beta = 1, 5, 20$ and the edge-based assembly for $\beta = 1$, all with a CFL = 96. It is shown that for lower values of the Hall parameter, the two assembly approaches have similar results and convergence behavior. However, when the Hall parameter is increased, the convergence behavior of the edge-based assembly is affected by the correction term, and the CFL has to be reduced. For $\beta = 20$, the simulation using the edge-based assembly fails to converge even at very low CFLs. On the other hand, the mixed assembly converges with high CFL (96), even for $\beta = 20$. As shown in Figure 6, the convergence of the simulations with the mixed assembly is substantially slower for larger Hall parameters, requiring 21,000 iterations for 1 order of magnitude drop for $\beta = 20$, while a 7-order magnitude drop takes only 4,000 iterations for $\beta = 1$. The slower convergence behavior for larger β can be explained by examining Eq. (2.20): as β increases, the off-diagonal elements of σ become nontrivial and eventually grow to a magnitude comparable with their diagonal counterparts, hence the Jacobian of the resulting linear system ceases to be diagonally-dominant, negatively affecting the convergence rate.

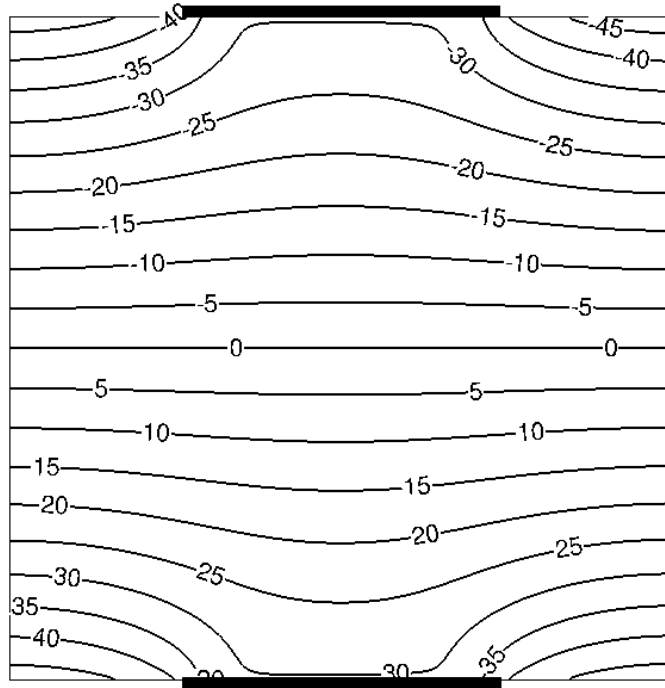


Figure 3. MHD channel flow through singly-paired electrodes: electric potential (V) contours between the electrodes with $\beta = 0$.

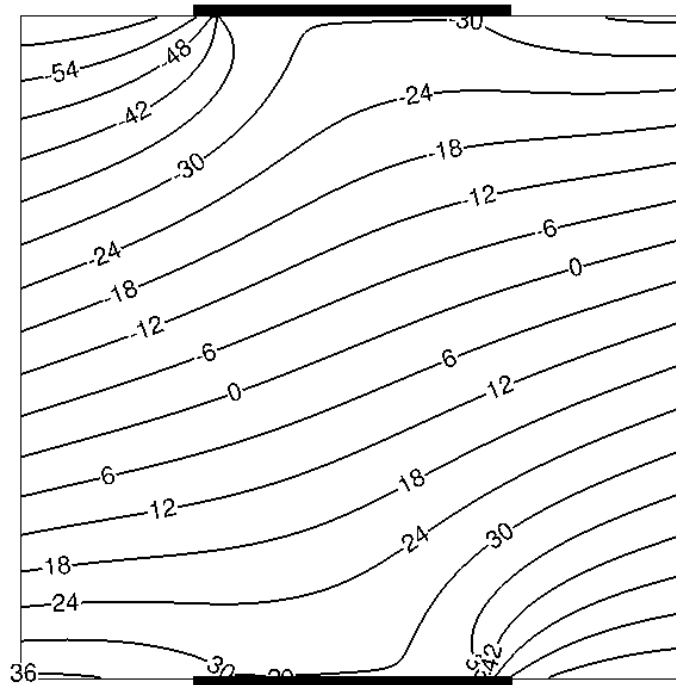


Figure 4. MHD channel flow through singly-paired electrodes: electric potential (V) contours between the electrodes with $\beta = 1$.

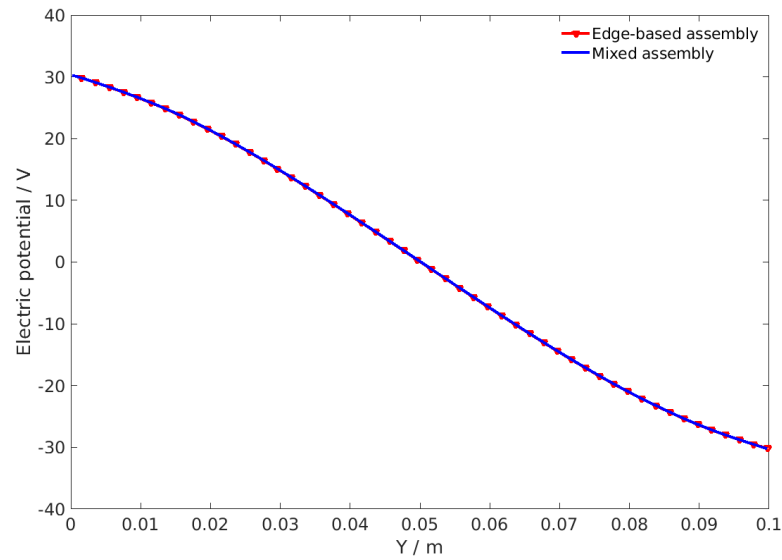


Figure 5. MHD channel flow through singly-paired electrodes: electric potential distribution at $x = 0.05m$ with $\beta = 1$.

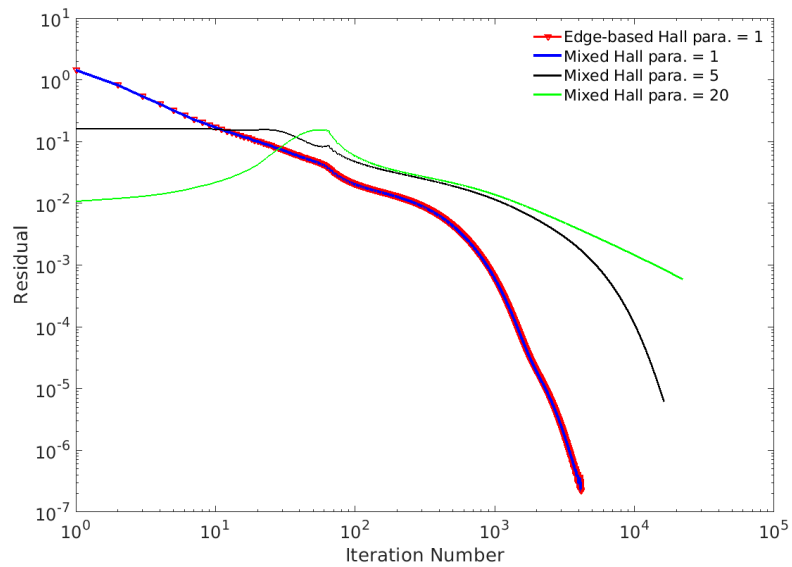


Figure 6. MHD channel flow through singly-paired electrodes: convergence history for $\beta = 1, 5, 10$.

4.2 Mach 5 Inviscid Flow Past a Sphere

In the second test case, a Mach 5 inviscid flow past a sphere is simulated under the effect of an imposed magnetic dipole. The sphere radius is $r_0 = 10 \text{ mm}$ and the properties of the free stream are

$$T_\infty = 100 \text{ K}, p_\infty = 1587 \text{ Pa}, \rho_\infty = 0.055 \text{ kg m}^{-3}, \sigma_\infty = 794 \text{ } \Omega^{-1}\text{m}^{-1}, V_\infty = 1022 \text{ m s}^{-1}, \gamma = 1.4, \\ Kn = 9.29 \times 10^{-5}$$

The electric conductivity is assumed to be uniform in the entire domain, and equal to its free stream value. The imposed magnetic field is created by a dipole mounted at the center of the sphere, expressed as:

$$\mathbf{B} = \frac{\mu_0[3\mathbf{r}(\mathbf{r} \cdot \hat{\mathbf{m}}) - r^2\hat{\mathbf{m}}]M}{4\pi r^5} \quad (4.35)$$

where:

$$M = \frac{2\pi B_0 L^3}{\mu_0}, \mathbf{r} = (x, y, z)^T \text{ and } r = \sqrt{x^2 + y^2 + z^2}$$

with $\hat{\mathbf{m}} = (1, 0, 0)^T$, a unit vector denoting the direction of the dipole moment and the origin of the Cartesian system of coordinates being at the center of the sphere. The boundary conditions for the electric potential are as follows: the electric potential at the far boundary (inlet) is set to 0 V , while on the outflow boundary and on the sphere surface, the current is assumed to flow along the boundary, namely,

$$\mathbf{j} \cdot \mathbf{n} = 0.$$

Numerical results are presented in terms of the non-dimensional Stuart number:

$$St = \frac{\sigma_\infty B_0^2 r_0}{\rho_\infty V_\infty} \quad (4.36)$$

This non-dimensional group, also known as Stuart number, measures the ratio of electromagnetic forces to inertial ones and is varied here by setting the value of the imposed magnetic field intensity B_0 . The applied magnetic field in the center of the sphere is provided in Table 1. The CFL starts at 1 and is exponentially increased to 50 within 100 Newton iterations.

St	0	1	2	3	4	5	6
$B_0 [T]$	0.000	2.642	3.737	4.577	5.285	5.909	6.472

Table 1. Strength of applied dipole for Mach 5 inviscid flow over a sphere.

Grid independence is studied using a coarse mesh containing 171,105 nodes and 163,840 hexahedral bi-linear elements (G2, Figure 7), and a fine mesh containing 1,339,585 nodes and 1,310,720 elements (G3). In Figure 8, the static temperature profiles along the stagnation line are plotted for $St = 0$ (no imposed magnetic field) and $St = 6$. While a finer mesh (G3) is more effective in terms of shock sharpness, the differences between the two meshes are imperceptible. We therefore proceed with the coarser mesh (G2) for the sake of computational efficiency.

As described in Section 3.1, the edge-based discretization introduces a correction term:

$$\sum_{j \in Ki} H_{ij} \frac{s_j^l - s_i^l}{2}$$

In Figure 9, the impact of this term is investigated by plotting the static temperature profiles across the shockwave for $St = 6$. No observable difference is found when neglecting the correction term.

In Figures 10, 11 and 12, the contours of static temperature, pressure and Mach number are shown for $St = 0$ and $St = 6$. Under the influence of an increasing electromagnetic body force, the bow shock standoff distance is significantly increased.

To demonstrate the effects of the induced electric field, the electric potential and the three components of the electric field are exhibited in Figure 13. The electric potential is non-uniform only in regions close to the sphere surface and the resulting electric field is therefore non-zero only in these regions. The induced electric field generally enhances MHD heat-shield. Figure 14 reports the shock standoff distance, made non-dimensional with radius, as a function of the Stuart number. The results obtained with the standard low-magnetic Reynolds number approximation and the simplified version (neglecting the induced electric field) are compared with the literature [4, 27, 28]. Results of the simplified low-magnetic Reynolds number approximation are in reasonable agreement with those of Poggie and Gaitonde [4]. When St is increased from 0 to 6, the shock standoff distance shows an increase of 70%. This is as expected since both are performed without considering the induced electric field. When the induced electric field is accounted for, an 87% increase in shock standoff distance is observed for $St = 6$.

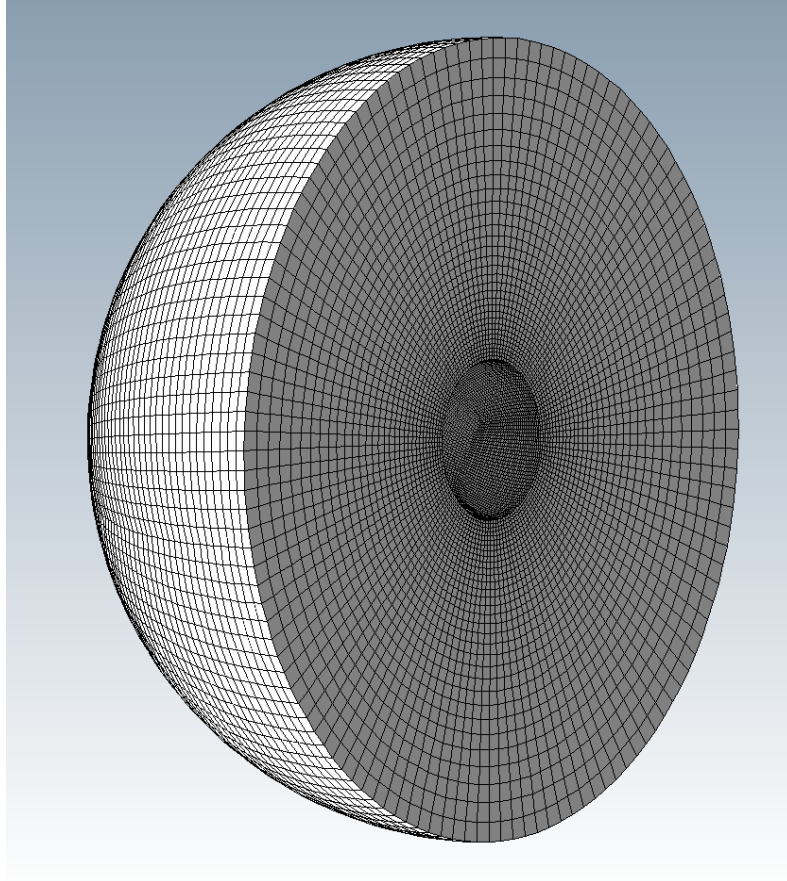


Figure 7. Mach 5 inviscid flow past a sphere:
coarse mesh (G2).

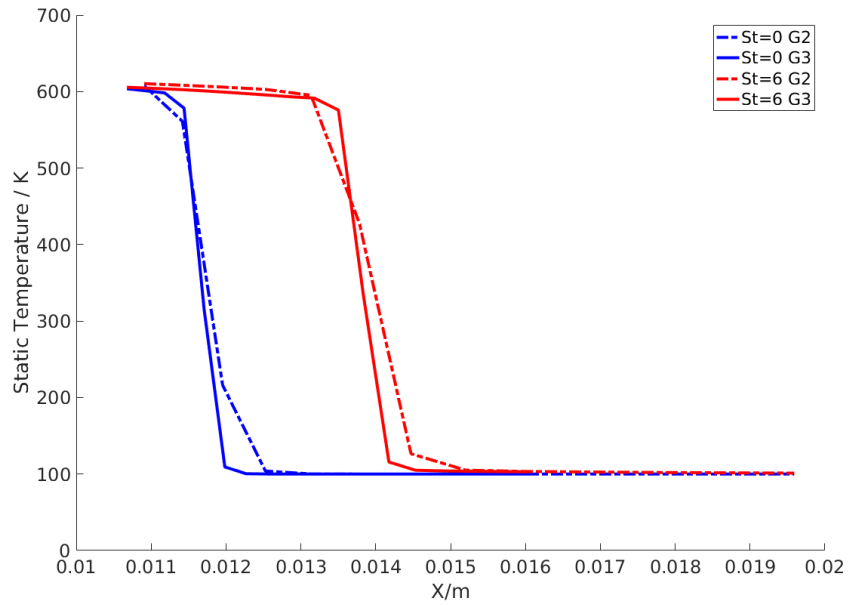


Figure 8. Mach 5 inviscid flow past a sphere:
comparison of static temperature across the shock with different meshes.

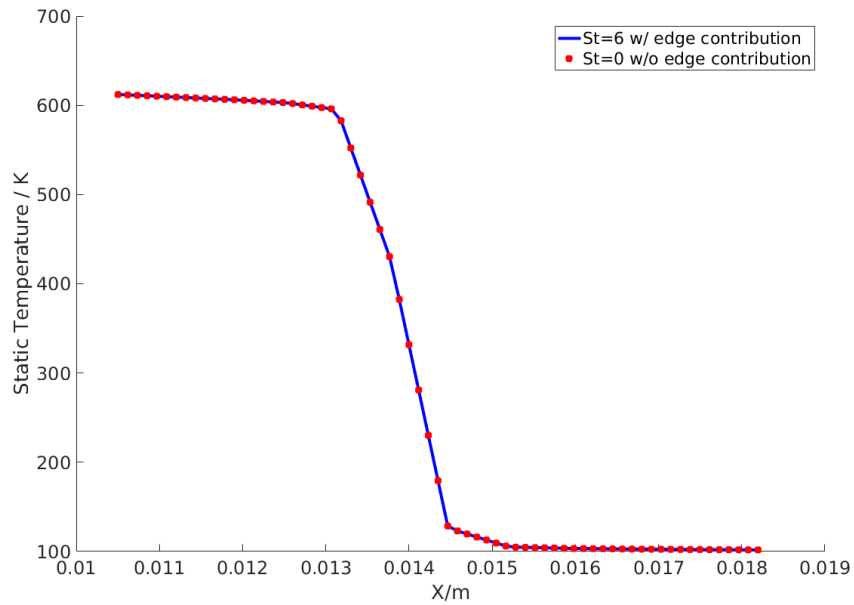


Figure 9. Mach 5 inviscid flow past a sphere:
comparison of static temperature across the shock with/without the edge-based correction term.

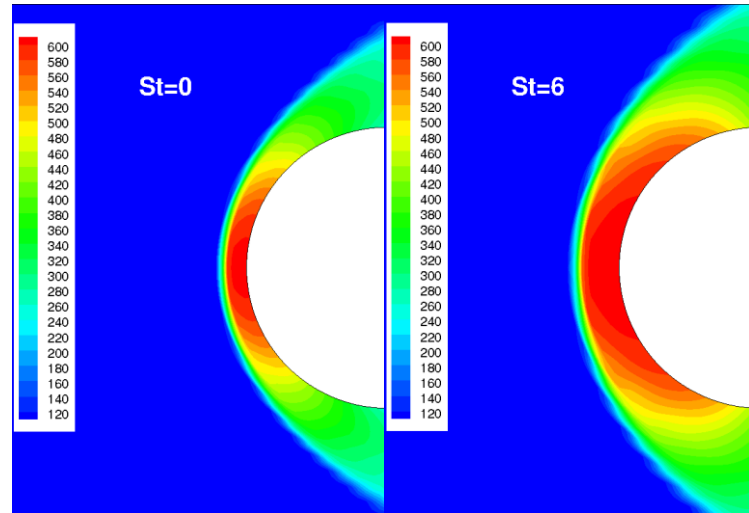


Figure 10. Mach 5 inviscid flow past a sphere:
contour plots of static temperature (K) for $St = 0$ and $St = 6$.

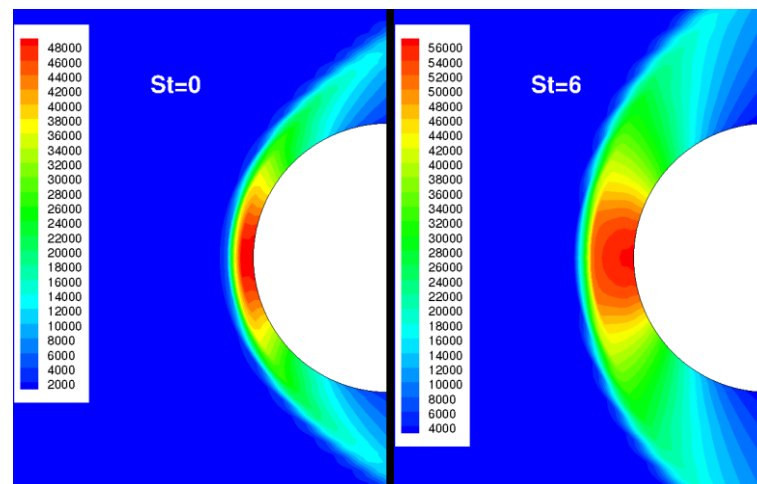


Figure 11. Mach 5 inviscid flow past a sphere:
contour plots of pressure (Pa) for $St = 0$ and $St = 6$.

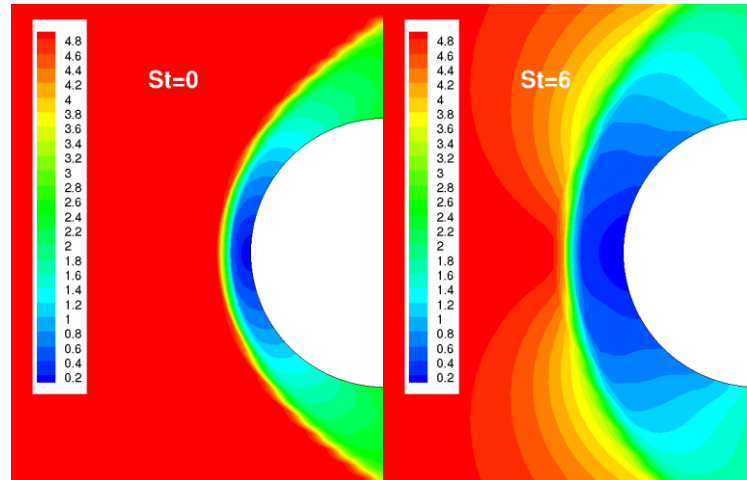


Figure 12. Mach 5 inviscid flow past a sphere:
contour plots of Mach number for $St = 0$ and $St = 6$.

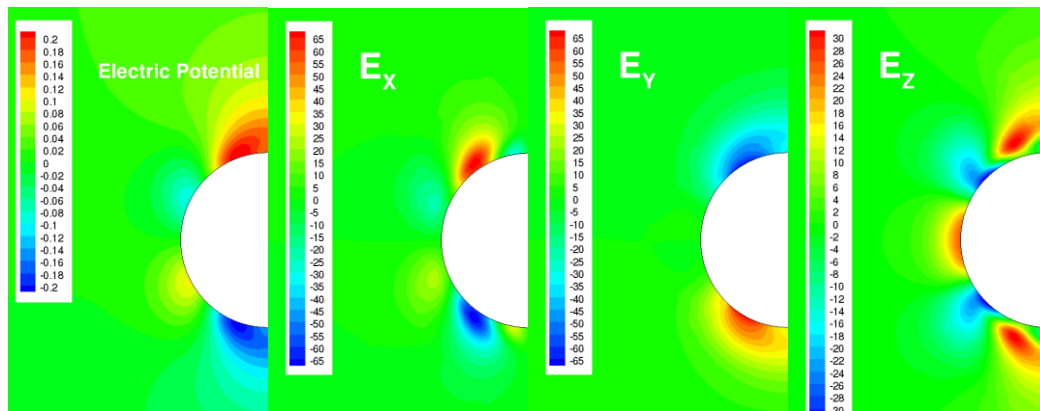


Figure 13. Mach 5 inviscid flow past a sphere:
contour plots of electric potential (V) and induced electric field (V/m) for $St = 6$.

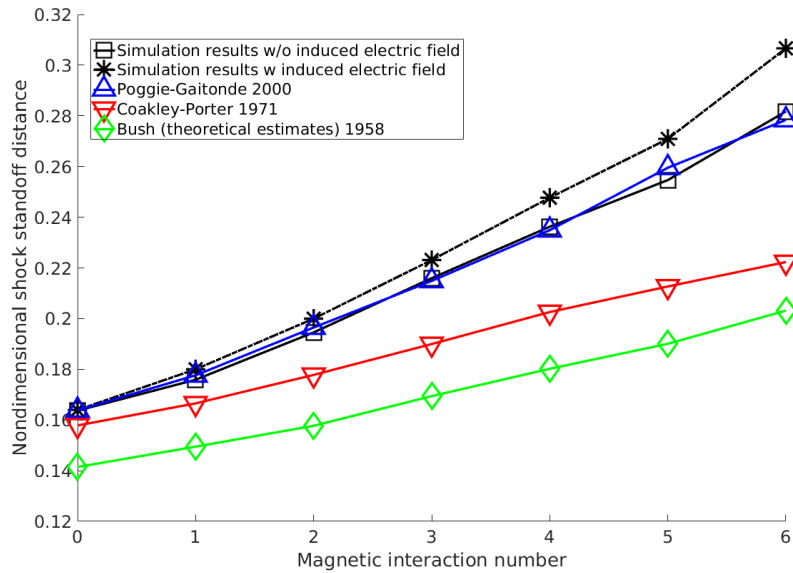


Figure 14. Mach 5 inviscid flow past a sphere: shock standoff distance against Stuart number.

The convergence of the numerical results can be assessed, as in Figure 15, via the L_2 norm of the residual R vs. Newton iterations for $St = 6$. After 78 iterations the residual drops approximately 4 orders of magnitude, which is sufficient for inviscid flows.

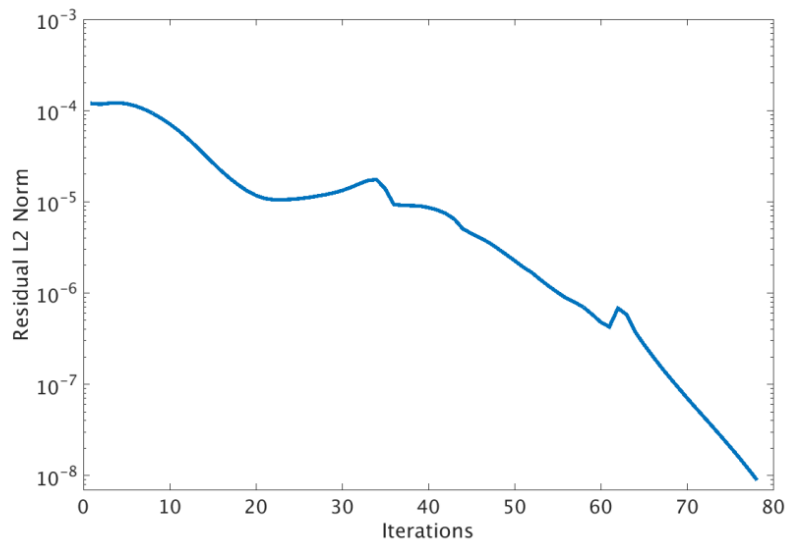


Figure 15. Mach 5 inviscid flow past a sphere: L_2 norm of residual vs. Newton iterations $St = 6$.

4.3 Mach 4.75 Laminar Flow Past a Sphere

The third test case is a Mach 4.75 laminar flow of Argon past a sphere. The radius of the sphere is $r_0 = 38.1 \text{ mm}$ and a hybrid mesh consisting of 196,686 tetrahedral elements and 224,074 nodes is shown in Figure 16. The inset in Figure 16 highlights the prismatic layers of 365,760 elements used to resolve the boundary layer. The mesh ought to be fine enough to demonstrate the effect of Stuart number on standoff distance. For more quantitative answers, mesh optimization as used in [60] should be employed and is introduced in Section 4.4.

The free stream conditions are

$$T_\infty = 1100 \text{ K}, p_\infty = 27.8 \text{ Pa}, \rho_\infty = 1.214 \times 10^{-4} \text{ kg m}^{-3}, V_\infty = 3 \times 10^3 \text{ m s}^{-1}, \gamma = 1.4, Kn = 2.92 \times 10^{-2}$$

The electric conductivity of Argon is set to [80]:

$$\sigma(T) = 3.34 \times 10^{-10} \frac{\alpha}{\beta \sqrt{T}}$$

where:

$$\alpha = 0.00623 \text{ and } \beta = 5 \times 10^{-17} \text{ cm}^2$$

The free stream electric conductivity is thus

$$\sigma_\infty = 1254.78 \text{ } \Omega^{-1} \text{ m}^{-1}$$

The imposed magnetic field and the boundary conditions of the electric potential are the same as in the previous test case. The Reynolds number based on the sphere radius is $Re = 148$ and a laminar flow assumption is justified. The CFL starts at 0.01 and is exponentially increased to 20 within 50 Newton iterations. An isothermal boundary condition is imposed at the wall by setting $T_w = 300 \text{ K}$. As in the previous test case, numerical results are presented in terms of the non-dimensional Stuart number.

Figures 17, 18 and 19 show the contours of static temperature, pressure and Mach number for $St = 0$ and $St = 6$. The applied magnetic field in the center of the sphere is provided in Table 2. As for the inviscid case, the bow shock is significantly pushed away from the surface under the influence of an increasing electromagnetic body force.

St	0	1	2	3	4	5	6
$B_0[T]$	0.00	0.09	0.12	0.15	0.17	0.20	0.21

Table 2. Strengths of the applied dipoles for Mach 4.75 laminar flow over a sphere.

Figure 20 shows the contours of electric potential and induced electric field. Similar to the test case of the preceding section, a non-uniform electric potential is observed only in regions adjacent to the sphere indicating that the induced electric field is nontrivial only in these regions.

Figure 21 shows shock standoff distances as a function of St . When neglecting the induced electric field, the distance varies linearly from 0.24 for $St = 0$, to 0.48 for $St = 6$; a 75% increase. If the induced electric field is taken into account, the increase in shock standoff is even more salient and a 100% increase is observed for $St = 6$. To the best of the author's knowledge, no results are available in the literature to compare against for this case.

In Figure 22 the peak heat flux at the stagnation point is plotted against St , non-dimensionalized with its value at $St = 0$. A quasi-linear rate decrease is observed up to $St = 6$, at which point a 13% reduction in the peak heat flux has been achieved.

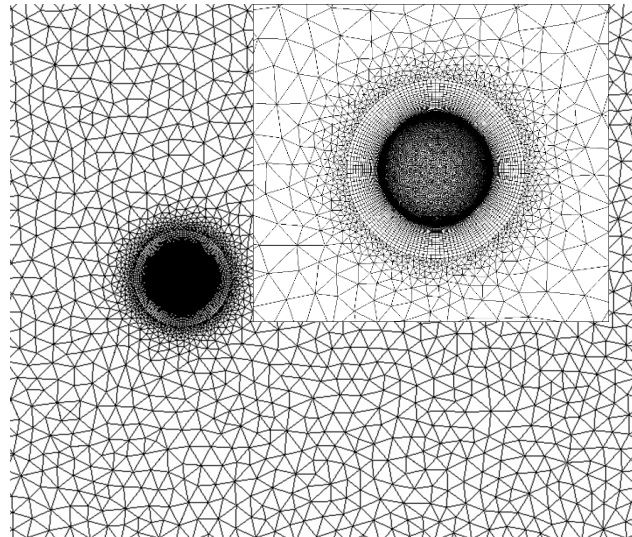


Figure 16. Mesh used for the simulation of Mach 4.75 laminar flow past a sphere.

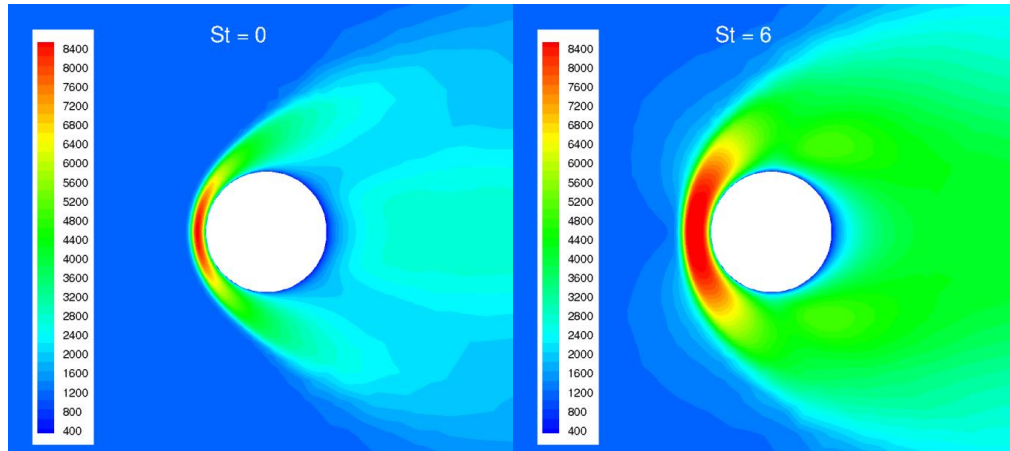


Figure 17. Mach 4.75 laminar flow past a sphere:
contour plots of temperature (K) at $St = 0$ and $St = 6$.

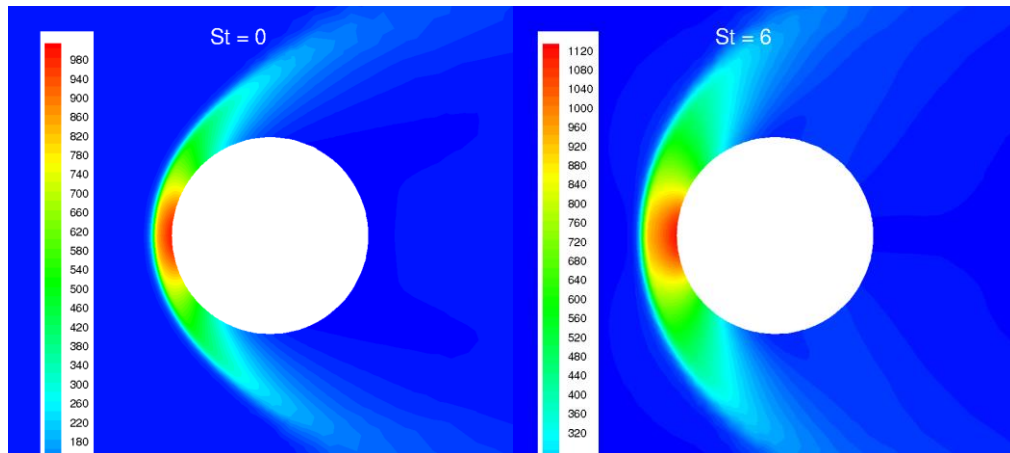


Figure 18. Mach 4.75 laminar flow past a sphere:
contour plots of pressure (Pa) at $St = 0$ and $St = 6$.

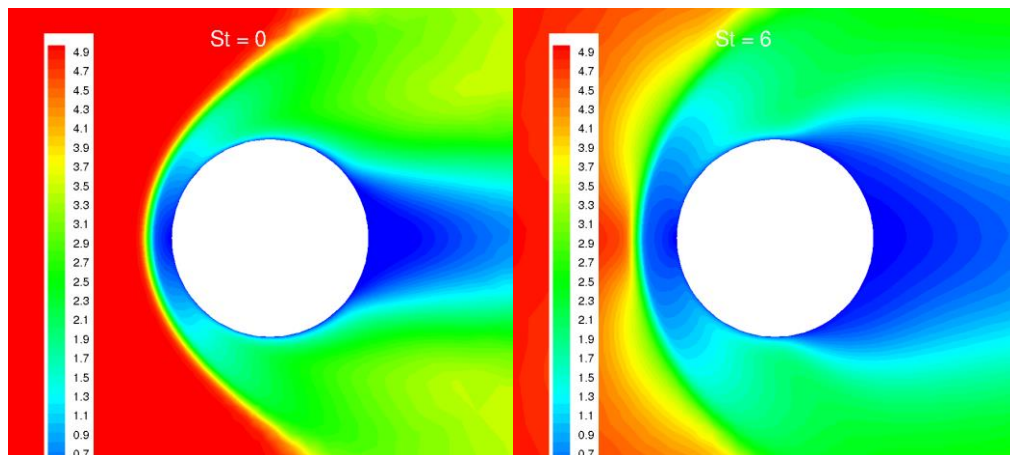


Figure 19. Mach 4.75 laminar flow past a sphere:
contour plots of Mach number at $St = 0$ and $St = 6$.

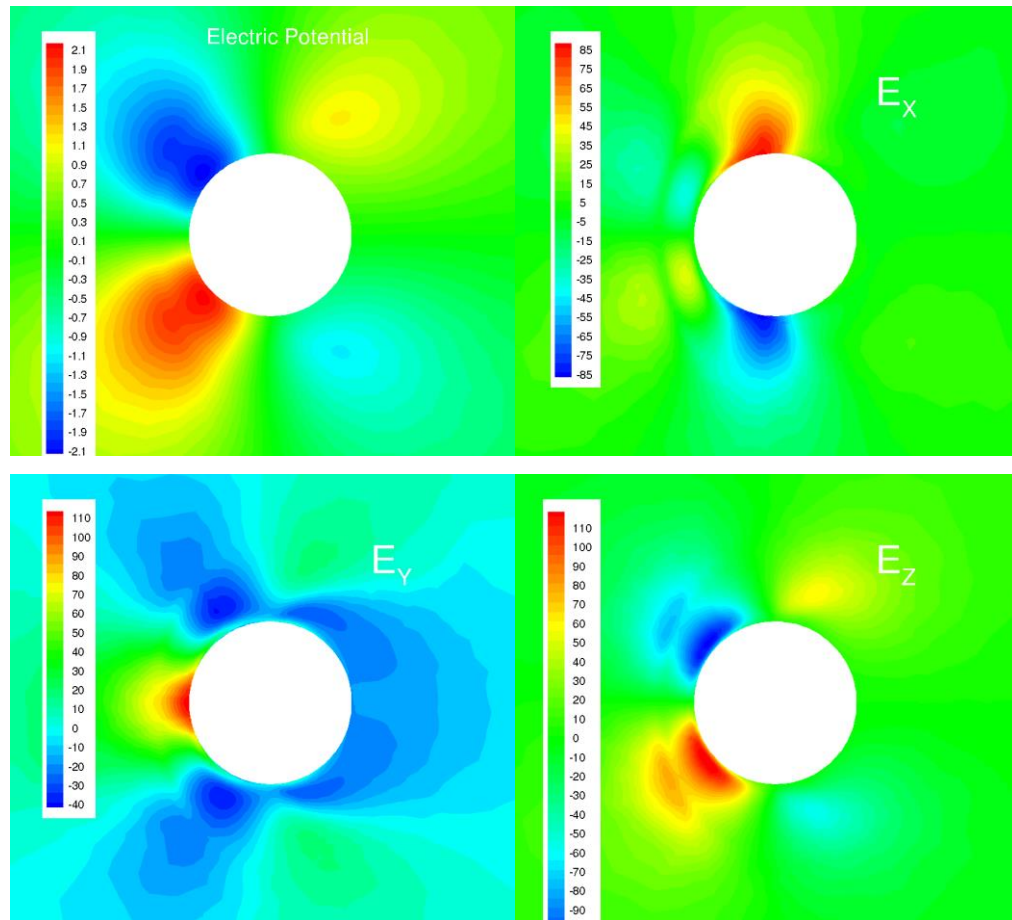


Figure 20. Mach 4.75 laminar flow past a sphere: contour plots of electric potential (V) and the induced electric field (V/m) for $St = 6$.

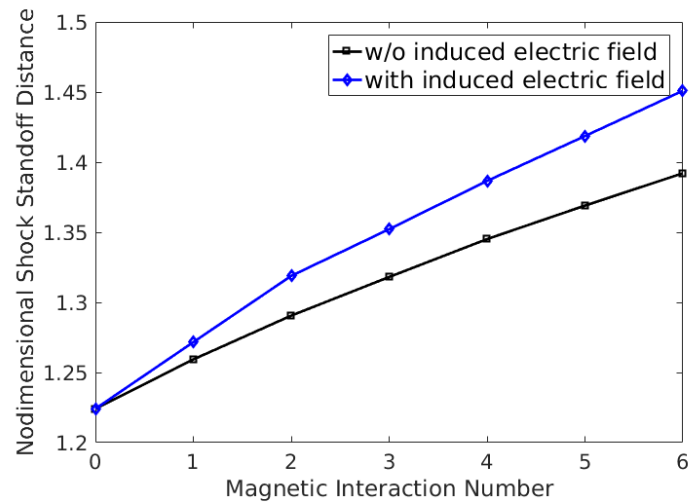


Figure 21. Mach 4.75 laminar flow past a sphere: shock standoff distance in terms of the Stuart number, St .

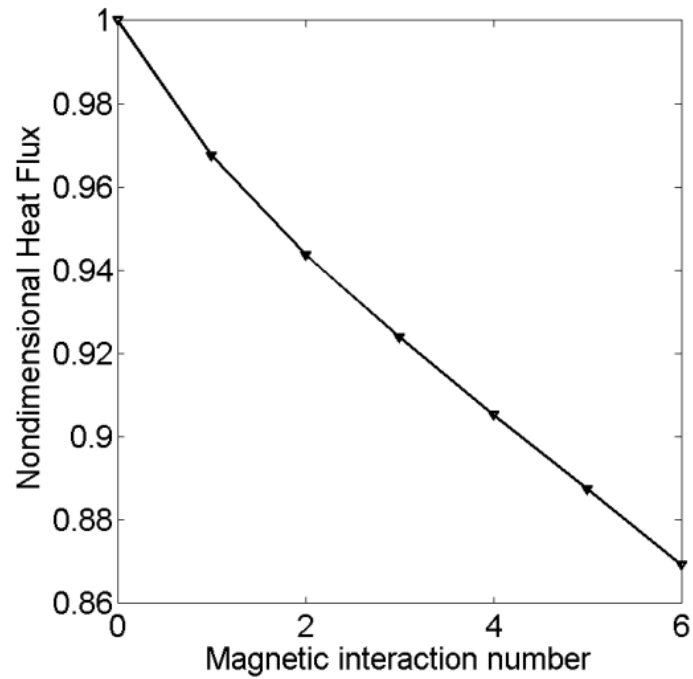


Figure 22. Mach 4.75 laminar flow past a sphere: peak heat flux in terms of the Stuart number, St .

Convergence has also been assessed for this viscous test case. As an example, Figure 23 shows the L_2 norm of the residual R , in terms of Newton iterations for $St = 6$. A reduction of 5

orders of magnitude in the residual is achieved after 130 iterations, which is satisfactory for a low-Reynolds number flow.

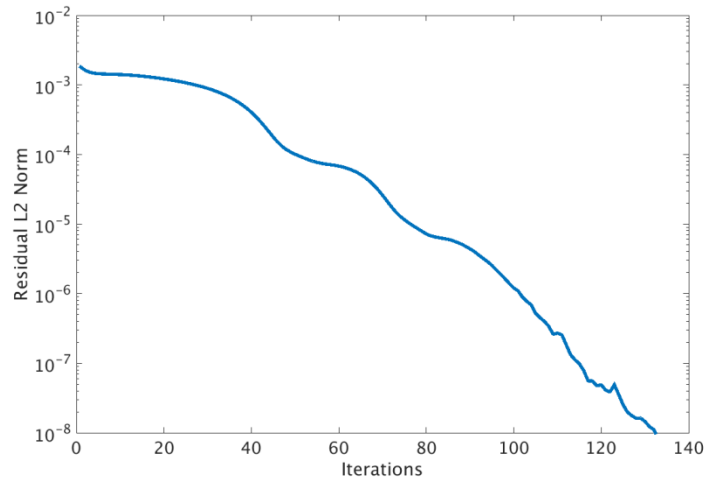


Figure 23. Mach 4.75 laminar flow past a sphere: L_2 norm of residual in terms of Newton iterations.

4.4 Introducing Anisotropic Mesh Optimization

The simulations presented in Sections 4.2, as well as the majority of other hypersonic simulations, are performed on structured grids. In Section 4.2, though an unstructured grid is utilized, the grid remains isotropic with no shock-grid alignment. It is known that poor shock-grid alignment induces an artificial vorticity in the post-shock region that is transported downstream eventually affecting wall solutions. Since the shock locations cannot be known *a priori* for arbitrary problems, aligning the shock with the grid is difficult when generating a grid, and impossible in the presence of a multi-shock system. Therefore, most examples in the literature employing structured grids are given for simple geometries, *e.g.* cones, spheres and cylinders.

To overcome this serious limitation, an anisotropic mesh optimization algorithm (OptiGrid, a code developed by the McGill CFD Lab) [81] is used in conjunction with the flow solver. OptiGrid can be used for both structured [47] and unstructured meshes [59, 82]. OptiGrid starts with the premise that mesh enrichment based on gradients is impractical in 3D because the resulting grids become very large and do not really optimize any global solution metric. Hence, some directionality must be introduced in order to intelligently not only refine edges but also coarsen and swap them, as well as move nodes, where needed. OptiGrid uses the truncation error

as a measure of directional refinement, which is the true difference between the partial differential equation and its discretized form for linear elements. The truncation error, being proportional to the second derivatives on linear elements, has nine components forming a Hessian, \mathbf{H} . The eigenvalues of \mathbf{H} give a measure of the relative length of an edge, and its eigenvectors specify the ideal orientation of the edge. A posteriori error measure can be expressed in an edge-based fashion as

$$error(\mathbf{x}_i - \mathbf{x}_j) = \int_0^1 \sqrt{(\mathbf{x}_i - \mathbf{x}_j)^T \mathbf{M}(l) (\mathbf{x}_i - \mathbf{x}_j)} dl$$

where \mathbf{x}_i and \mathbf{x}_j are two endpoints of an edge and \mathbf{M} is the absolute value of \mathbf{H} . In practice, \mathbf{M} is approximated by post-processing the solution on a fixed background mesh. The error is then equally distributed among the edges by resorting to node movement, edge-face-swapping, mesh refinement and coarsening. The error estimator transforms the mesh from a Cartesian space to a Riemannian space. Uniformly distributing errors produces an isotropic Delaunay mesh in the Riemannian space, but a highly stretched anisotropic mesh in the Cartesian space that is automatically aligned with any number of shocks [82]. This is because the tetrahedral elements perpendicular to the shock are refined, and parallel to the shock are coarsened. In Figure 24, an arbitrary unstructured grid, together with a manufactured solution with uniform second order derivative yields a uniform grid in Cartesian space, clearly illustrating the converse mechanism. Unlike gradient-based mesh optimizers, OptiGrid introduces a crucial edge dimension effect and directional effect (anisotropy) based, respectively, on the eigenvalues and eigenvectors of the solution Hessian. This allows a much finer resolution of complex flow phenomena such as multiple shocks, most importantly without necessarily increasing the mesh size nor using higher order interpolation. Even more important is that minimal time is spent generating the initial grid: it will be optimized no matter what the starting mesh is and will always converge to the same solution [60].

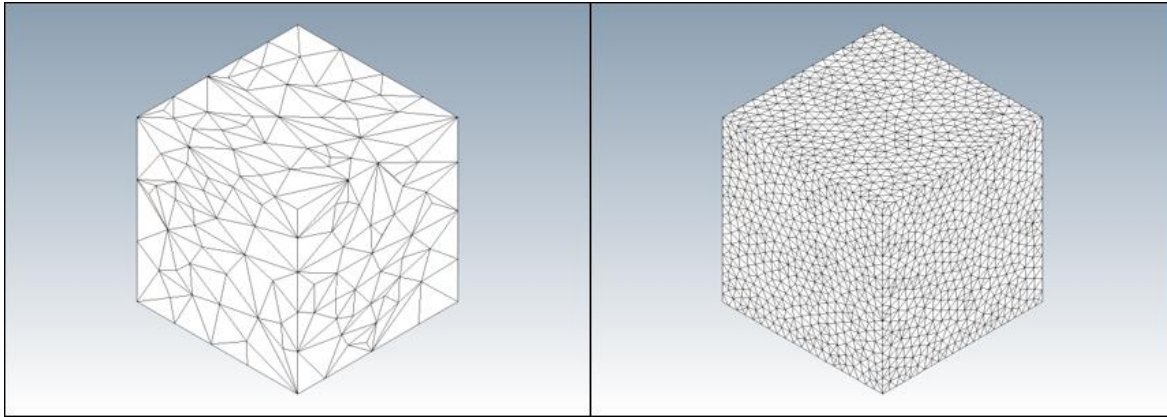


Figure 24. Arbitrary grid of a box (left); optimized grid based on a solution with uniform second order derivative (right).

Given an initial flow solution, OptiGrid performs the aforementioned node and edge operations according to eigenvalues and eigenvectors obtained from the Hessian of the error estimator of the evolving solutions. It does this in three dimensions, while respecting the original CAD if nodes on the surface are moved. A user-selected (typically 8-10) number of adaptation iterations are performed. During each iteration, the error estimate computed over the grid resulting from the previous one is interpolated over the newly optimized grid. When the optimization process is completed, the solution is updated by solving the governing equations over the new grid. The new solution is then fed back to the optimization code and the cycle repeated until a prescribed number of global adaptation cycles is reached (typically 4 or 5).

In OptiGrid, two options are available: optimizing to a specified error level in the solution domain or optimizing to a fixed number of mesh points i.e. giving the user the best solution for his/her money. In Sections 4.2-4.7, the second option is chosen to keep the number of mesh points bounded. It will be clearly demonstrated that mesh optimization not only enables a much better accuracy on unstructured meshes, but is perhaps the only way that makes possible the use of unstructured meshes to accurately predict aerodynamic and thermal loads of hypersonic vehicles of arbitrary shape.

Magnetohydrodynamics is multidisciplinary compared to CFD, with the flow and EM fields not aligned in space because of the disparity in their length scales. Mesh optimization solely based on the flow or on the EM solution is thus likely to cause insufficient resolution of the variables excluded from adaptation, which in turn adversely affects the variables for which the

grid is optimized. In Sections 4.6 and 4.7, the mesh optimization methodology is comprehensively modified to simultaneously optimize the grid for curvature of the geometry even before the start of a CFD calculation, the flow variables (pressure, density, temperature, turbulence and velocity), as well as the EM variable of interest (the electric potential).

4.5 Apollo-like Re-entry Capsule

The fourth test case is the turbulent flow over an Apollo command module-like (AS-202) re-entry geometry. As shown in Figure 25, the outer mold line (OML) consists of a spherical section (forebody in the flow-oriented nomenclature) of radius of curvature of 4.694 m with a shoulder radius of 0.196 m , and an afterbody consisting of a 33-degree conical section blunted to a 0.231 m radius at the aft end. The maximal diameter of the capsule is 3.912 m and the axial length, including the TPS material, is 3.431 m . The origin is at the intersection between the spherical section and the x-axis.

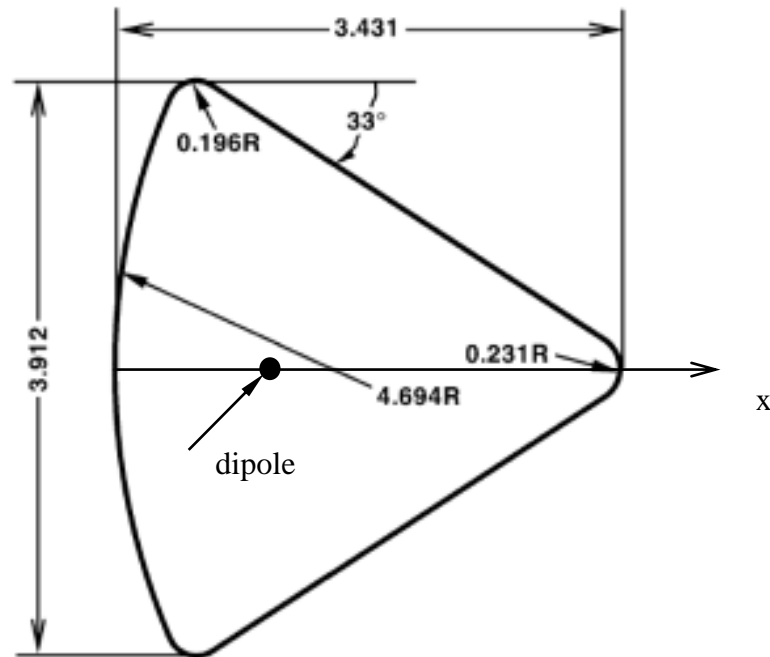


Figure 25. Apollo-like re-entry capsule:
schematic drawing of the outer mold line of AS-202 taken from [83].

The chosen re-entry conditions are at an angle of attack of 18.6° and a Mach number of 13.26 . The capsule temperature is set to $T_w = 8500\text{ K}$. The air being considered a thermally perfect gas, the free-stream conditions are as follows:

$$T_\infty = 268 \text{ K}, p_\infty = 61.53 \text{ Pa}, \rho_\infty = 8 \times 10^{-4} \text{ kg m}^{-3}, V_\infty = 4350 \text{ m s}^{-1}, \gamma = 1.4, Kn = 2.44 \times 10^{-5}$$

The electric conductivity is uniform and set to:

$$\sigma = 794.00 \text{ } \Omega^{-1} \text{ m}^{-1} \text{ [4]}$$

The imposed magnetic field is the same as in the two first test cases, mounted at ($x = 1.0, y = z = 0.0$). The Reynolds number based on the capsule length axis is $Re = 800,000$, and the Spalart-Allmaras turbulence model is used with a 10^{-5} free-stream ratio of Eddy turbulent viscosity to laminar viscosity.

The geometry of the test case is complex with anticipated challenging flow characteristics that are unknown a priori, making anisotropic mesh adaptation methodology an absolute necessity. Herein, mesh optimization is carried out for 4 cycles, with the agglomerated adaptation criteria being the Hessian of density ρ , pressure p , temperature T and turbulent viscosity μ_t . Figure 26 shows the initial mesh and the mesh after four adaptation cycles, for a Stuart number $St = 0$. The initial original mesh is composed of 909,713 nodes, with 526,273 tetrahedral elements and 1,626,088 prisms, whereas the adapted one is composed of 1,145,647 nodes with 1,527,658 tetrahedral elements and 1,732,112 prisms. One can notice the vast improvement in the solution, with only a 10% increase in nodes but with “directionality” taken into consideration, as opposed to an unguided mesh refinement scheme in which points are blindly increased in all directions or even locally enriched which would require one to know the location of all singular phenomena such as shocks and boundary layers.

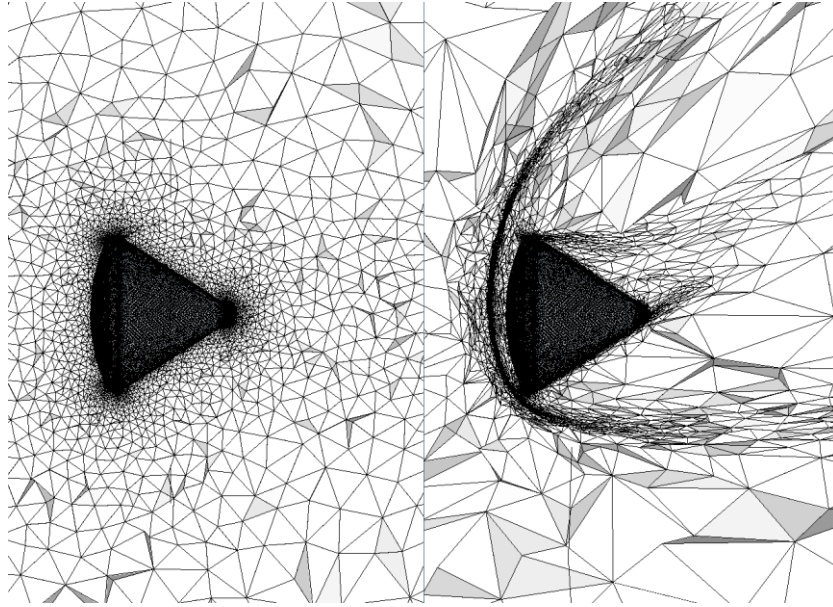


Figure 26. Apollo-like re-entry capsule:

initial mesh (left) and optimal one (right) after 4 adaptation cycles, $St = 0$.

In this case ($St = 0$), the CFL starts at 0.01 and is progressively increased to 0.5 in 1,500 iterations. Figure 27 shows the static temperature contours for $St = 0$ obtained from the initial mesh (left) and from the adapted one (right). It is clear that after mesh adaptation the shock-capturing is considerably improved since the mesh is realigned with the shock adding grid points in regions of highest truncation error.

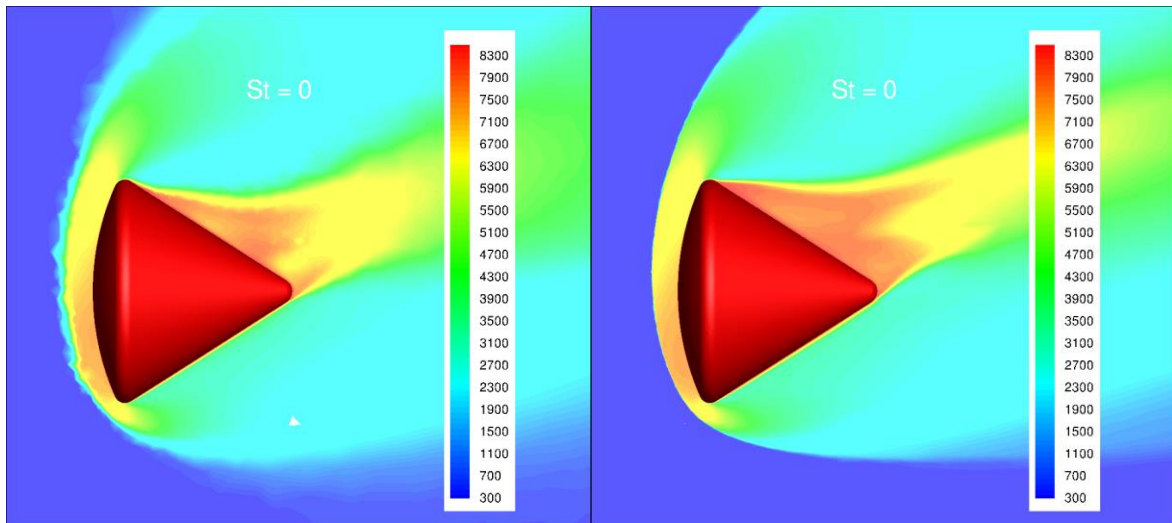


Figure 27. Apollo-like re-entry capsule:

contour plots of temperature for $St = 0$, with the initial mesh (left) and with the adapted one (right), expressed in Kelvins.

In Figure 28, the adapted meshes after 4 cycles are contrasted for $St = 0$ (1,145,647 nodes, 1,527,658 tetrahedral elements and 1,732,112 prisms) and $St = 6$ ($B_0 = 0.1622 T$), demonstrating how the mesh adaptation takes into consideration the local physics. Not only is the shock location captured well, but also the larger wake structure generated by the magnetic dipole.

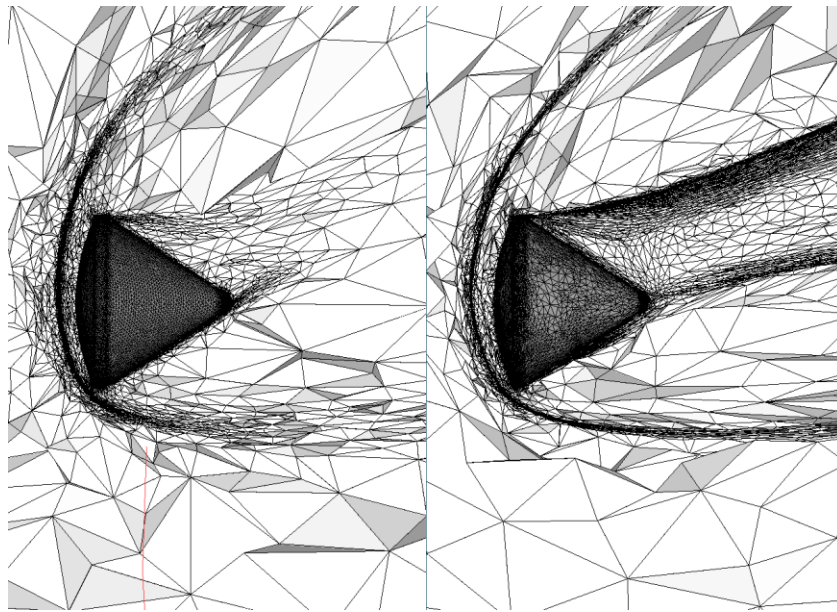


Figure 28. Apollo-like re-entry capsule: meshes after 4 adaptation cycles for $St = 0$ (left) and $St = 6$ (right).

In this case ($St = 6$), CFL starts at 0.01 and is increased to 0.1 in 1,500 iterations. Figure 29 shows the static temperature contours for $St = 6$ obtained with the initial mesh (left) and with the adapted one (right). Figure 30 displays the contours of pressure and Mach number for $St = 6$ with the adapted mesh.

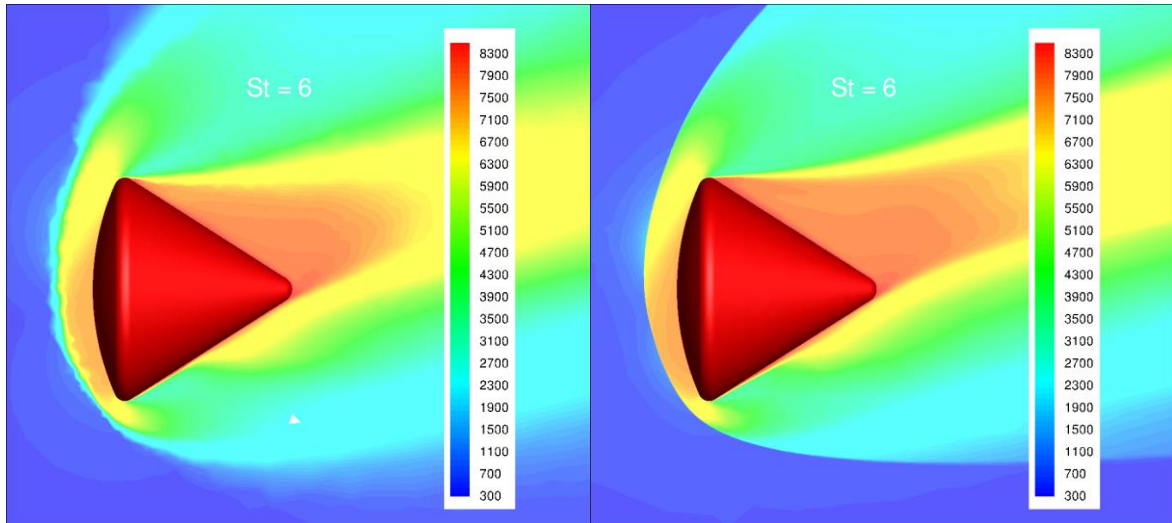


Figure 29. Apollo-like re-entry capsule: contour plots of temperature for $St = 6$, with the initial mesh (left) and with the adapted one (right), expressed in Kelvin.

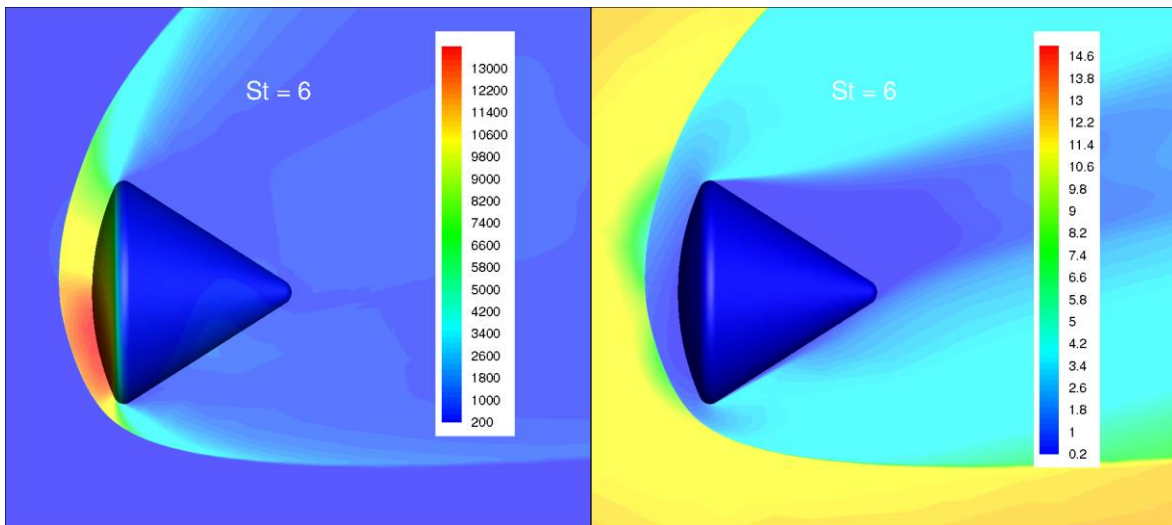


Figure 30. Apollo-like re-entry capsule: contour plots of pressure (Pa, left) and Mach number (right) for $St = 6$.

In Figure 31 the distribution of the static pressure across the shock wave is shown. The usefulness and the efficiency of the mesh adaptation methodology are clearly put into evidence in this figure. Without increasing the number of mesh points, the adapted mesh not only captures the shock with superior accuracy and sharpness (Figure 31), but also significantly improves the resolution of other complex flow features such as the expansion fans, the free shear layer and the base recirculation (Figures 29 and 30). On the other hand, the shock-mesh misalignment of the

initial mesh produces poorly resolved shock and induces oscillations in the surface heat flux distribution.

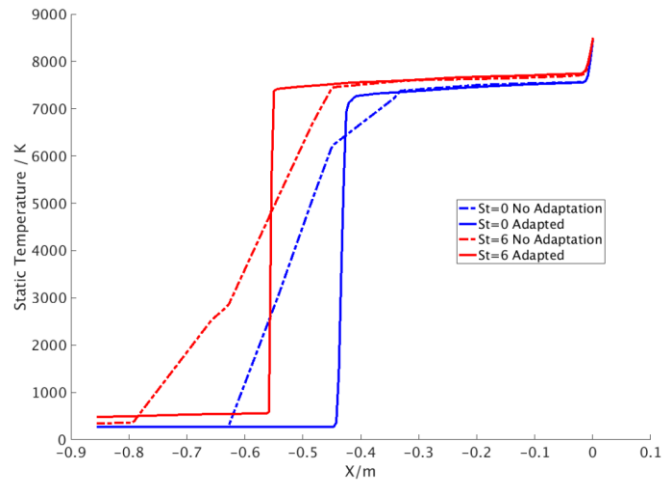


Figure 31. Apollo-like re-entry capsule: static temperature across the shock wave, expressed in Kelvins.

Figure 32 illustrates non-dimensional (with respect to the forebody diameter) shock standoff distances as a function of St . When neglecting the induced electric field, they vary linearly from 0.1176 for $St = 0$, to 0.1503 for $St = 6$, an increase of 27%. For the standard low-magnetic Reynolds number formulation, an increase of 34% is observed.

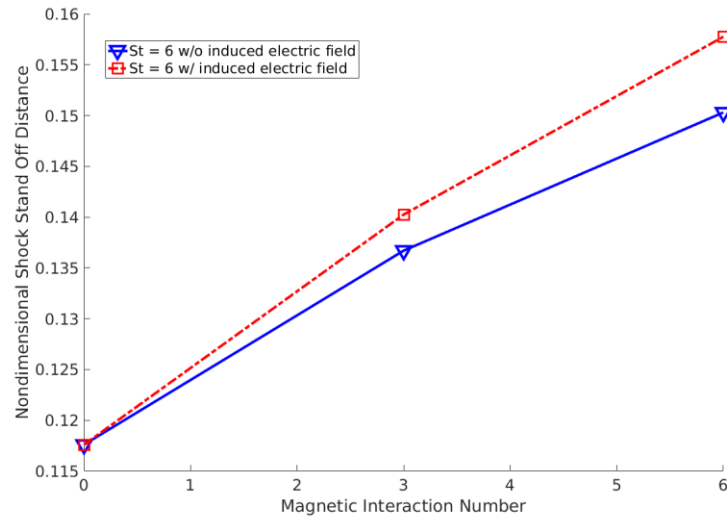


Figure 32. Apollo-like re-entry capsule:
shock standoff distance in terms of the Stuart number St for the Apollo capsule.

In Figure 33, the maximum heat flux on the capsule's surface is reported in terms of the Stuart number St . Between $St = 0$ and $St = 6$, the maximum heat flux decreases by more than 16%.

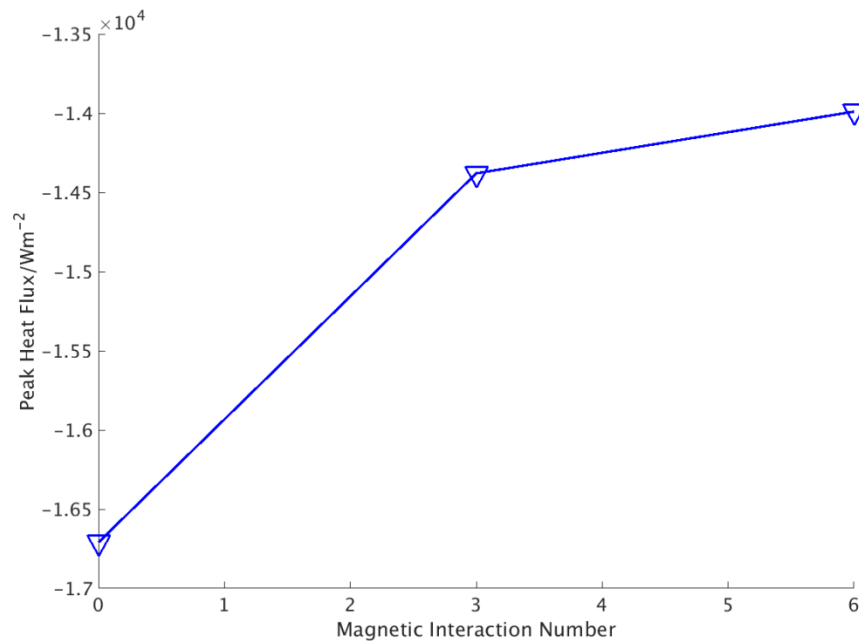


Figure 33. Apollo-like re-entry capsule:
peak heat flux in terms of the Stuart number St for the Apollo capsule.

The convergence of the numerical results is assessed in Figure 34 that shows the L_2 norm of the residual R vs. Newton iterations for $St = 6$ when the adaptive methodology is applied. A reduction of 5 orders of magnitude in the residual is achieved after 40,000 iterations, which is reasonable for such a stiff problem.

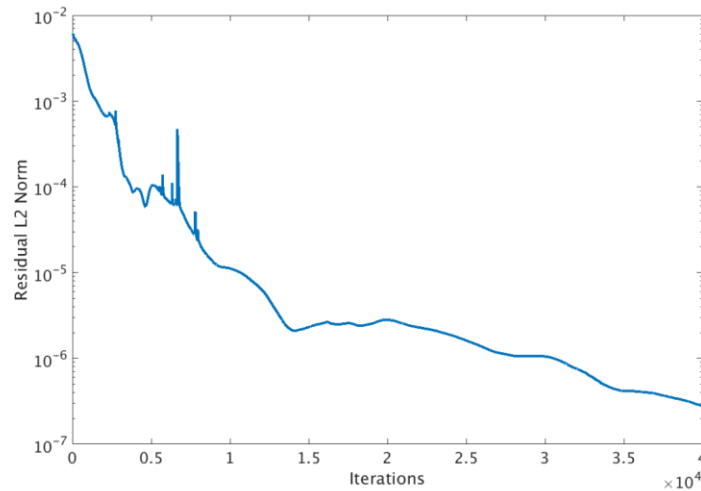


Figure 34. Apollo-like re-entry capsule:
 L_2 norm of residual in terms of Newton iterations.

4.6 Laminar Flow over a Sphere (Mach 21.38)

This test case considers laminar flow over a sphere with a radius of 1.0 m at Mach 21.38. The surface temperature is set to $T_w = 2000\text{ K}$. Air is assumed to be a thermally perfect gas, and the free-stream conditions at high altitude are as follows:

$$T_\infty = 230\text{ K}, p_\infty = 6.40\text{ Pa}, V_\infty = 6500\text{ m s}^{-1}, \gamma = 1.4, Kn = 7.52 \times 10^{-4}$$

The electrical conductivity is uniform and set to:

$$\sigma_0 = 200.00\ \Omega^{-1}\text{m}^{-1}$$

The Reynolds number based on the radius of the sphere is $Re = 42,100$. The imposed magnetic field is created by a dipole mounted at the center of the sphere, with $\hat{\mathbf{m}} = (1, 0, 0)^T$, $B_0 = 0.3\text{ T}$. The Hall parameter is set to $\beta = 10$. The boundary conditions for the electric potential are the same as in Sections 4.2 and 4.3.

To fully resolve physical quantities with such distinct time/length scales, the mesh is optimized according to the solution. Three mesh-optimization strategies are considered, all starting from an unstructured initial mesh containing 1,023,327 nodes, 906,314 tetrahedral and

1,625,712 prismatic elements. A target number of nodes (1,000,000) after adaptation is applied for all three strategies, but the adaptation criteria are different, as shown in Table 3.

Case	Optimization criteria	Final no. of nodes	Final no. of elements
Case 1	ρ, V, p, T (Flow only)	1,035,993	5,362,797
Case 2	ϕ (EM only)	1,035,185	5,374,500
Case 3	ϕ, ρ, V, p, T (Flow+EM)	1,098,972	5,578,202

Table 3. Mach 21.38 laminar flow over a sphere:
mesh adaptation setup

Figure 35 shows the convergence of the Mach number distributions along the stagnation line during the mesh optimization process for Case 3. The figure shows that the difference between the distributions starts being negligible as soon as the second optimization cycle.

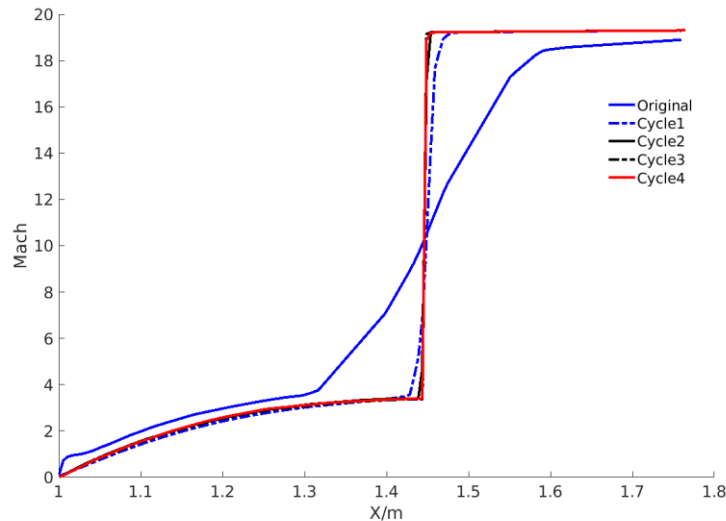


Figure 35. Mach 21.38 laminar flow over a sphere:
convergence of Mach number along stagnation line during mesh optimization (Case 3).

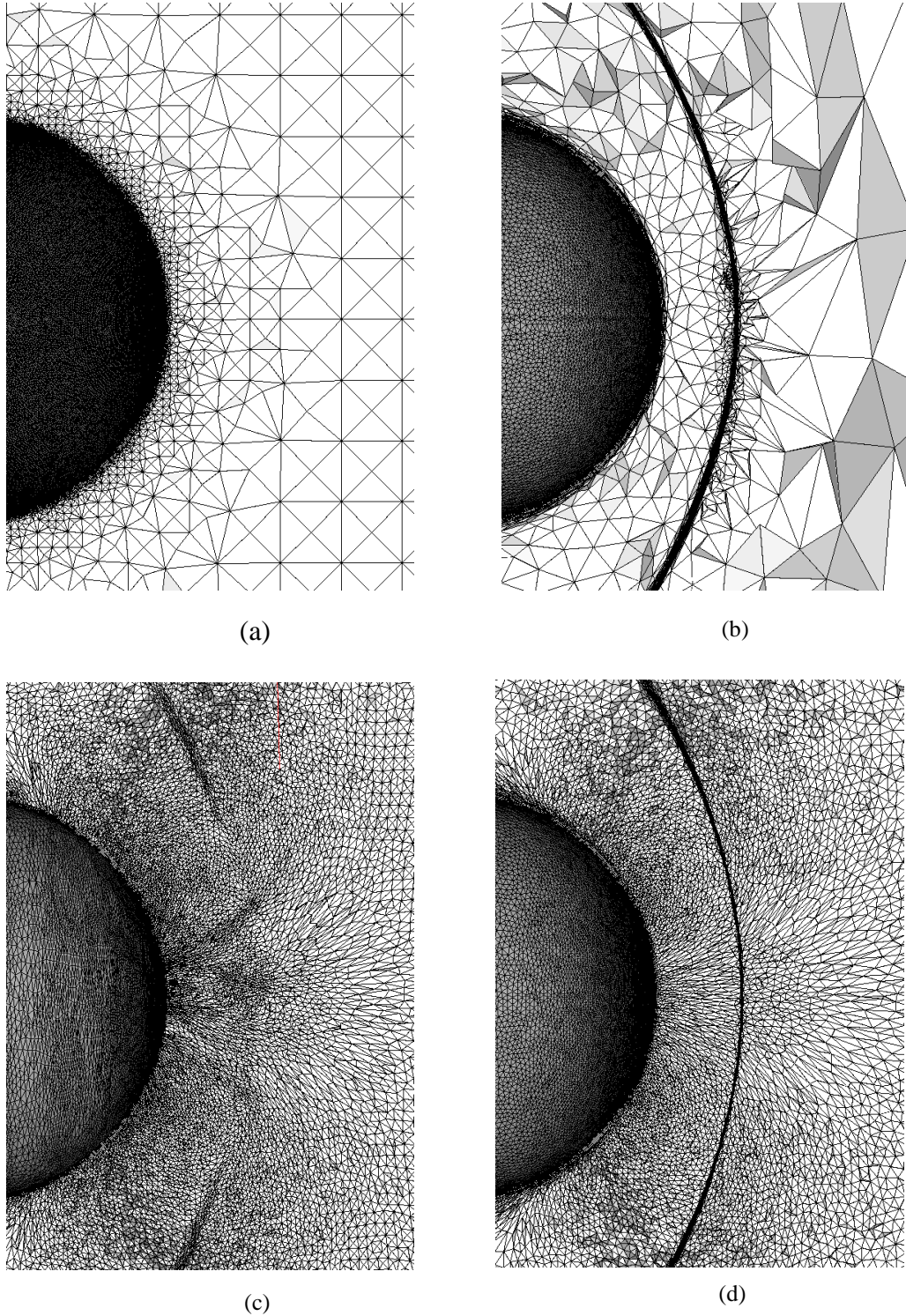


Figure 36. Mach 21.38 laminar flow over a sphere, resulting meshes with different optimization strategies:
(a) Original mesh; (b) Case 1 (Flow only); (c) Case 2 (EM only); (d) Case 3 (Flow+EM).

Figure 36 shows the original and adapted meshes. Figures 37-39 display the contours of pressure, electric potential and Mach number, respectively, obtained with these meshes. Figure 40 depicts the electric potential and Mach number distributions along the stagnation line.

It is clear that different adaptation criteria produce very different node/edge distributions for the same target number of nodes. The element size of the original octree mesh increases exponentially from the sphere surface until a prescribed maximum is reached (Figure 36(a)), appearing as a generally coarse mesh, apart from the immediate neighborhood of the surface. The coarseness of the initial mesh produces a smeared shock (Figures 37(a), 39(a) and 40(b)) and a washed-out electric potential distribution (Figures 38(a) and 40(a)). Optimization based on the flow quantities (ρ , p , V , T) alone results in better grid-shock alignment (Figure 36(b)) with nodes heavily clustered around the shock front, and coarse stretched elements upstream of the shock. While shock resolution is substantially improved (Figures 37(b), 39(b) and 40(b)) compared to the initial mesh, this adaptation strategy delivers the most disappointing resolution of the electric potential due to the coarsening and stretching of the elements (Figures 38(b) and 40(a)). Conversely, mesh optimization on the electric potential alone yields a relatively uniform mesh aligned with the oblique part of the shock, with sufficient refinement near the stagnation point (Figure 36(c)). Since a uniform electrical conductivity is assumed, the distribution of the electric potential is smooth and diffusive (Figure 38(c)), with discontinuities from the flow quantities only introduced through the $\nabla \cdot (\boldsymbol{\sigma} \cdot \mathbf{V} \times \mathbf{B})$ term in the current-continuity equation.

While adaptation on the flow field or the EM field improves the resolution of the corresponding variable, it leaves the variables omitted from the optimization compromised. Since the flow equations and the current-continuity equation are coupled through source terms, poorly resolved quantities from one field undercut the other, whether individually optimized or not at all. For instance, despite the excellent grid-shock alignment in Figure 36(b), some irregularities are observed in the dense mesh cluster straddling the shock, as well as asymmetry in the distribution of electric potential in the stagnation region (Figure 38(c)). Although Case 1 clusters the vast majority of nodes in the shock region, the resulting shock resolution is still inferior to Case 3, as shown in Figure 40(b). Moreover, due to the poor resolution of the electric potential, a substantial shift in shock location can also be observed in Figure 40(b). Optimization on both the flow and EM solution variables clearly outperforms the other strategies and, remarkably, without increasing the overall node count. Figures 37(d) and 40(b) show a crisply

resolved shock with a clean and sharp front without the irregularities of Figure 37(b), while Figure 39(d) demonstrates that the asymmetry near the stagnation point disappears.

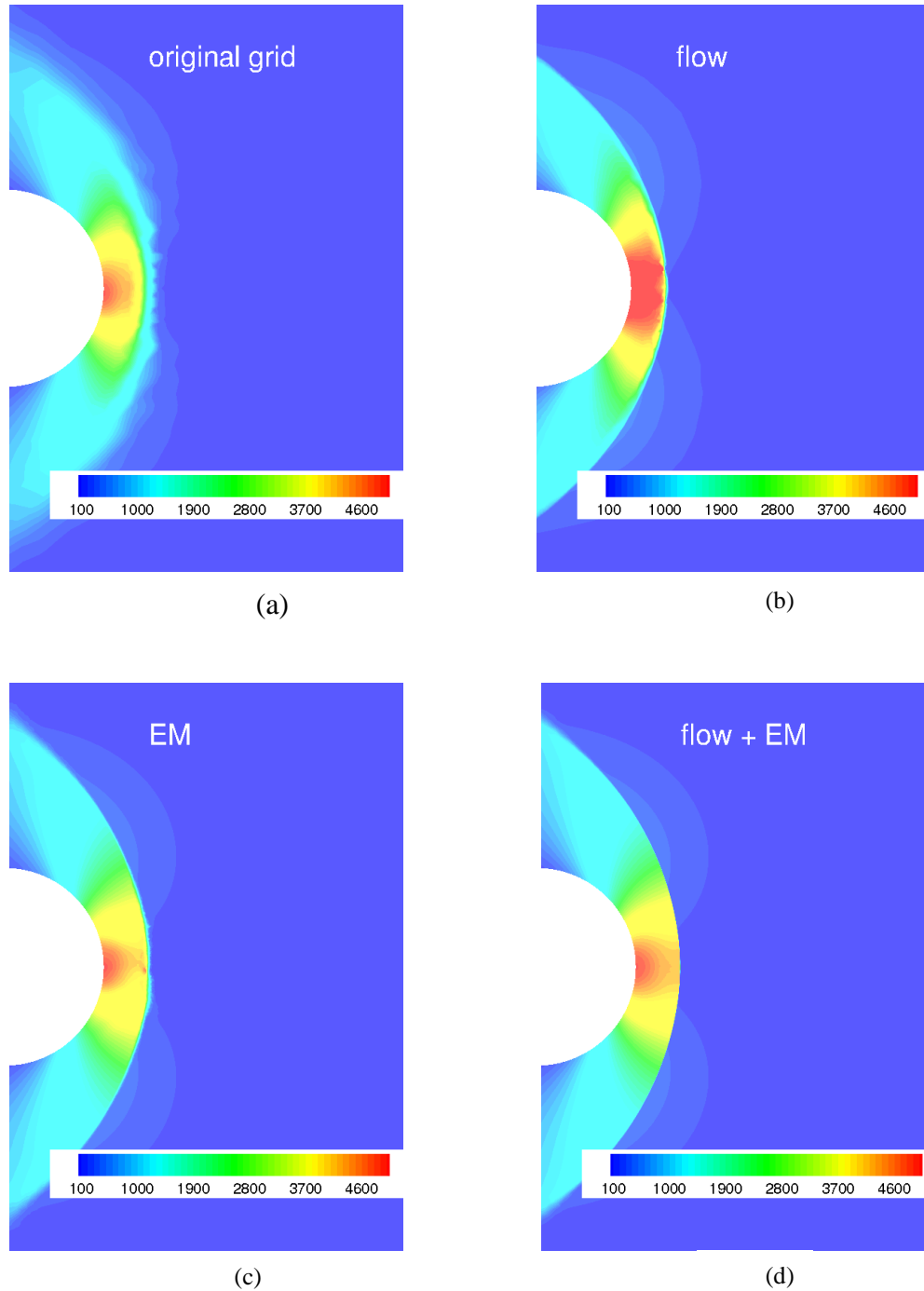


Figure 37. Mach 21.38 laminar flow over a sphere, pressure contours (Pa) obtained from the original and optimized meshes:
(a) Original mesh; (b) Case 1 (Flow only); (c) Case 2 (EM only); (d) Case 3 (Flow+EM).

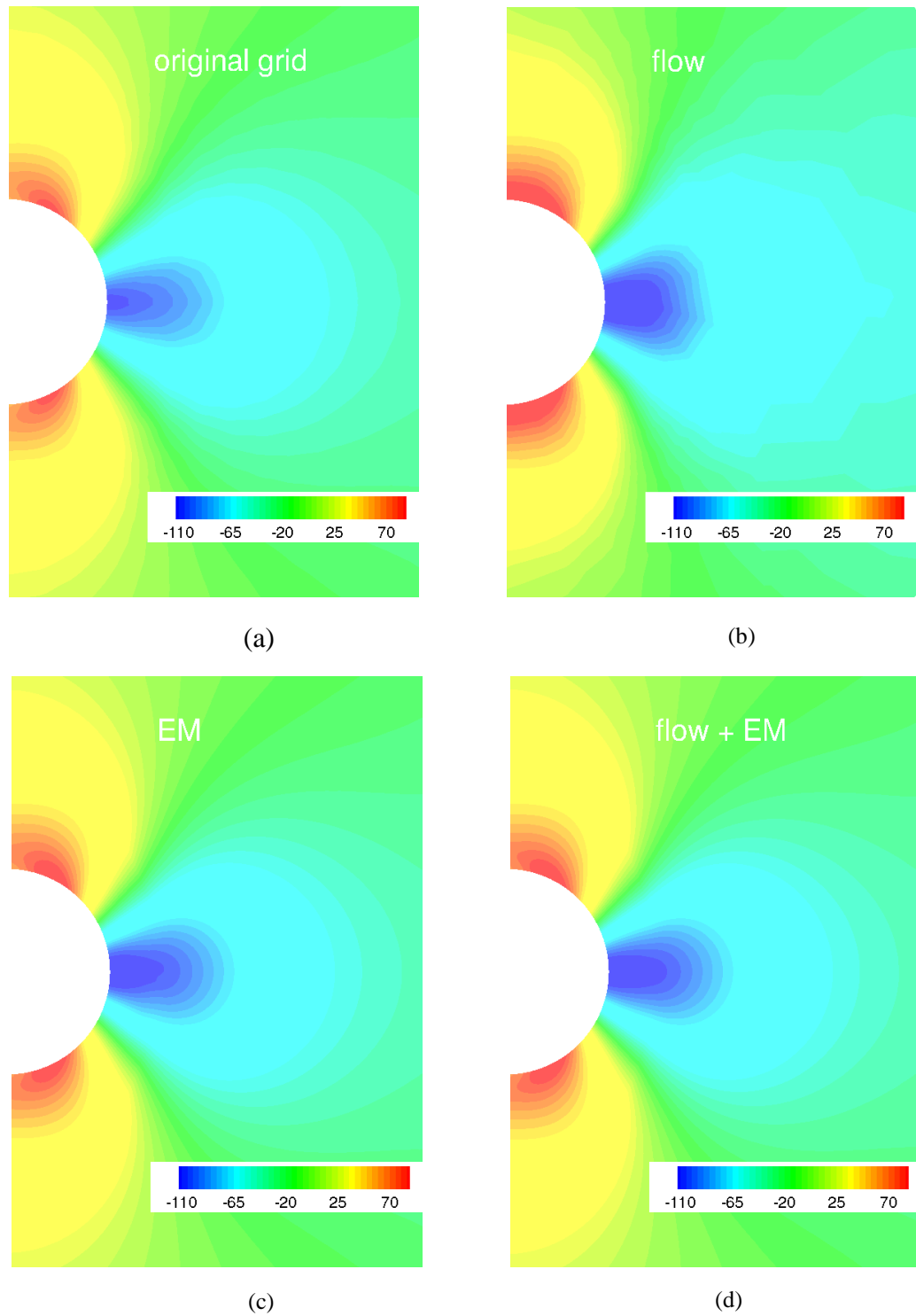


Figure 38. Mach 21.38 laminar flow over a sphere, electric potential (V) contours from original and optimized meshes:
(a) Original mesh; (b) Case 1 (flow only); (c) Case 2 (EM only); (d) Case 3 (flow+EM).

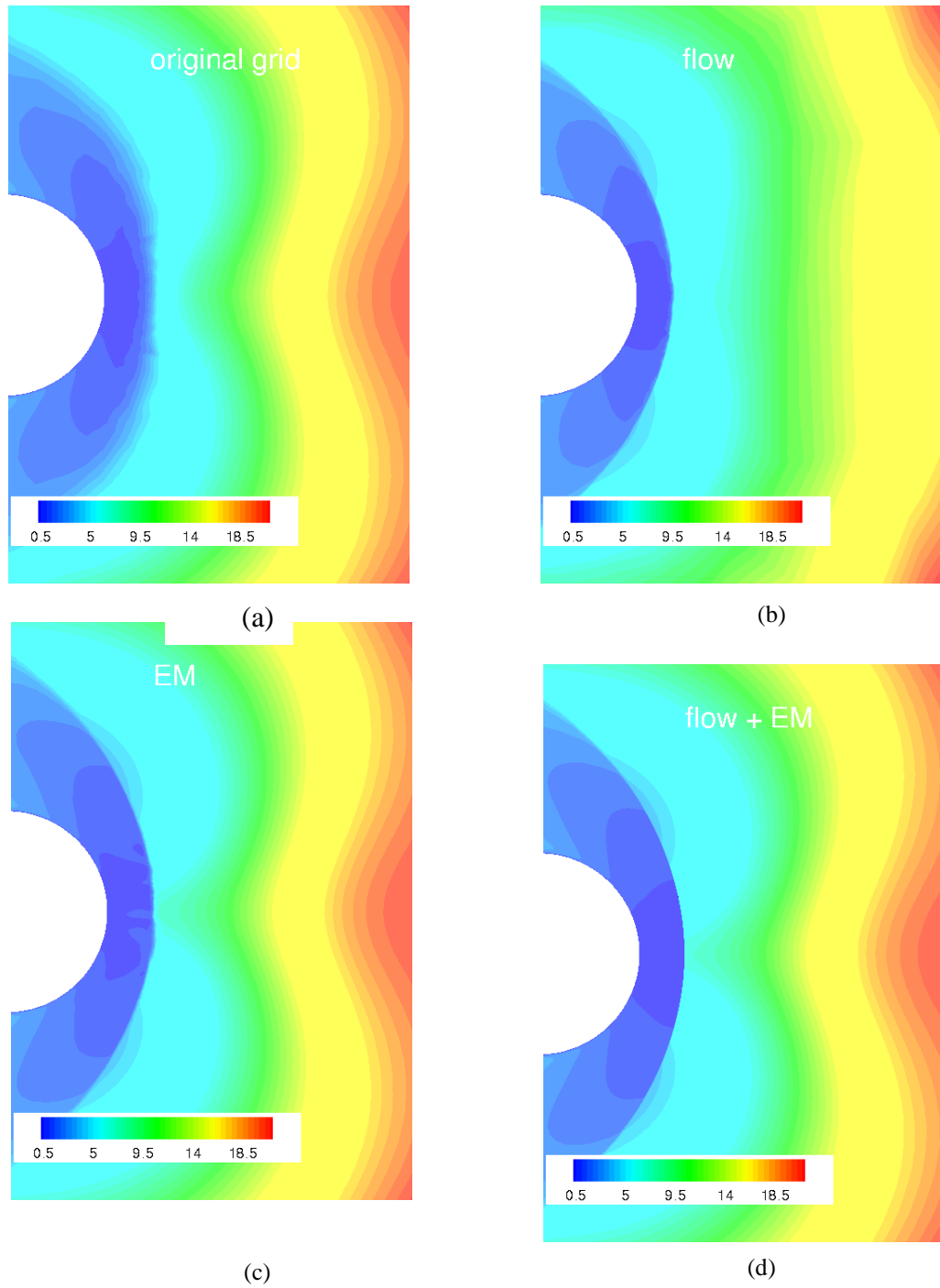


Figure 39. Mach 21.38 laminar flow over a sphere, Mach number contours from original and optimized meshes:
(a) Original mesh; (b) Case 1 (flow only); (c) Case 2 (EM only); (d) Case 3 (flow+EM).

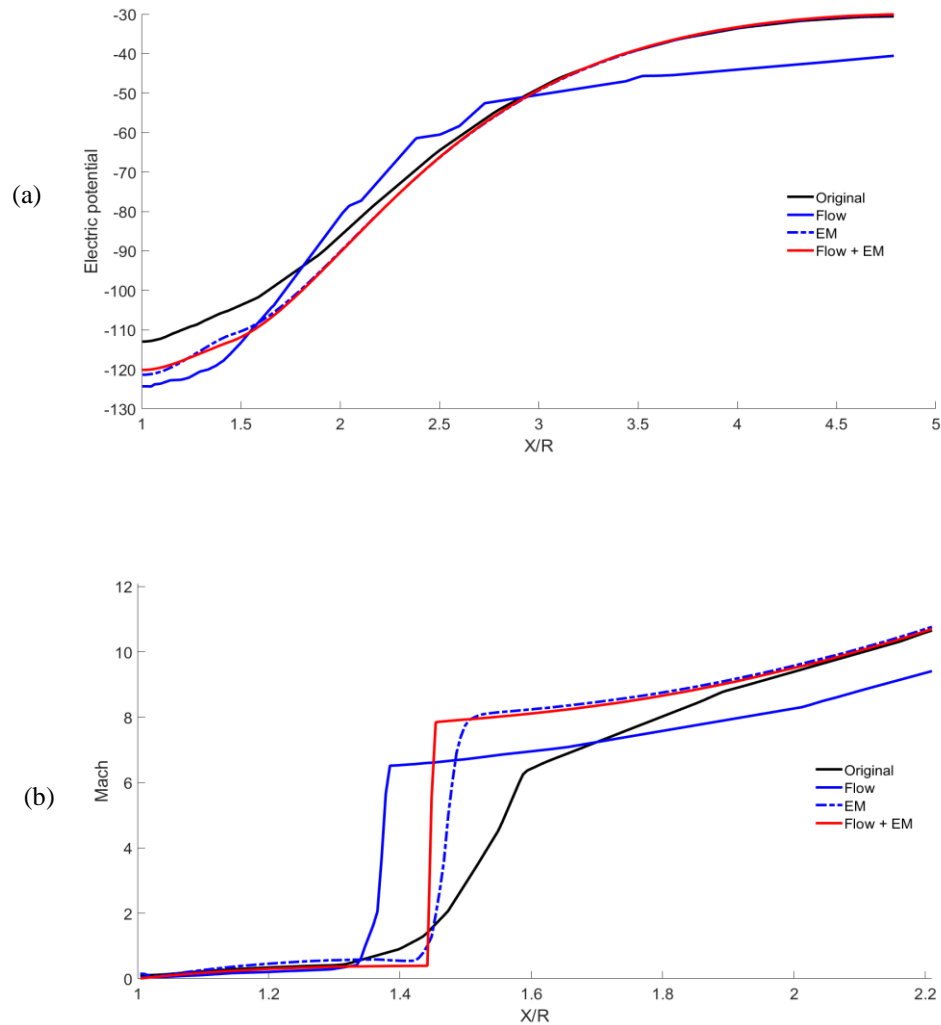


Figure 40. Mach 21.38 laminar flow over a sphere:
 (a) Electric potential and (b) Mach number distributions along stagnation line.

4.7 Turbulent Flow over Orbital Re-entry Experiment (OREX) Capsule (Mach 17.61)

The OREX capsule is considered for the simulation of hypersonic re-entry at Mach 17.61. The left side of Figure 41 shows the OREX geometry, composed of a cone with a spherical nose ($R = 1.35$ m), a circular shoulder and a rear truncated bi-conical cover, and the initial computational domain on the right. The detailed dimensions of OREX can be found in [84]. The origin of the coordinates system is at the nose of the capsule.

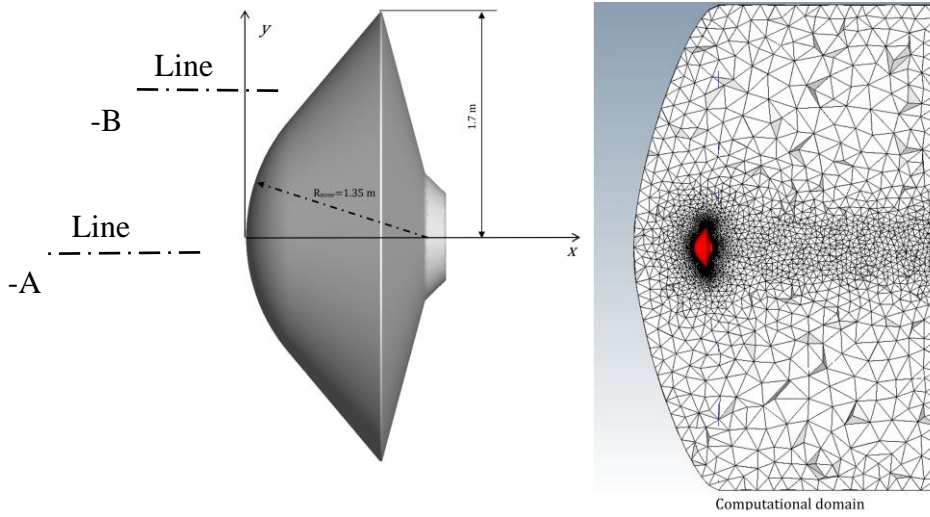


Figure 41. OREX geometry and computational domain.

The surface temperature is set to $T_w = 1519 K$. Air is assumed to be a thermally perfect gas and the free-stream conditions are as follows:

$$T_\infty = 248 K, p_\infty = 23.6 Pa, V_\infty = 5561.6 m s^{-1}, \gamma = 1.4, Kn = 9.29 \times 10^{-5}$$

The electrical conductivity is given as:

$$\sigma = \sigma_0 \left(\frac{T}{T_r} \right)^2$$

where $\sigma_0 = 200 \Omega^{-1} m^{-1}$ and $T_r = 25000 K$ [36]. The Reynolds number based on nose radius is $Re = 156,390$. Turbulence is introduced via the Spalart-Allmaras model with a free-stream of Eddy-to-laminar viscosity ratio of 10^{-5} .

A magnetic dipole is placed along the x -axis at $x = 0.8 m$ with $\hat{\mathbf{m}} = (1, 0, 0)^T$ and $B_0 = 0.3 T$. The Hall parameter is set to $\beta = 10$. The inflow and outflow boundary conditions are the same as in the preceding test case. The surface of the vehicle is assumed to be an electrode, with the electric potential set to $0 V$.

The same optimization strategies of the previous case are adopted. An initial coarse mesh (2,391,100 nodes, 1,539,187 tetrahedral and 4,231,216 prismatic elements) and a target number of nodes (6,000,000) are the same for the three cases listed in Table 4. A target number of nodes much higher than the initial grid is justified by the anticipated formation of a turbulent wake and additional phenomena. The turbulent viscosity coefficient, μ_T , being one of the solution

variables, is incorporated in the adaptation criteria of Cases 1 and 3 to properly capture the wake behind the capsule. Figure 42 shows the convergence of the Mach number distributions along the stagnation line (Line-A in Figure 41) obtained on the original and the optimized meshes for Case 3. As in the previous case, after two adaptation cycles the difference between the distributions becomes negligible.

Optimization	criteria	Final nodes	Final elements
Case 1	ρ, V, p, T, μ_T (Flow only)	5,869,543	26,061,617
Case 2	ϕ (EM only)	6,027,358	26,824,706
Case 3	$\rho, V, p, T,$ μ_T, ϕ (Flow+EM)	5,809,704	25,808,277

Table 4. Turbulent flow over OREX capsule:
mesh adaptation setup.

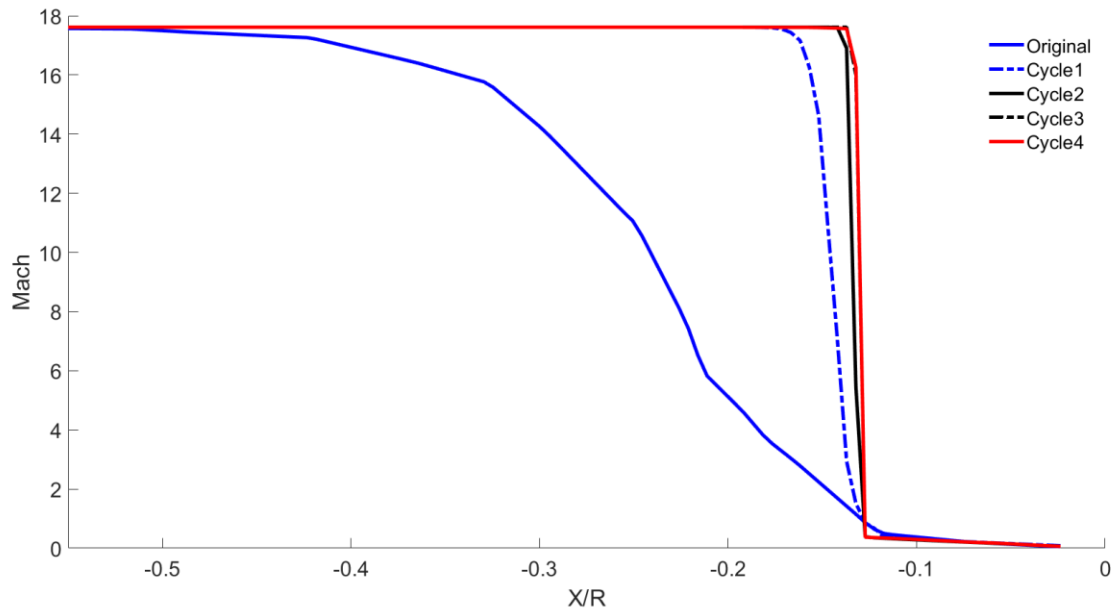
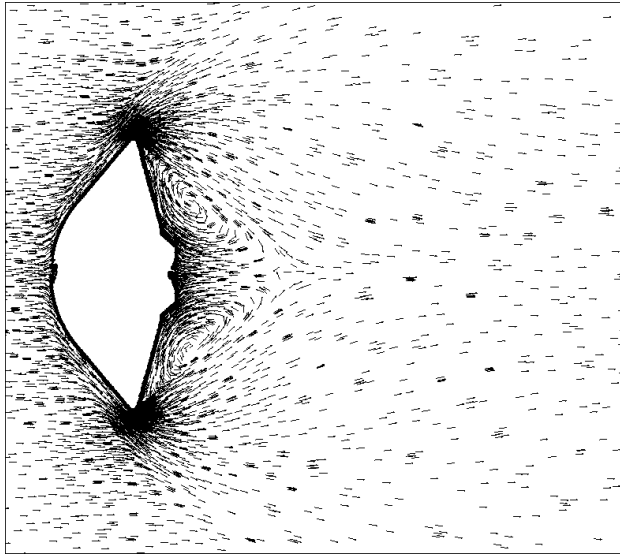
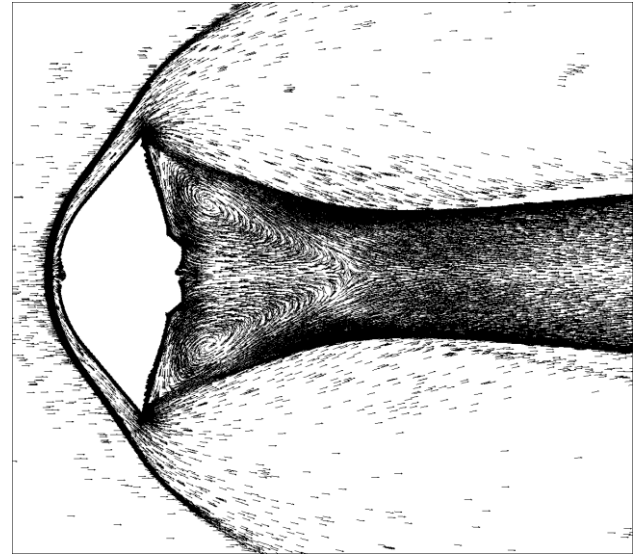


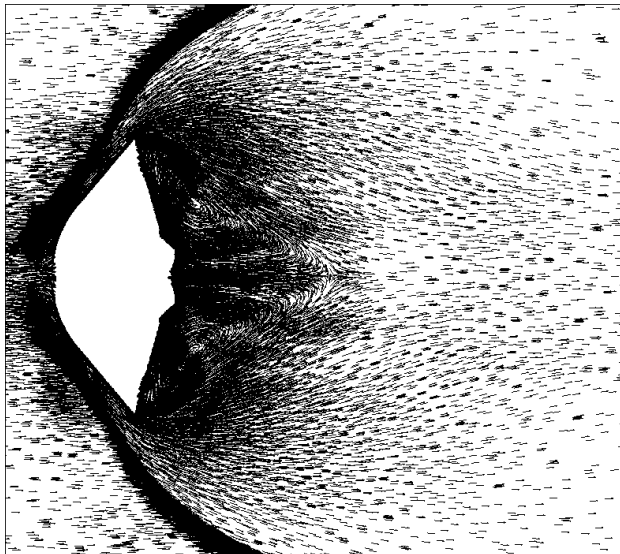
Figure 42. Turbulent flow over OREX capsule:
convergence of Mach number along stagnation line (line-A in Figure 13) during mesh
optimization (Case 3).



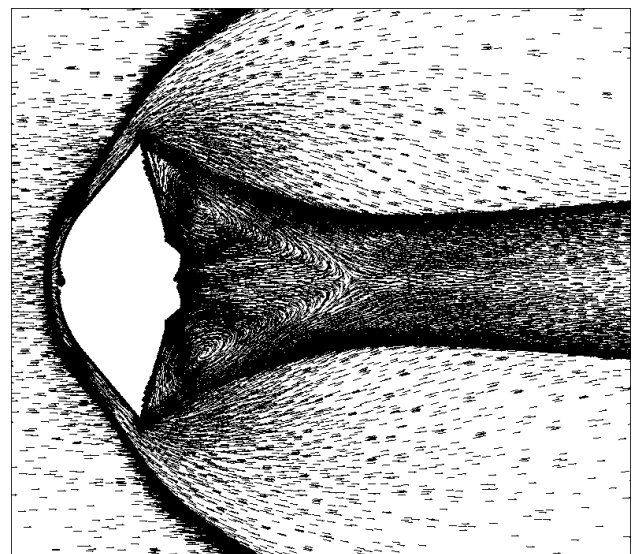
(a)



(b)



(c)



(d)

Figure 43. Turbulent flow over OREX capsule, velocity vectors from original and optimized meshes:

(a) Original mesh; (b) Case 1 (flow only); (c) Case 2 (EM only); (d) Case 3 (flow+EM).

Figure 43 depicts the velocity vector field obtained with the original and adapted meshes. The major flowfield characteristics, such as the bow shock in the forebody region, the expansion fans on the shoulder, the base recirculation region, the converging free shear layer and the weak recompression shock wave emanating from the neck of the wake, are crisply defined when the flow variables are included in the adaptation criteria (Figures 43 (b) and (d)). On the other hand, insufficiently resolved (if not almost totally missing) flow characteristics are observed in Figures 43 (a) and (c). For example, compared to Figures 43 (b) and (d), the base recirculation region is substantially smaller in Figure 43 (a) and poorly resolved away from the base in Figure 43 (c).

Figure 44 shows the original and optimized meshes. Figures 45 and 46 display the contours of the electric potential and Mach number obtained with both meshes. Due to the complexity of the geometry and the formation of the wake, the adapted meshes exhibit different patterns according to the optimization criteria. In this test case, the electrical conductivity is a function of the square of the temperature and therefore increases abruptly across the strong shock. The resulting electric potential contours show sharp gradients in the vicinity of the shock in the forebody region (Figure 45). In addition, since the wall is assumed to be conducting and electric currents are short-circuited on the surface, strong variations are also observed in Figure 45 in the base region near the surface. The features of the electric potential appear clearly in the meshes of Case 2 and 3, shown in Figures 44 (c) and (d), since electric potential is one of the optimization criteria. On the other hand, the original coarse mesh in Figure 44 (a) produces an inaccurate electric potential distribution, with smeared gradients across the shock, overestimated values in the base region and behind the shock, and weak gradients behind the shoulder (Figure 45(a)).

As with the previous test case, optimizing solely on flow variables (Case 1) clusters the nodes near the flow features and leaves the other regions with highly stretched elements. Consequently, the resolution of the electric potential improves across the shock compared to the original mesh, but its quality in the base region is unsatisfactory (Figure 45(b)). Optimization on the electric potential only (Case 2) shows a smeared shock in the stagnation region and a smeared wake due to lack of refinement (Figures 46 (c) and 43 (c)) compared to Cases 1 and 3 (Figures 46 (b) and (d)).

Adaptation on both flow and EM variables (Case 3) captures the features of the flow and EM fields much better, most importantly for the same node and element counts. Figure 44 (d) shows that the grid automatically clusters in the shock region, the expansion fan on the shoulder,

the wake, and captures the sharp gradients of electric potential in the forebody and wake regions. Figure 47 exhibits the Mach number and electric potential distributions along high gradients lines. This optimization strategy produces a more accurate solution in the wake region (Figures 45 and 46), while yielding in the forebody region a Mach number distribution almost identical to Case 1 and an electric potential almost identical to Case 2 (Figure 47).

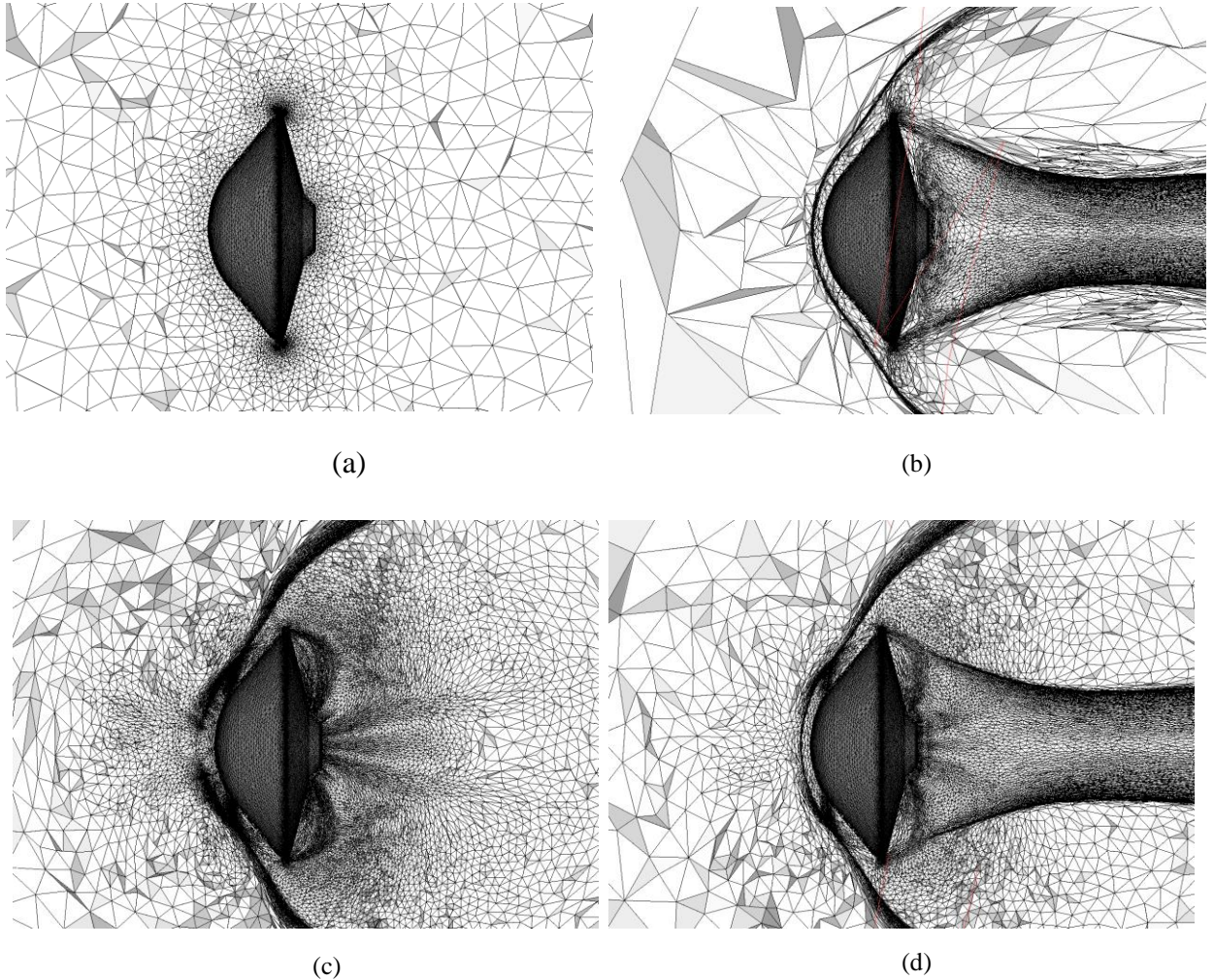


Figure 44. Turbulent flow over OREX capsule, meshes with different optimization strategies:
(a) Original mesh; (b) Case 1 (flow only); (c) Case 2 (EM only); (d) Case 3 (flow+EM).

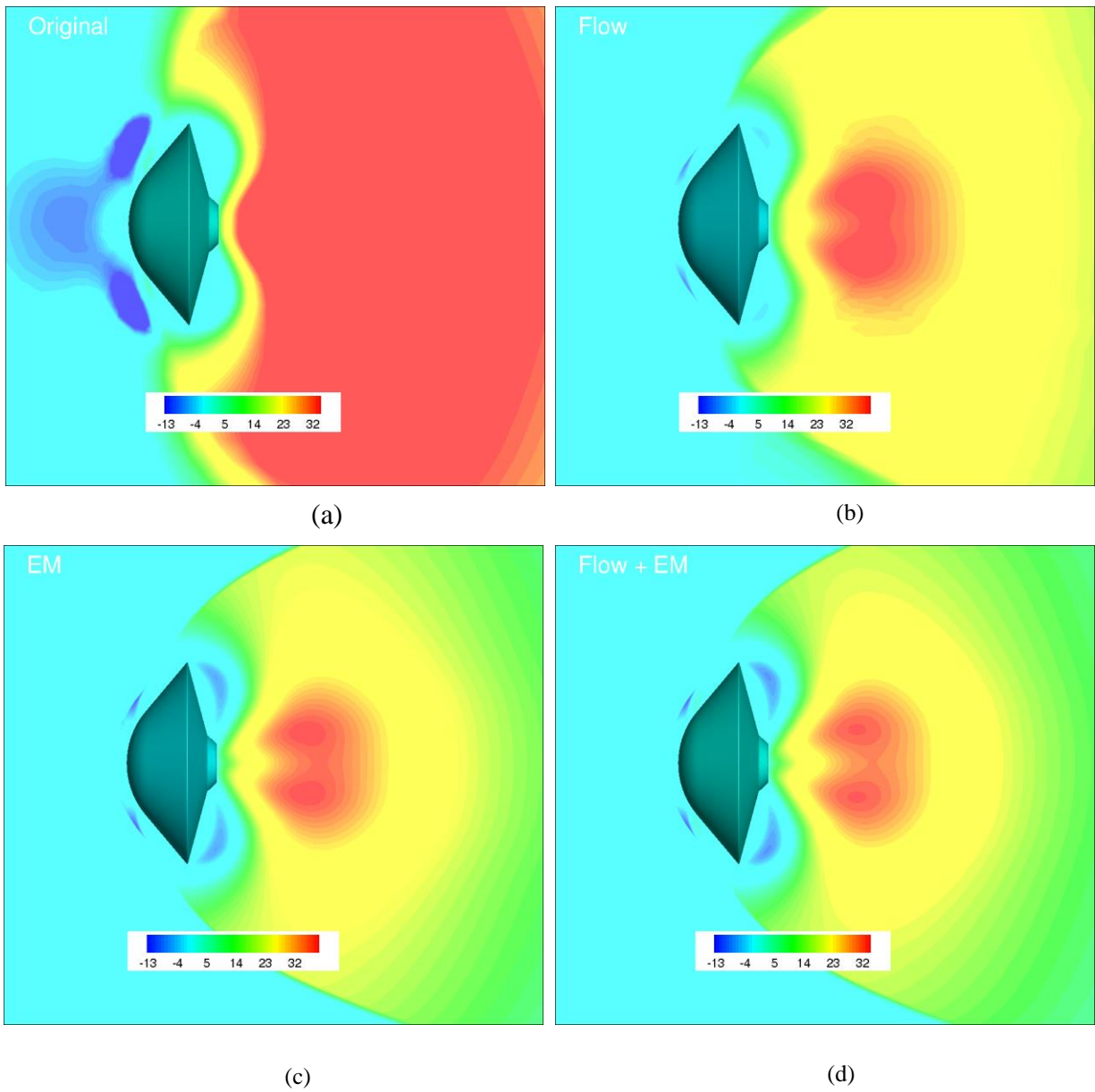


Figure 45. Turbulent flow over OREX capsule, electric potential (V) contours from original and optimized meshes:
(a) Original mesh; (b) Case 1 (flow only); (c) Case 2 (EM only); (d) Case 3 (flow+EM).

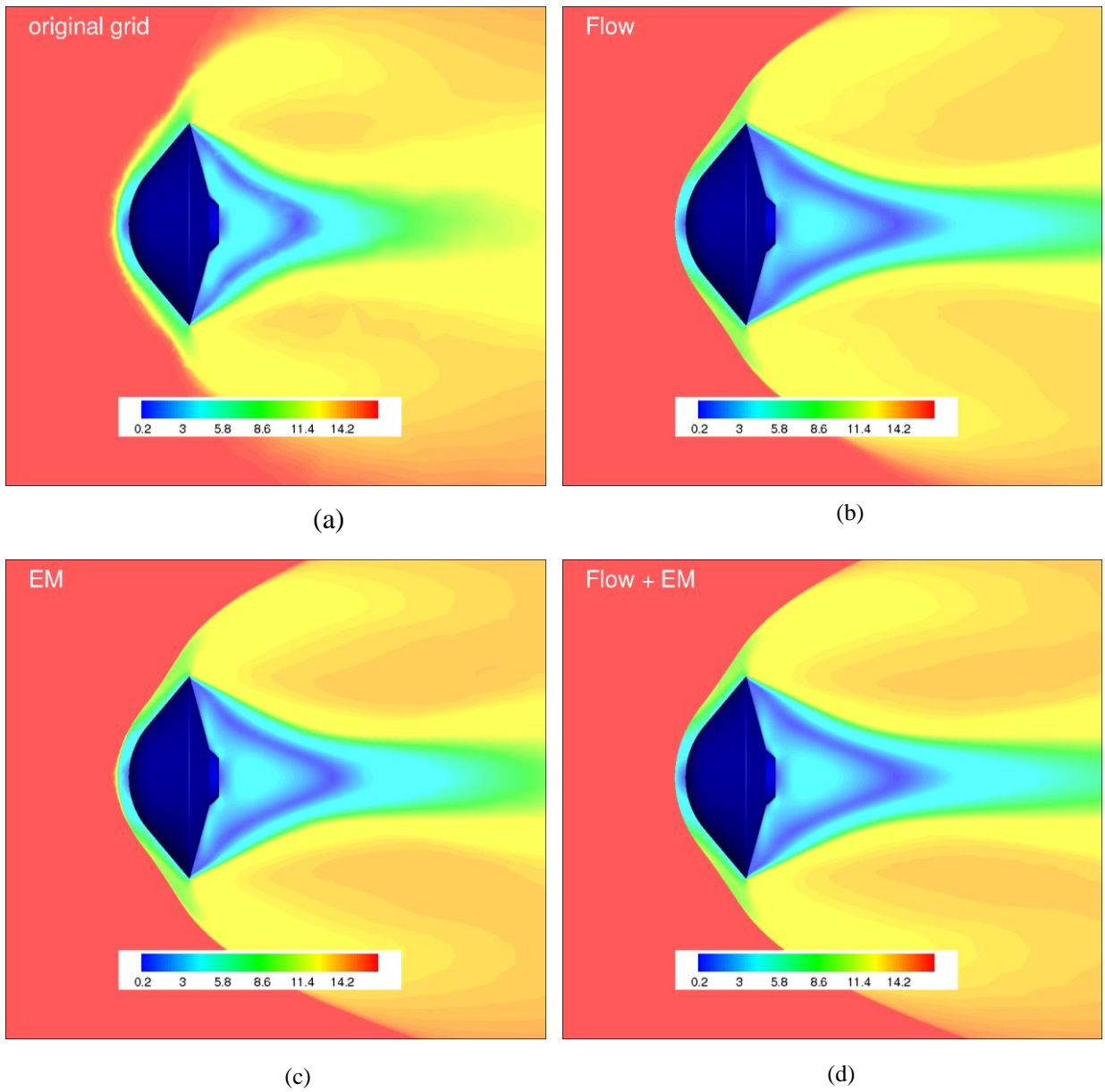


Figure 46. Turbulent flow over OREX capsule, Mach number contours from original and optimized meshes:
(a) Original mesh; (b) Case 1(flow only); (c) Case 2 (EM only); (d) Case 3 (flow+EM).

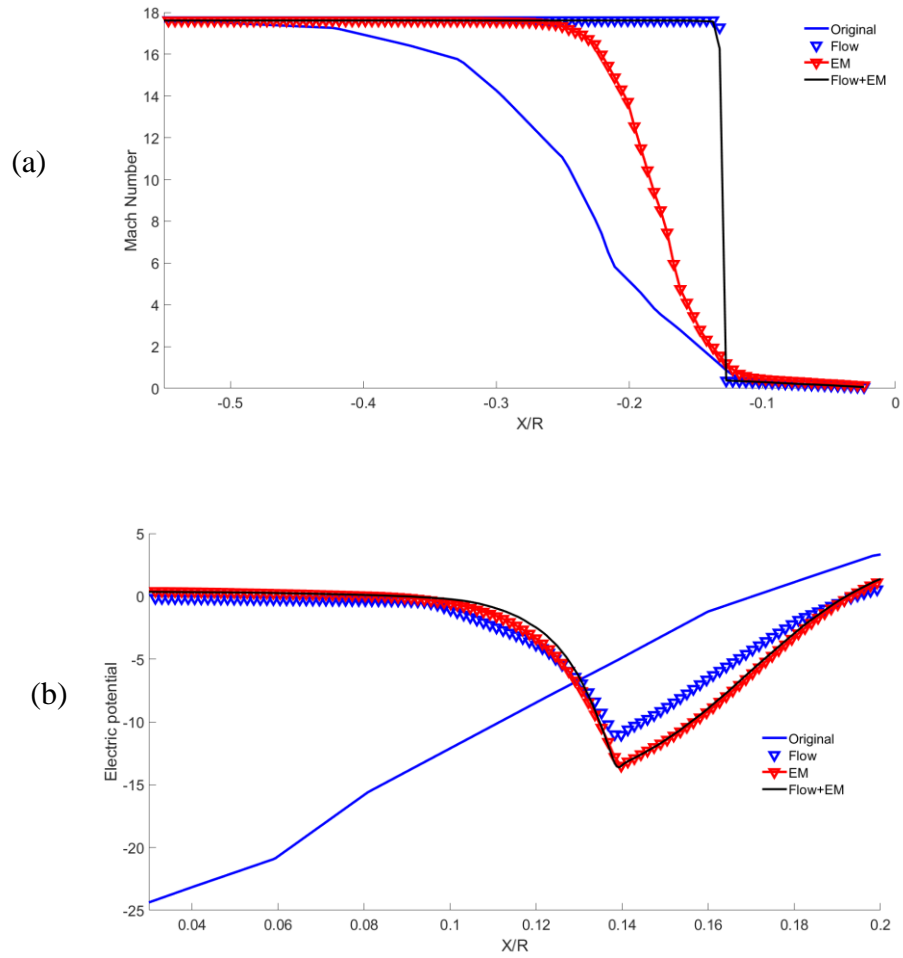


Figure 47. Turbulent flow over OREX capsule:
(a) Mach number distribution along stagnation line (line-A in Figure 40); (b) Electric potential distribution along $y=1.1$ m, $z=0$ m (line-B in Figure 40).

5 Resistive MHD Model

In this chapter, the results from selected simulations of MHD flows employing the resistive MHD model are presented. The RANS solver is the same as in the preceding chapter with a modification to the EM source terms to incorporate the induced magnetic field.

Four test cases are presented to validate the resistive MHD model: the Hartmann flow, a converging MGD accelerator, a two-dimensional simplified scramjet assuming inviscid flow, and a three-dimensional scramjet with viscous flow. To verify the fulfillment of the divergence-free constraint of the magnetic field, the L_2 -norm of the divergence over the computational domain is reported for each test case, approximated using the following formula

$$\|\nabla \cdot \mathbf{B}\|_2 = \sqrt{\sum_e \int_{V_e} (\nabla \cdot \mathbf{B})^2 dV_e} = \sqrt{\sum_e \int_{V_e} \left(\sum_{i \in K_e} \nabla W_i \cdot \mathbf{B}_i \right)^2 dV_e} \quad (5.1)$$

The first two test cases use structured grids. The latter two are on unstructured grids and OptiGrid is used to adapt on the flow field quantities (density, temperature and velocity) and the EM quantity of interest (the induced magnetic field in this chapter)

5.1 Hartmann Flow

The Hartmann flow is one of the cornerstone examples in magnetohydrodynamics [85]. It consists of a conducting liquid or gas flowing under the influence of a pressure gradient in the x direction, through a two-dimensional duct with a height of $2h$ in the y direction. A uniform external magnetic field B_0 is applied in the y direction (Figure 48).

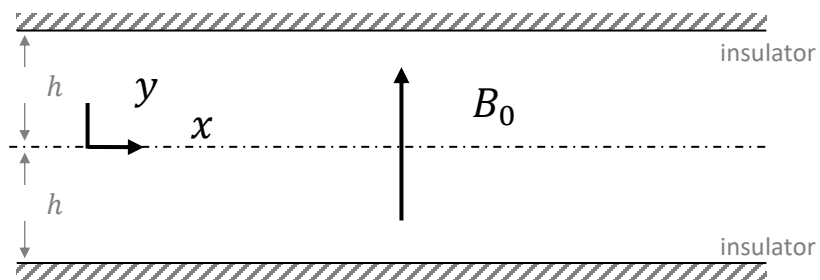


Figure 48. Sketch of the Hartmann flow configuration.

Assuming the walls to be perfectly insulated, an analytical solution for the x component of the velocity and the induced magnetic field exists in the fully-developed regime and is written in non-dimensional form as

$$U^* = \frac{u}{u_M} = \frac{\cosh(\text{Ha}) - \cosh\left(\frac{y \text{Ha}}{h}\right)}{\cosh(\text{Ha}) - 1} \quad (5.2)$$

$$\frac{b_x}{B_0} = -\frac{\text{Re}_m}{\text{Ha}} \left(\frac{\sinh\left(\frac{y \text{Ha}}{h}\right) - \frac{y}{h} \sinh(\text{Ha})}{\cosh(\text{Ha}) - 1} \right) \quad (5.3)$$

where Ha , the Hartmann number is defined as

$$\text{Ha} = B_0 h \left(\frac{\sigma}{\mu} \right)^{\frac{1}{2}} \quad (5.4)$$

where the square of the Hartmann number measures the relative importance of electromagnetic forces to viscous ones.

Results are obtained for a 48 m long rectangular channel ($h = 0.2$ m) with different Hartmann and magnetic Reynolds numbers and compared to the analytical solution. The free-stream temperature is 288 K and the channel walls are assumed to be adiabatic. A uniform flow of $10 \frac{\text{m}}{\text{s}}$ is imposed at the inlet and the outlet pressure is specified to be 1010 Pa. The mesh is composed of 600,000 nodes with 296,901 hexahedral elements with one layer of elements along the periodic direction z . Figures 49 and 50 show a comparison between the numerical and analytical solutions at $x = 45$ m for $\text{Re}_m = 1$ and for different Hartmann numbers $\text{Ha} = 1, 2, 5$ and 10. In Figure 48 the braking effect of the electromagnetic forces in the core region of the flow is observed, together with the evolution of the hydrodynamic Hartmann layers. In Figure 49, the magnetic signature of the Hartmann layers is shown. The L_2 -norms of $\nabla \cdot \mathbf{B}$ are 0.32, 0.31, 0.25 and 0.18 $\text{T} \cdot \text{m}^{1/2}$ for $\text{Ha} = 1, 2, 5$ and 10, respectively ($\text{Re}_m = 1$).

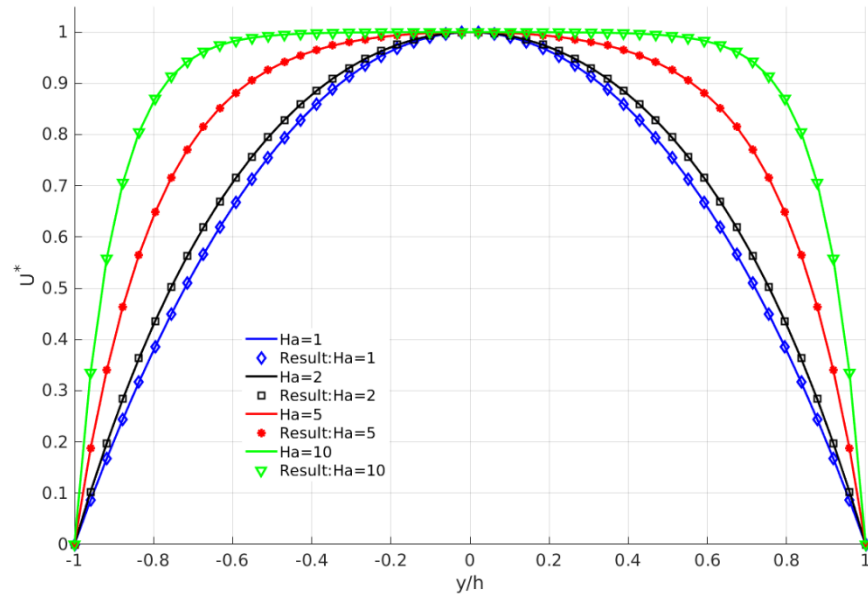


Figure 49. Hartmann flow inside a two-dimensional channel: velocity for different Hartmann numbers and unitary magnetic Reynolds number at $x = 45 m$.

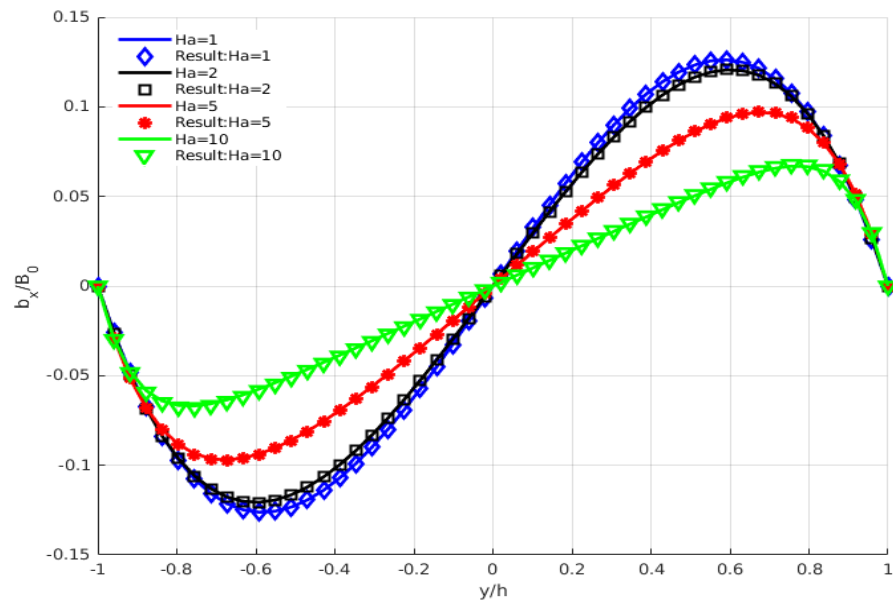


Figure 50. Hartmann flow inside a two-dimensional channel: induced magnetic field for different Hartmann numbers and unitary magnetic Reynolds number at $x = 45 m$.

5.2 MGD Converging Channel Accelerator

Taken from MacCormack [44], this test case considers a 5.566 m long channel. The height of the channel is 0.933 m at the inlet and 0.730 m at the exit, as sketched in Figure 51. The accelerator inlet is at $x = 0$ m and its outlet is at $x = 2.846$ m.

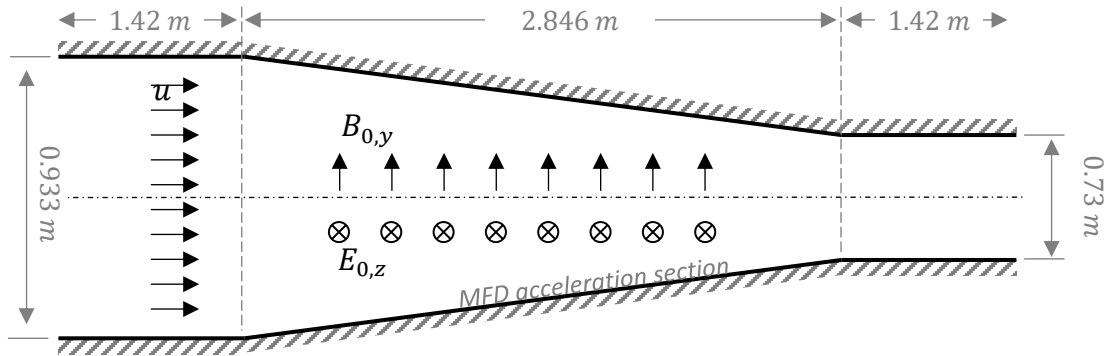


Figure 51. Sketch of the converging channel accelerator.

A constant magnetic field ($B_{0,y} = 11.28$ T) is imposed along the y direction between the inlet and the outlet of the accelerator section. The induced electric field \mathbf{e} is neglected and the total electric field \mathbf{E} could be approximated by the imposed one \mathbf{E}_0 which is applied everywhere across the accelerator section and varies linearly from $E_{0,z} = -30,990$ V.m $^{-1}$ at inlet to $E_{0,z} = -31,470$ V/m at exit). The boundary conditions for the induced magnetic field at solid walls normal to the y axis are

$$\frac{\partial b_x}{\partial y} = -\mu_0 \sigma E_{0,z}, \quad b_y = 0, \quad \frac{\partial b_z}{\partial y} = 0$$

where $\mu_0 = 1.257 \times 10^{-6}$ H/m. At the entrance of the channel, the pressure, the temperature, the Mach number and the Knudsen number are respectively: $p = 1.251 \times 10^6$ Pa, $T = 3583$ K, $Mach = 1.147$, $Kn = 8.60 \times 10^{-8}$.

Based on these conditions and the accelerator length, the magnetic Reynolds number is $Re_m = 0.17$. The mesh is composed of 64,962 nodes with 32,000 hexahedral elements. Numerical results have been obtained for the conditions described above. The induced magnetic field components are shown in Figures 52 and 53. Since the magnetic Reynolds number is considerably small thanks to the weak ionization in this test case, the induced magnetic field is not salient in general compared to the imposed one and is most noticeable at the inlet and outlet

of the accelerator section where the discontinuity of the imposed electric and magnetic fields occurs. The L_2 -norm of $\nabla \cdot \mathbf{B}$ is $0.06 \text{ T} \cdot \text{m}^{1/2}$.

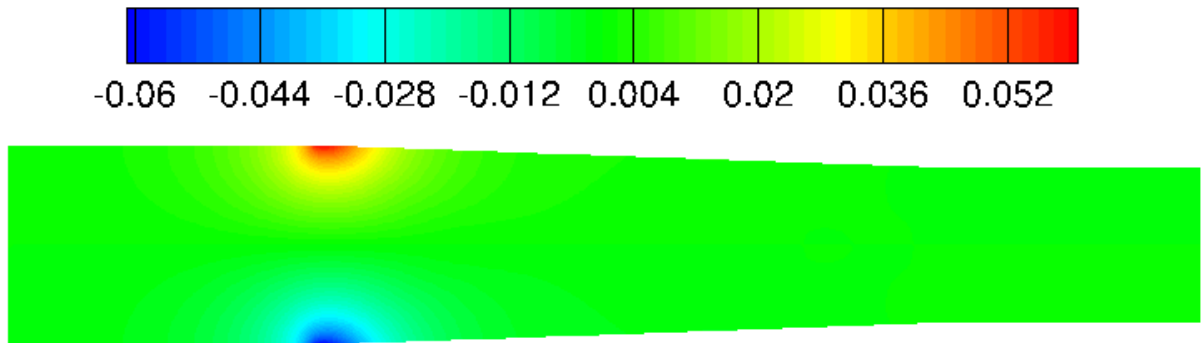


Figure 52. MGD converging channel accelerator:
 x -component of the induced magnetic field (T) b_x .

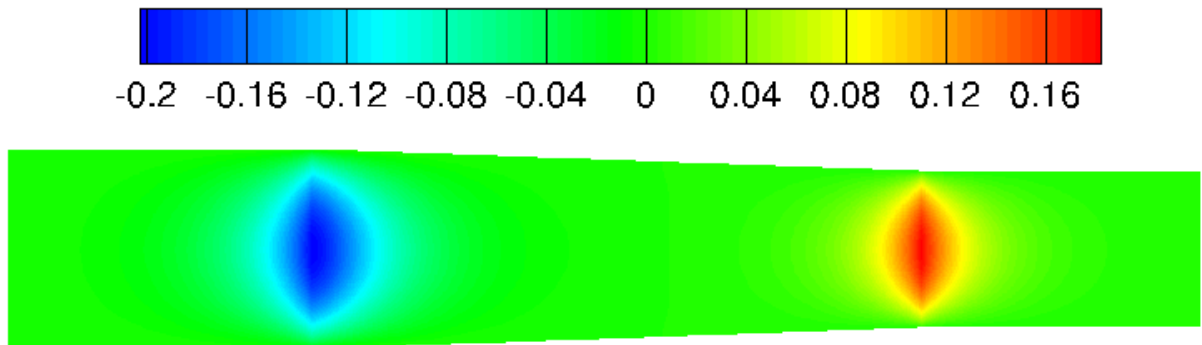


Figure 53. MGD converging channel accelerator:
 y -component of the induced magnetic field (T) b_y .

The pressure and the Mach number contours are shown in Figures 54 and 55. A supersonic flow is supposed to slow down in a convergent channel. However, under the influence of the Lorentz force, it is seen that a significant acceleration occurs between the entrance of the channel and the outlet of the accelerator by a factor of 1.96. From these results, it is observed that two mirrored shock waves generated at the inlet of the accelerator are reflected by the internal walls at multiple locations in the chamber.

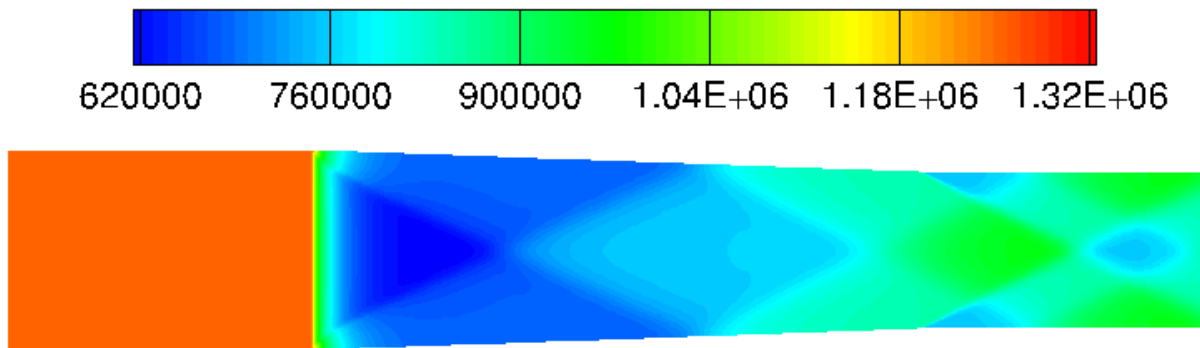


Figure 54. MGD converging channel accelerator:
pressure (in Pa) contours.

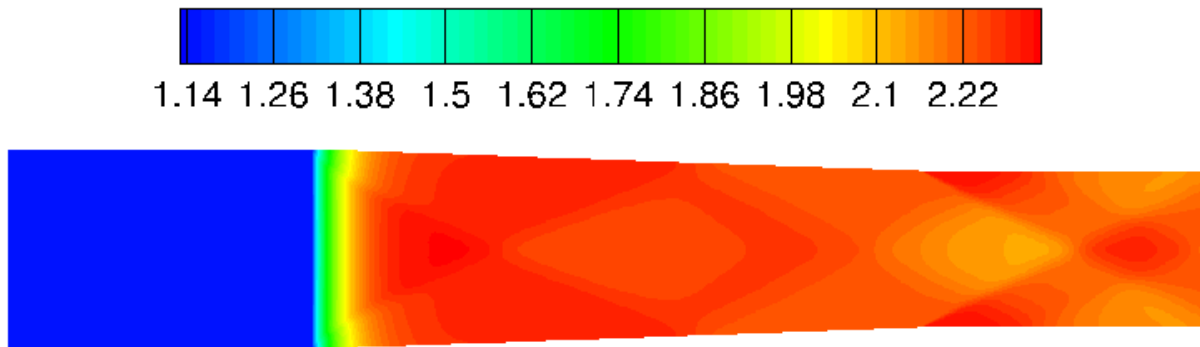


Figure 55. MGD converging channel accelerator:
Mach number contours.

The axial velocity profile along the channel centerline $y = 0$ m (normalized by the axial velocity at the entrance $u_0 = 1400.35 \text{ m}\cdot\text{s}^{-1}$) is shown in Figure 56 and compared with MacCormack [44]. While both results qualitatively agree with each other and predict the same acceleration ratio, an exception is observed at the outlet of the accelerator section which shows one mesh point oscillation.

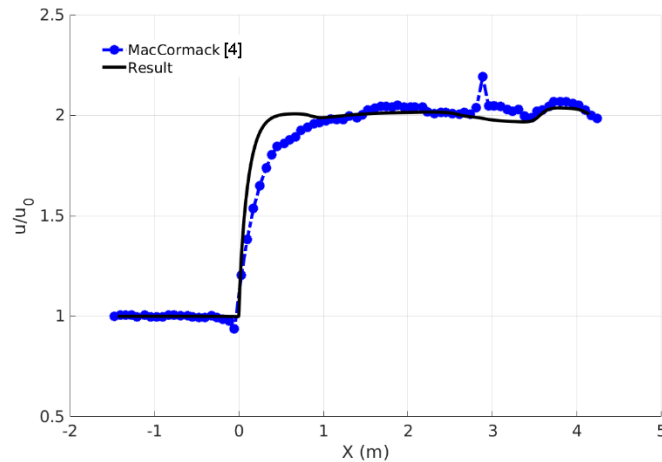


Figure 56. MGD converging channel accelerator:
 x component of the velocity u/u_0 along the centerline $y = 0$.

5.3 2D MHD Energy Bypass Scramjet Engine (Inviscid)

In an MHD energy bypass scramjet engine, the converging channel accelerator is located just downstream of the combustor chamber which itself is downstream of the diverging channel functioning as the generator. In this test case, taken from [45], the flow is assumed to be inviscid and a simplified geometry is considered. The geometry is composed of an inlet section, a generator, a combustor, an accelerator and an exit section. In its diverging generator section, the engine generates electric power from the kinetic energy and the flow slows down for better combustion. The extracted power is then used in the converging accelerator section to increase the thrust. Figure 57 shows a sketch of the engine. The scramjet is 6.9912 m long in total and the lengths of the generator and accelerator are 2.72 m and 2.85 m, respectively. At the entrance of the channel, the pressure, the temperature, the Mach number and the Knudsen number are respectively: $p = 1.039 \times 10^6$ Pa, $T = 3370$ K, $Mach = 2.16$, $Kn = 9.72 \times 10^{-8}$.

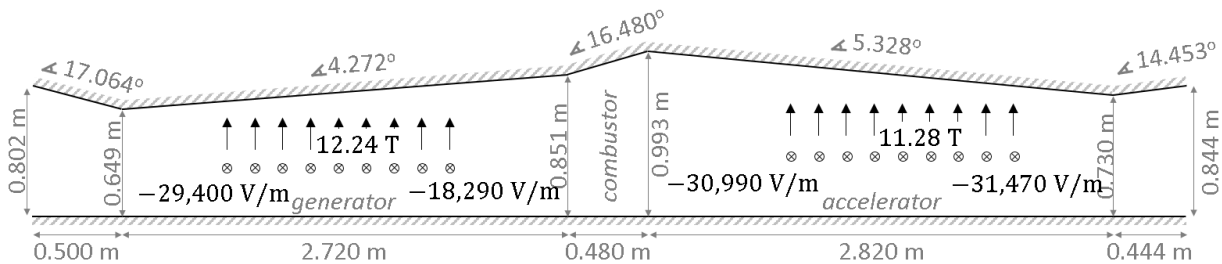


Figure 57. Sketch of the simplified MHD energy bypass scramjet engine with the applied electromagnetic fields.

A piecewise constant magnetic field is imposed in the y direction and Figure 58 (top) shows its distribution along the scramjet, with $B_{0y} = 12.74$ T and 11.28 T at the generator and accelerator, respectively.

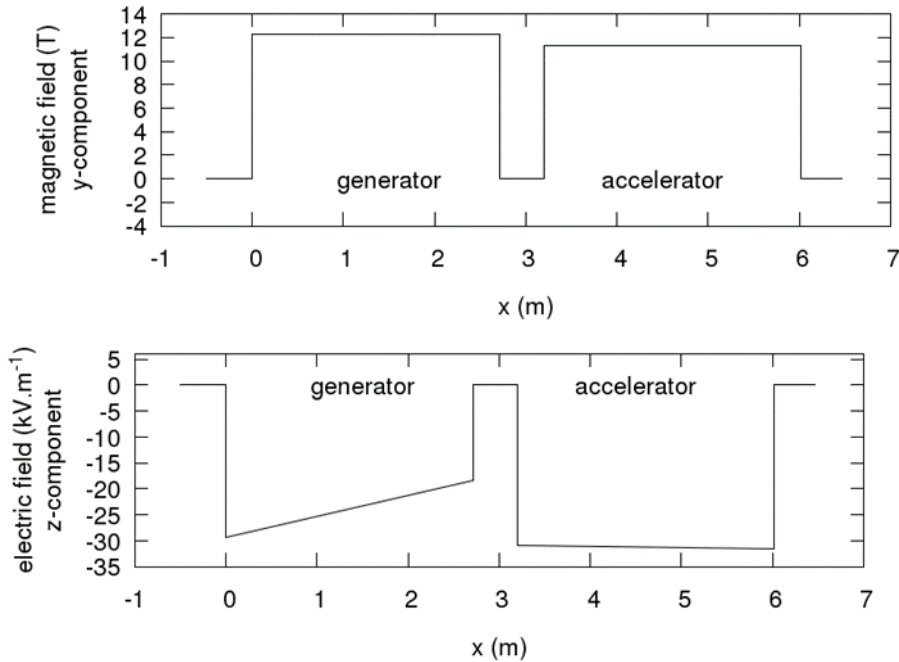


Figure 58. 2D MHD energy bypass scramjet engine: the distribution of the imposed magnetic field (top) and the imposed electric field (bottom) along the x axis.

The imposed electric field is everywhere across the generator and the accelerator sections. For the generator section, it varies linearly from $E_{0z} = -29,400 \text{ V.m}^{-1}$ at the inlet to $E_{0z} = -18,290 \text{ V.m}^{-1}$ at the outlet. For the accelerator, it varies linearly from $E_{0z} = -30,990 \text{ V.m}^{-1}$ to $E_{0z} = -31,470 \text{ V.m}^{-1}$ (Figure 58, bottom). Boundary conditions and entrance parameters are

the same as in the previous test case. The magnetic Reynolds number is $Re_m = 0.34$. No combustion takes place within the combustor for this test case. The electric conductivity (σ) equals $32.42 \Omega^{-1}\text{m}^{-1}$ in the generator and $35.87 \Omega^{-1}\text{m}^{-1}$ in the accelerator.

To best resolve the flow features of the complex shock wave structure, OptiGrid was used to seek numerical solutions on unstructured meshes. The adaptation criteria are the density ρ , the temperature T , the two components of velocity u and v and the magnitude of the induced magnetic field \mathbf{b} . Three mesh-optimization cases starting from the same unstructured initial mesh (8398 nodes, 8005 linear prisms), but with different targeted node numbers, are performed (Table 5). Figure 59 shows the initial and adapted (after 5 cycles) meshes of Case 2. In the adapted mesh, two distinct types of node clusters are observed. The first type is aligned with flow features (shocks, expansion waves, *etc.*), and the second type resides at the junctions of engine chambers, caused by the discontinuities of the imposed electric and magnetic fields, as well as the abrupt geometry changes.

Case	Target no. of nodes	Final no. of nodes	Final no. of elements
Case 1	8398	8370	8124
Case 2	16000	15974	15611
Case 3	32000	32480	31907

Table 5. 2D MHD energy bypass scramjet engine: the mesh-optimization cases.

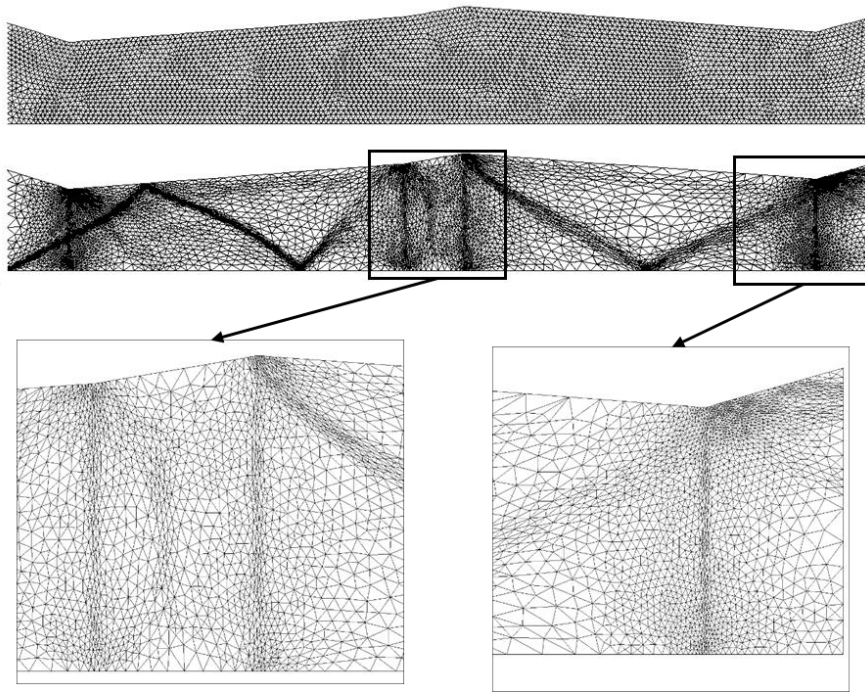


Figure 59. 2D MHD energy bypass scramjet engine: initial mesh and adapted one (Optimization Case 2) after 5 adaptation cycles.

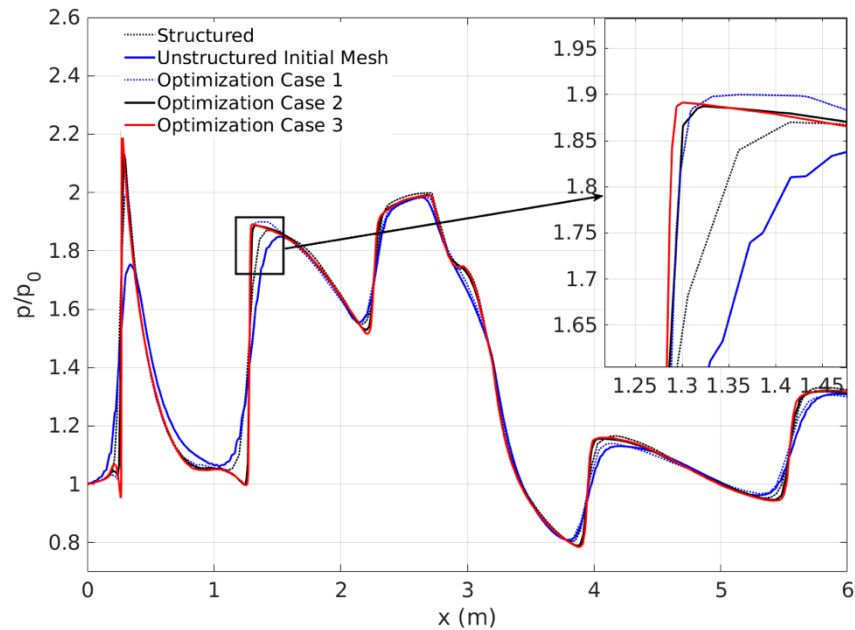


Figure 60. 2D MHD energy bypass scramjet engine: the pressure profile along the horizontal axis $y = 0.4$ m.

In Figure 60, the pressure profiles along the horizontal axis $y = 0.4$ m are shown for five different meshes: a structured mesh (57760 nodes, 28440 hexahedral elements), an unstructured initial mesh and three optimized meshes. One can notice that with almost the same number of nodes and elements as the unstructured initial mesh (Optimization Case 1), the solution quality in terms of shock sharpness is substantially improved and is superior to that achieved by the structured mesh with almost 6 times as many nodes. The mesh optimization methodology takes into account the directionality of the solution and therefore outperforms an unguided mesh-refinement scheme in which additional nodes are added in all directions. Table 6 lists the channel thrust at the exit of the engine normalized by $\int p + \rho V^2 dA_0$ at the inlet. It can be concluded that grid convergence is attained when the node count is doubled (Optimization Case 2) since the maximum difference between Optimization Case 2 and Optimization Case 3 is less than 0.05%.

Mesh	Normalized Exit Thrust
Structured	1.0788
Unstructured Initial	1.0687
Optimization Case 1	1.0725
Optimization Case 2	1.0734
Optimization Case 3	1.0731

Table 6. 2D MHD energy bypass scramjet engine: normalized thrust at the exit for different meshes.

Figure 61 shows the Mach number contours using the unstructured initial mesh (above) and the adapted one (Optimization Case 2, below). The shock resolution is significantly improved because the adapted mesh is considerably better aligned with the shocks by adding nodes in regions of high truncation error.

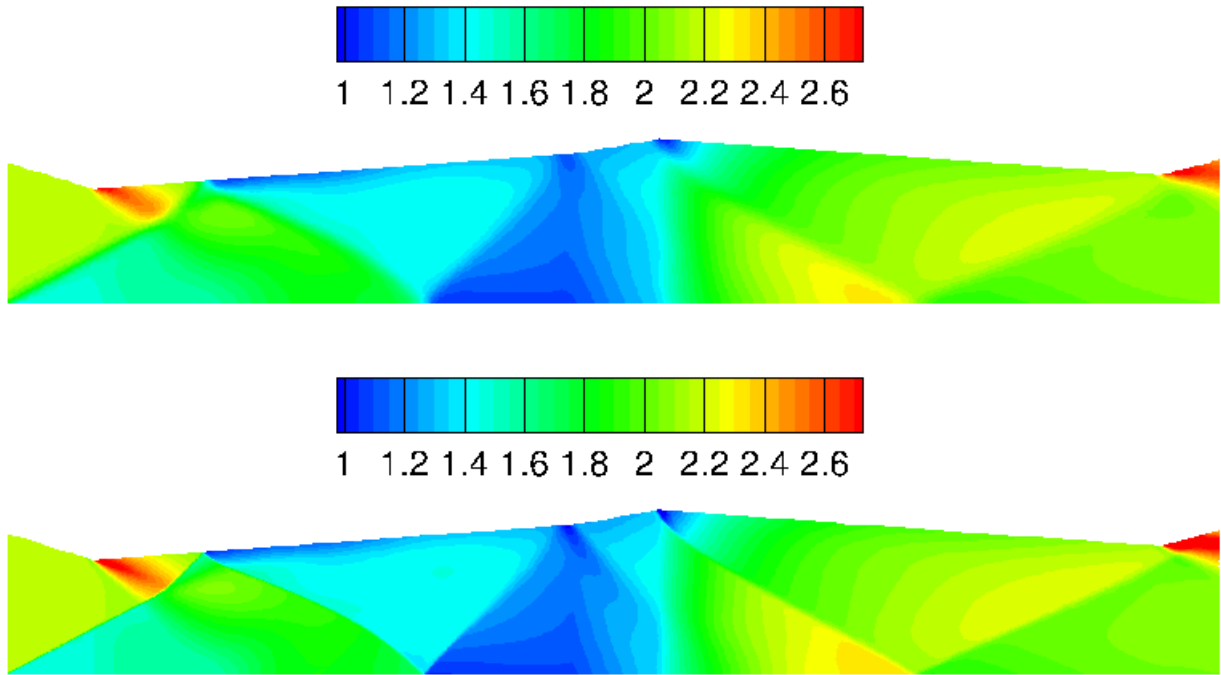


Figure 61. 2D MHD energy bypass scramjet engine:
Mach number contours with the initial (top) and adapted (bottom) meshes.

Figure 62 shows the pressure contours obtained with the adapted mesh (Optimization Case 2). In the inlet section, the supersonic stream forms an oblique shock (bottom) and an expansion wave (top), which subsequently experience a process of crossing and reflection through the chamber and establish a complex wave system.

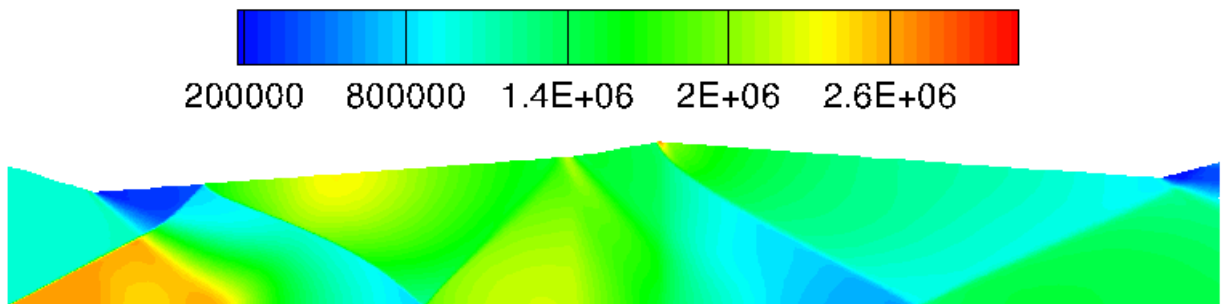


Figure 62. 2D MHD energy bypass scramjet engine:
pressure (Pa) contours with the adapted mesh.

In Figures 63 and 64, results for the induced magnetic field obtained with the adapted mesh are shown. The x -component of the induced magnetic field (b_x) is most salient in the vicinity of the walls close to the inlet of the accelerator section due to the discontinuity of the boundary condition directly related to the imposed electric field. The y -component (b_y), on the other hand, is noticeable only in the junctions of different sections due to the abrupt change of the imposed magnetic field. The L_2 -norm of $\nabla \cdot \mathbf{B}$ is $0.02 \text{ T} \cdot \text{m}^{1/2}$.

By means of mesh optimization, which automatically aligns tetrahedral elements with the shock, one can capture clean and sharp shocks with a substantially reduced number of nodes. Despite the success in resolving the electromagnetic field, however, the results presented by MacCormack [45] suffered from the coarseness of the mesh and could not capture any shock structure in the flow. This is understandable given that the main objective of that work was the development of a scaling scheme for the Maxwell flux to eliminate the numerical instability caused by the disparity in time scales of the flow and EM fields and that the latter was to a large extent insensitive to changes in the flow field. However, a detailed comparison with [45] is also rendered less informative by the crudity of the shock capturing in [45] and is therefore omitted.

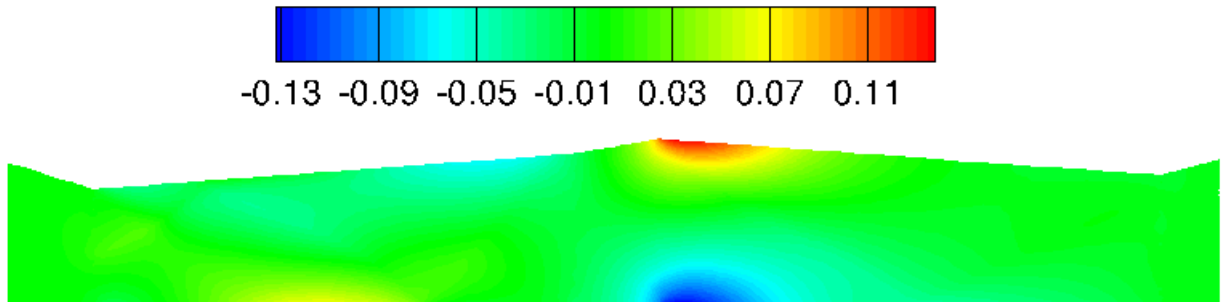


Figure 63. 2D MHD energy bypass scramjet engine:
 x -component of the induced magnetic field (T) b_x .

Figure 65 shows the estimated error derived from second order derivatives of the aforementioned flow and EM quantities, on the unstructured initial mesh (above) and the adapted one (Optimization Case 2, below). The error traces shocks and expansions in the flow field, as well as discontinuities in the EM field (b_x near the junctions of chambers). Adaptation reduces the overall level of the error and uniformly distributes the error across the computational domain.

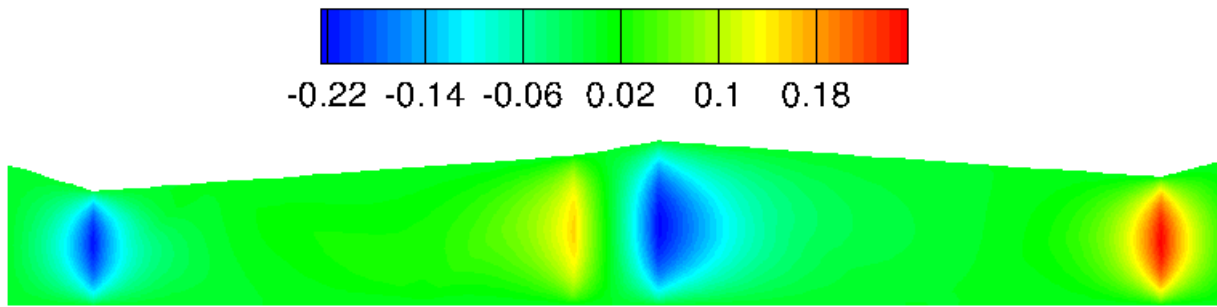


Figure 64. 2D MHD energy bypass scramjet engine:
y-component of the induced magnetic field (T) b_y .

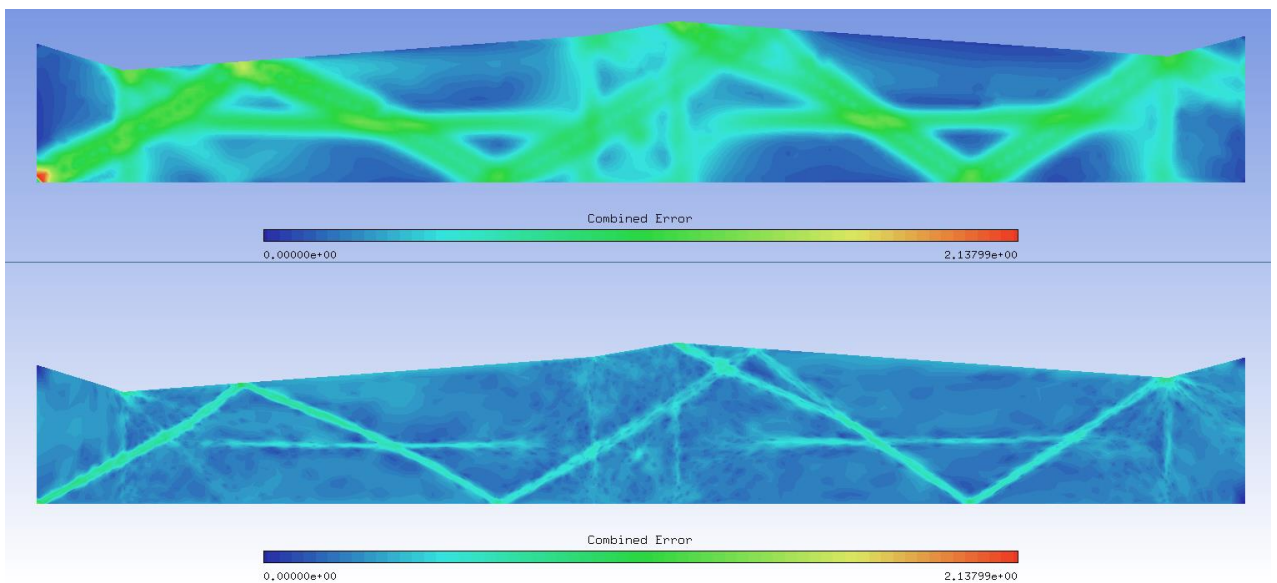


Figure 65. 2D MHD energy bypass scramjet engine:
estimated error contours with the initial (top) and adapted (bottom) meshes.

5.4 3D MHD Energy Bypass Scramjet Engine (Viscous)

The geometry of the 3D MHD energy bypass scramjet engine is obtained by extruding its 2D counterpart along the z -axis by 1 m. The configurations of the imposed magnetic/electric field, the boundary conditions of the magnetic induction equation, the electric conductivity and entrance parameters are inherited from the preceding test case. No-slip boundary conditions are used for solid walls when solving the momentum equations. The Reynolds number based on the generator length is 89,700,000 and the Spalart-Allmaras turbulence model is employed with a free-stream eddy/laminar viscosity ratio of 10^{-5} .

For a better alignment of the mesh with the resolved flow and magnetic fields, anisotropic mesh adaptation is again utilized while preserving the number of nodes and total height of the prism layers near the surface. The adaptation criteria are the same with the preceding subsection. The initial mesh consists of 4,266,260 nodes with 3,285,244 tetrahedral elements and 7,217,694 prisms, and the adapted mesh (after 3 adaptation cycles) has 4,197,014 nodes with 6,129,306 tetrahedral elements and 6,150,474 prisms. Figure 66 shows the initial and adapted meshes.

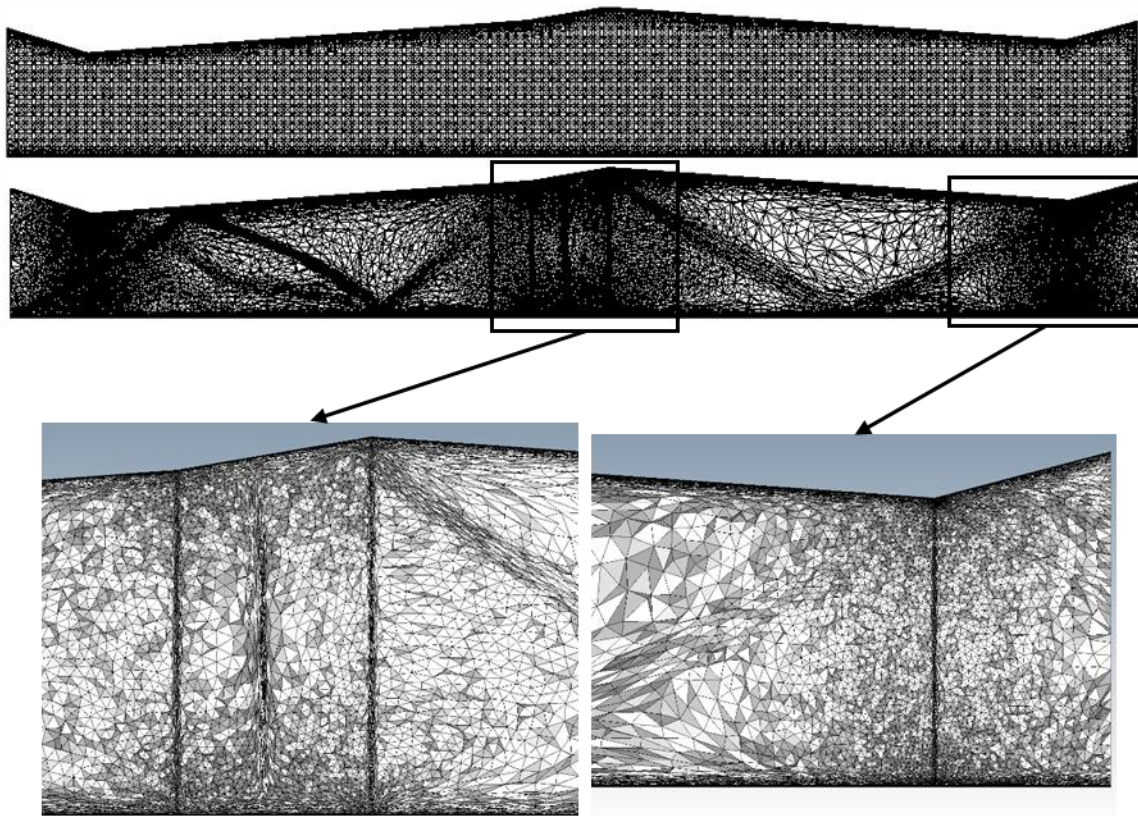


Figure 66. 3D MHD energy bypass scramjet engine: initial mesh and adapted one after 3 adaptation cycles.

Compared to the adapted mesh in the 2D inviscid case (Figure 59), node clusters are observed not only alongside the shock and the induced magnetic field, but also near the no-slip walls where the prisms reside to resolve the boundary layer effect.

Figure 67 shows the Mach number contours (cross section $z = 0$ m) using the initial mesh (top) and the adapted one (bottom). The efficiency and pertinence of the multi-physics

anisotropic mesh adaptation are again clearly put into evidence in these two figures where shocks are significantly better resolved with the adapted mesh.

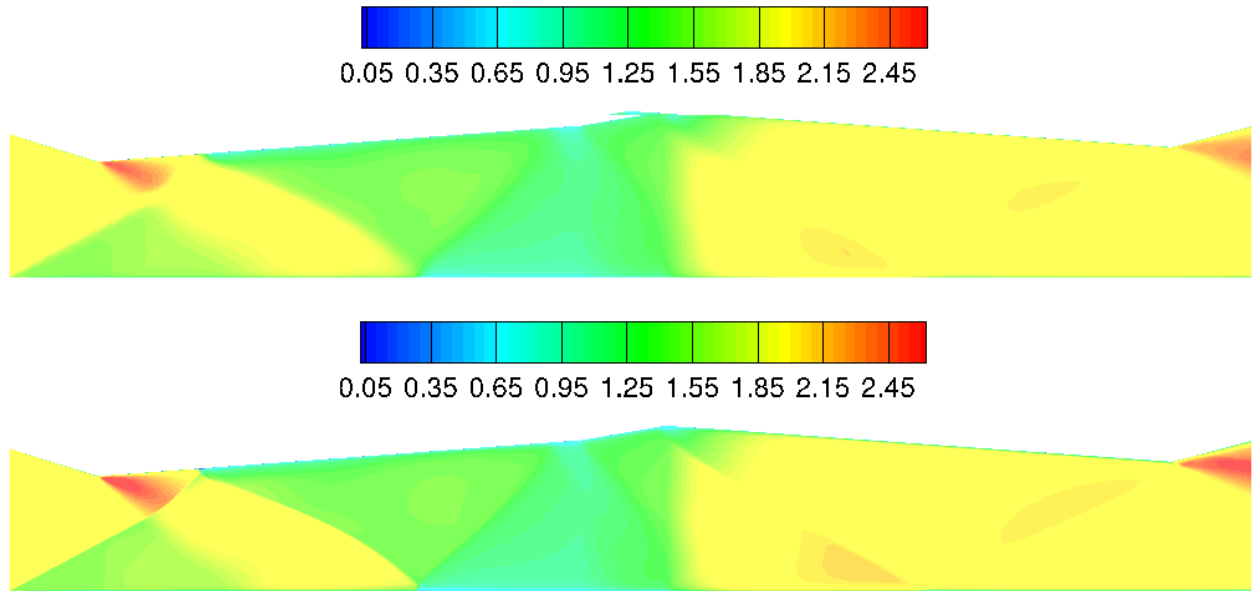


Figure 67. 3D MHD energy bypass scramjet engine:
Mach number contours in the cross section $z = 0 \text{ m}$ for the scramjet with the initial mesh (top) and adapted mesh (bottom).

In Figure 68, the pressure profiles along the horizontal axis $y = 0.40 \text{ m}$ are shown for the 2D inviscid test case (black line), the 3D viscous test case with original (dashed line) and adapted (red line) 3D meshes. While the 3D adapted mesh yields overwhelmingly sharper and cleaner shocks than the initial mesh, it also outperforms the 2D adapted mesh in terms of shock resolution. This is because in the 3D case, more nodes are available to be deployed to accommodate the need of shock capturing. Figure 69 compares the pressure contours at the $z = 0 \text{ m}$ cross-section between the 2D and 3D adapted meshes. The flow structures are similar except that the 3D mesh gives higher pressure, and the boundary layer effect is insignificant for that case.

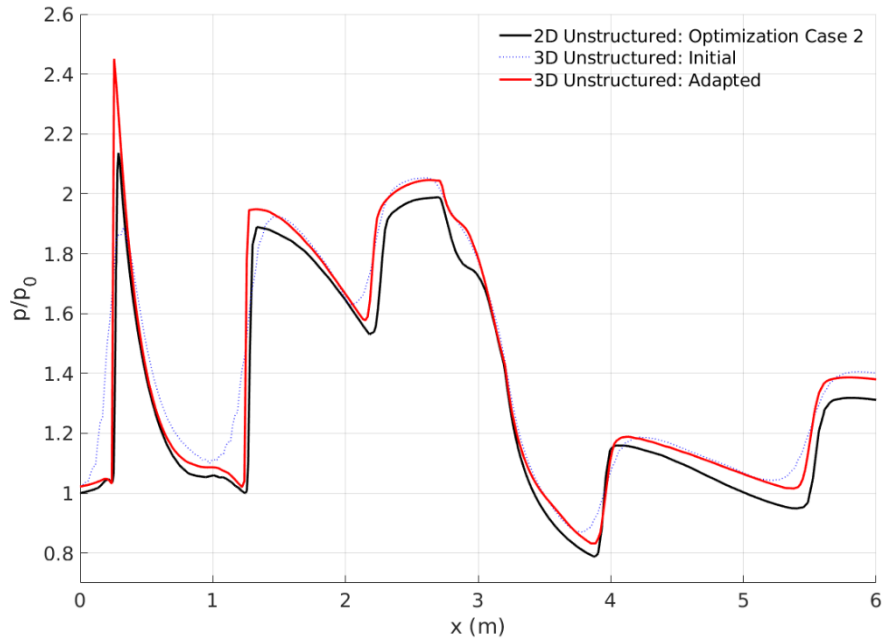


Figure 68. 3D MHD energy bypass scramjet engine: pressure profile along the horizontal axis $y = 0.40$ m.

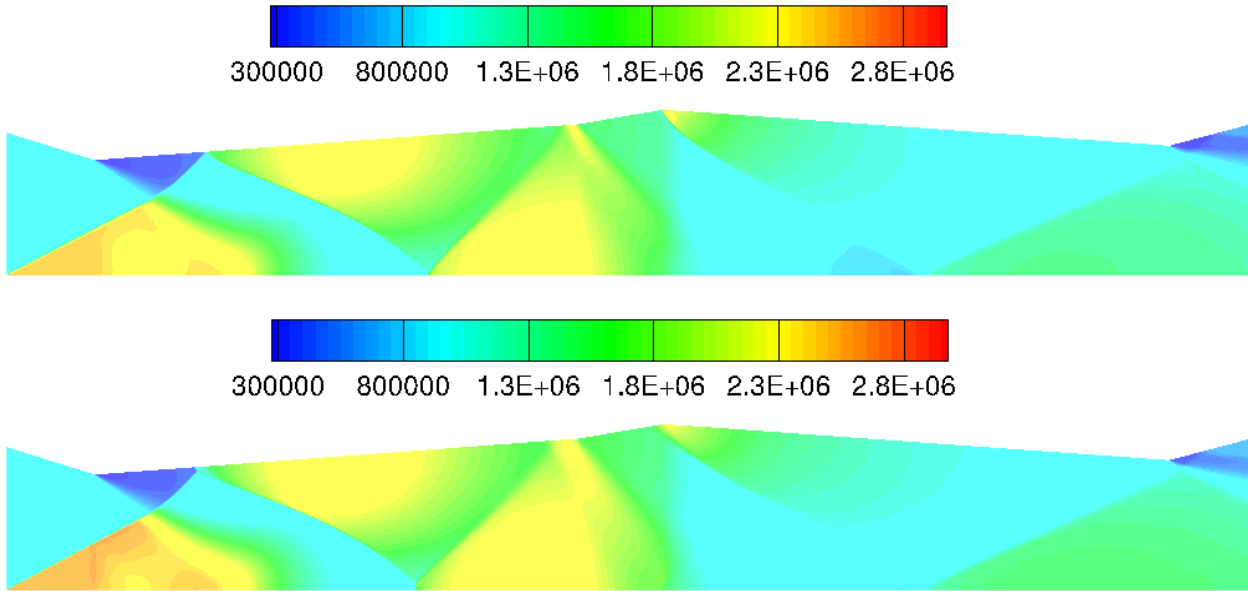


Figure 69. 3D MHD energy bypass scramjet engine: pressure contours in the cross section $z = 0$ m; top: 2D with adapted mesh (Optimization Case 2), bottom: 3D with adapted mesh.

In Figures 70 and 71, results for the induced magnetic field obtained with the adapted mesh are shown. The induced magnetic field is more dispersive compared to its 2D inviscid

counterpart (Figures 63 and 64) due to the existence of a boundary layer. The L_2 -norm of $\nabla \cdot \mathbf{B}$ is $0.06 \text{ T} \cdot \text{m}^{1/2}$.

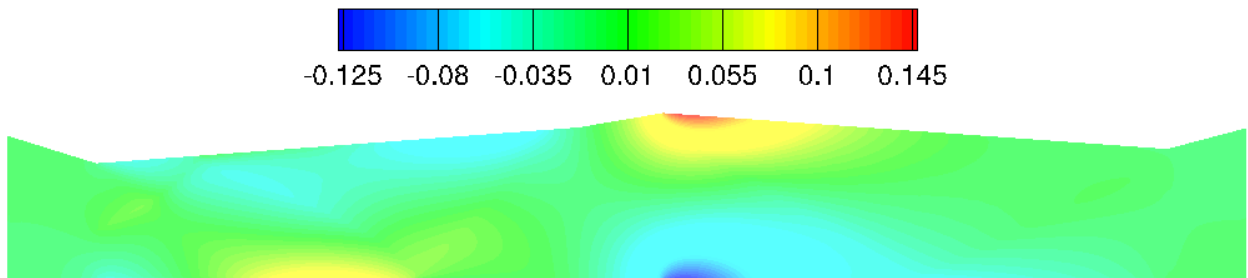


Figure 70. 3D MHD energy bypass scramjet engine:
 x -component of the induced magnetic field (T) b_x .

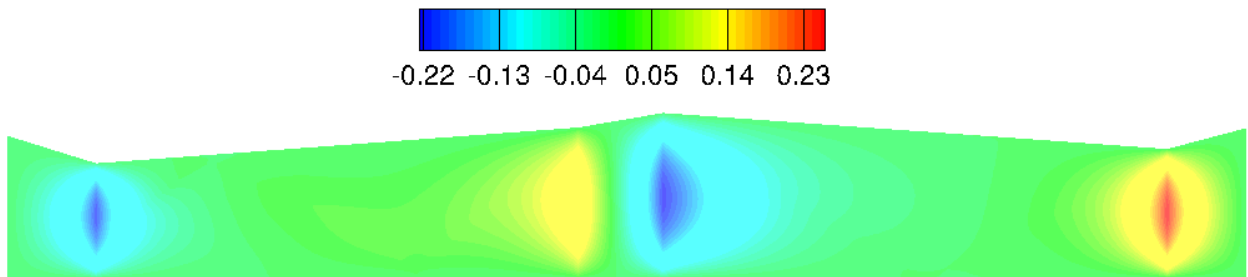


Figure 71. 3D MHD energy bypass scramjet engine:
 y -component of the induced magnetic field (T) b_y .

6 Conclusion and Suggested Future Developments

As part of a sustained effort to create HALO3D, an all-Mach number CFD code capable of simulating non-equilibrium effects, turbulence, Stuart, and more, the present work presents a robust and accurate loosely-coupled solver for magnetohydrodynamic equations at high Mach numbers. Two models are developed with the magnetic Reynolds number determining their applicability. The resistive MHD model makes use of the MHD assumptions and yields a coupled system composed of the RANS and magnetic induction equations. The low-magnetic Reynolds number formulation neglects the induced magnetic field and replaces the magnetic induction equation with the current-continuity equation, cast in terms of a scalar electric potential. These equations, written in conservative form, are discretized via an edge-based FE formulation in which the shape function coefficients associated with the geometrical features of the mesh need to be computed only once in the pre-processing phase of the solution procedure. To stabilize convection-dominated regimes, the inviscid fluxes are discretized with the Roe formulation, and second order accuracy is obtained through a MUSCL reconstruction of the primitive variables at the midpoints of the edges and a standard 1D van Albada slope limiter. The linear system is solved using the GMRES method with an ILU preconditioner. Various two and three-dimensional numerical simulations on both structured and unstructured grids are presented.

The solver for the current-continuity equation is first validated by simulating ionized flow through singly-paired segmented electrodes. The results shown are in good agreement with the literature. After the validation step, the coupled solver is used to simulate inviscid and laminar flows over a sphere, turbulent flows over an Apollo re-entry capsule and an OREX re-entry vehicle. Numerical results show that in all cases the flow features are changed by the imposed magnetic field. When the Stuart number St gradually grows from 0 to 6, the inviscid and viscous flows over a sphere witness an increase in shock standoff distance of more than 70%, and the Apollo capsule problem also sees an increase of 27%. Moreover, it is put into evidence that the peak heat flux decreases as well (13% for the viscous flow over a sphere problem and 16% for the Apollo problem). An investigation on the effects of the induced electric field is also performed. The induced electric field is nontrivial in regions adjacent to the object and in general enhances the MHD heat-shield phenomenon. Therefore, it is suggested that the induced electric

field must be taken into account by solving the current continuity equation and subsequently taking the gradient of the calculated electric potential.

The magnetic induction solver is validated through the Hartmann flow by comparing numerical results with analytical solutions. Results have also been obtained for a converging channel accelerator, a two-dimensional MHD energy bypass scramjet engine assuming inviscid flow and a three-dimensional energy bypass scramjet engine with viscous flow. The numerical results show, in all cases, how the flow characteristics are changed by the presence of the interaction between the magnetic and electric fields. For the Hartmann flow the braking effect of the Lorentz force is put into evidence, as well as the evolution of the hydrodynamic Hartmann layers and their magnetic signature. For the converging channel accelerator, the results demonstrate the accelerating effect of the electromagnetic force. For the entrance conditions retained for the computations, the acceleration ratio is 1.96.

An anisotropic grid optimization technique is studied on unstructured grids and it is found that grid optimization is crucial to retrieve accurate solutions with constrained mesh size. Some key features are:

- (1) The process is automated. No matter what initial grid is used (and as a matter of fact what algorithm the user has chosen), this methodology delivers the same solution of superior multi-scale resolution without necessarily increasing the grid size. Gao *et. al.* studied the dependency of initial grids by comparing the optimization outcomes (with a target of 1 million nodes) of 3 unstructured grids with 1/2, 1 and 2 million nodes (coarse, medium and fine), respectively [60]. All 3 grids demonstrated similar node distribution, despite the observation that the medium grid deployed more nodes near the shock. It was worth noting that the solution computed on these optimal grids of roughly 1 million nodes, was nearly identical to the solution computed on the structured grid of 20 million nodes, except for slight differences near the shock.

In non-trivial problems, the location of the salient flow features is not necessarily known a priori. Grid optimization effectively identifies these regions while locally optimizing the grid to resolve them. The sensitivity of the solution to user input is thus minimized. The grid-shock alignment (along with the alignments with other salient physical features) achieved by this optimization technique is extremely tedious or even impossible if not automated. A

structured grid, at its best, can be aligned with a simple shock system for a simplified geometry, assumed that the needed resources are at the user's disposal.

(2) Wall quantities such as the heat flux are indirectly, yet dramatically, improved by the resulting increased shock resolution.

(3) Unlike gradient-based grid optimizers, this methodology brings in a crucial directional effect based on the Hessian of the solution. The tetrahedral elements near the shock are elongated and aligned to the shock. The extremely elongated edges in the optimal grids are not only acceptable, but also necessary to capture shocks with superior resolution [82]. While order of accuracy is a major concern for structured grids dealing with smooth fields, it is less relevant for anisotropic unstructured grids resolving discontinuities that mandate first order techniques to introduce artificial viscosity. As is shown in Subsection 5.3 for a complex multi-shock system in a scramjet engine, an optimal unstructured grid of 8000 nodes produces, effortlessly, a more accurate solution than a structured grid of 57,000 nodes.

(4) Recently many research efforts have been dedicated to high-order methods (*e.g.* discontinuous Galerkin) and some advances have been reported in the high-Mach number regime [88, 89]. However, to the best of the author's knowledge, almost all of the reported results are limited to simplified 1D or 2D geometries employing mostly structured grids, and none has demonstrated comparable sophistication as the proposed methodology. Furthermore, Habashi *et. al.* pointed out that most well-posed stable numerical schemes, be they of first or second order, give practically the same answers on optimal grids [59]. The author believes that CFD practitioners should be more confident in using grid optimization, together with simpler schemes with guaranteed order of accuracy to pursue more accurate results, rather than resorting to overly complicated higher-order methods.

Moreover, the numerical results reveal that when heterogeneous physical quantities of different time/length scales reside in the solution, mesh optimization should respect their disparate time/length scales. Specifically, when the flow equations and the EM equations are coupled, the mesh optimization criteria should include both the flow field (ρ , p , V , T and/or μ_T) and the EM (φ or \mathbf{b}) variables. The results conclusively demonstrate that in hypersonic flow simulations it is not possible to heuristically generate meshes of sufficient quality to produce accurate results for both the flow and EM problems, and therefore anisotropic mesh optimization is an indispensable strategy that ought to be an integral part of credible hypersonic codes. The

results also show that for the same target number of nodes, optimization based on both the flow and EM solutions clearly outperforms that based on either alone. In addition, such noticeable increase in accuracy does not necessitate more mesh points, as gradient-based mesh enrichment would dictate.

Future developments can include the following aspects:

(1) The current hypersonic solver uses a loosely-coupled approach. This is an adequate approach at the beginning of the code development but has some disadvantages, such as stalls in the residuals and limitations on the CFL number, which suggest that fully coupling the solvers may improve convergence. Yet doing that would have the disadvantage that the modules are no longer portable;

(2) To simulate more complex and realistic physics, it is necessary to develop additional physical models, such as weak ionization and near-surface plasma sheath;

(3) During re-entry, the temperature on the surface of the vehicle may be over 2,000 K, necessitating a thermal protection system. MHD heat-shield concept is able to reduce the heat on the surface by slowing down the flow near the body using the Lorentz force induced by imposed magnetic field. Electron transpiration cooling is another approach that decreases the heat by emitting electrons from the hot leading edge. Accurate modeling of the coupling between those physical phenomena and the flow is required to reduce design margins, thus improving efficiency. In this respect, the hypersonic flow solver developed in this work can be used as a solid basis for such future developments.

References

1. Bisek, N.J., Boyd, I.D. and Poggie, J., *Numerical study of plasma-assisted aerodynamic control for hypersonic vehicles*. Journal of Spacecraft and Rockets, 2009. **46**(3): pp. 568-576.
2. Gaitonde, D.V., *A high-order implicit procedure for the 3-D electric field in complex magnetogasdynamic simulations*. Computers & Fluids, 2004. **33**(3): pp. 345-374.
3. D'Ambrosio, D. and Giordano, D., *Two-dimensional numerical methods in electromagnetic hypersonics including fully-coupled Maxwell equations*. AIAA Paper 2008-4013.
4. Poggie, J. and Gaitonde, D.V., *Magnetic control of flow past a blunt body: Numerical validation and exploration*. Physics of Fluids, 2002. **14**(5): pp. 1720-1731.
5. Laub, B. and Venkatapathy, E., *Thermal protection system technology and facility needs for demanding future planetary missions*. In International Workshop on Planetary Probe Atmospheric Entry and Descent Trajectory Analysis and Science. Noordwijk, Netherlands: ESA Publications Division, 2003: pp. 239-47.
6. Resler Jr., E., *The prospects for magneto-aerodynamics*. Journal of the Aerospace Sciences, 1958. **2**(9): pp. 25-235.
7. Cambel, A., Kranc, S. and Porter, R., *Electrodeless magnetogasdynamic power during entry*. Journal of Spacecraft and Rockets, 1967. **4**(6): pp. 813-815.
8. Ericson, W.B. and Maciulaitis, A., *Investigation of magnetohydrodynamic flight control*. Journal of Spacecraft and Rockets, 1964. **1**(3): pp. 283-289.
9. Boynton, J.H., *Experimental study of an ablating sphere with hydromagnetic effect included*. Journal of the Aerospace Sciences, 1960. **3**(27): pp. 306-307.
10. Postelnicu, A., *Influence of a magnetic field on heat and mass transfer by natural convection from vertical surfaces in porous media considering sores and dufour effects*. International Journal of Heat and Mass Transfer, 2004. **47**(6): pp. 1467-1472.
11. Hanquist, K.M., Alkandry, H. and Boyd, I.D., *Evaluation of computational modeling of electron transpiration cooling at high enthalpies*. Journal of Thermophysics and Heat Transfer, 2016. **31**(2): pp. 283-293.
12. Fomin, V., Tretyakov, P. and Taran, J.P., *Flow control using various plasma and aerodynamic approaches (short review)*. Aerospace Science and Technology, 2004. **8**(5): pp. 411-421.
13. Mason, W. and Lee, J., *Aerodynamically blunt and sharp bodies*. Journal of Spacecraft and Rockets, 1994. **31**(3): pp. 378-382.
14. N. Santos, W.F. and Lewis, M.J., *Aerothermodynamic performance analysis of hypersonic flow on power law leading edges*. Journal of Spacecraft and Rockets, 2005. **42**(4): pp. 588-597.

15. Shang, J., Hayes, J. and Menart, J., *Hypersonic flow over a blunt body with plasma injection*. Journal of Spacecraft and Rockets, 2002. **39**(3): pp. 367-375.
16. Girgis, I., Shneider, M. and Macheret, S., *Creation of steering moments in supersonic flow by off-axis plasma heat addition*. AIAA Paper 2002-0129.
17. Gnemmi, P., Charon, R. and Dup eroux, J.P., *Feasibility study for steering a supersonic projectile by a plasma actuator*. AIAA Journal, 2008. **46**(6): pp. 1308-1317.
18. Updike, G.A., Shang, J. and Gaitonde, D.V., *Hypersonic separated flow control using magneto-aerodynamic interaction*. AIAA Paper 2005-164.
19. Bityurin, V. and Vatazhin, A., *Hypersonic flow past the spherical nose of a body in the presence of a magnetic field*. Fluid Dynamics, 2004. **39**(4): pp. 657-666.
20. Ben Salah, N., *A finite element method for the fully-coupled magnetohydrodynamics*. Ph.D. Thesis, Concordia University, Montreal, QC, Canada, 1999.
21. Park, C., Bogdanoff, D. and Mehta, U., *Theoretical performance of a nonequilibrium MHD bypass scramjet*. AIAA Paper 2001-0792.
22. Kim, M., Keidar, M. and Boyd, I.D., *Analysis of an electromagnetic mitigation scheme for reentry telemetry through plasma*. Journal of Spacecraft and Rockets, 2008. **45**(6): pp. 1223-1229.
23. Macheret, S.O., Shneider, M.N. and Candler, G.V., *Modeling of MHD power generation on board reentry vehicles*. AIAA Paper 2004-1024.
24. D'Ambrosio, D. and Giordano, D., *Electromagnetic fluid dynamics for aerospace applications*. Journal of Thermophysics and Heat Transfer, 2007. **21**(2): pp. 284-302.
25. Thompson, R.J., Wilson, A., Moeller, T. and Merkel, C.L., *Advected upstream splitting method for the coupled Maxwell and Navier-Stokes equations*. AIAA Journal, 2014. **53**(3): pp. 638-653.
26. Khan, O.U., Hoffmann, K.A. and Dietiker, J.F., *Validity of low-magnetic Reynolds number formulation of magnetofluid dynamics*. AIAA Paper 2008-4013.
27. Bush, W.B., *Magnetohydrodynamics-hypersonic flow past a blunt body*. Journal of Aerospace Science, 1958. **25** (11): pp. 685-690.
28. Coakley, J.F. and Porter, R.W., *Time-dependent numerical analysis of MBD blunt body problem*. AIAA Journal, 1971. **9**(8): pp. 1624-1626.
29. Ziemer, R.W., *Experimental investigation in magneto-aerodynamics*. ARS Journal, 1959. **29**(9): pp. 642-647.
30. Bulen, A., Kranc, S. and Nowak, R., *Magnetogasdynamic re-entry phenomena*. Journal of Spacecraft and Rockets, 1967. **4**(11): pp. 1538-1542.
31. Kimmel, R.L. and Hayes, J., *Supersonic plasma flow control experiments*. Air Force Research Lab Wright-Patterson AFB OH Air Vehicles Directorate, December 2005.
32. Lineberry, J., Bityurin, V. and Bocharov, A., *Cylinder with current in hypersonic flow*. In Proc. 3rd Workshop on Magneto-Plasma Aerodynamics in Aerospace Applications, Moscow, Russia: pp. 15-25, 2001.

-
33. Gülhan, A. and Esser, B., *Experimental verification of heat-flux mitigation by electromagnetic fields in partially-ionized-argon flows*. Journal of Spacecraft and Rockets, 2009. **46**(2): pp. 274-283.
 34. Palmer, G., *Magnetic field effects on the computed flow over a Mars return aerobrake*. Journal of Thermophysics and Heat Transfer, 1993. **7**(2): pp. 294-301.
 35. Gaitonde, D.V. and Poggie, J., *Simulation of magnetogasdynamic flow control techniques*. AIAA Paper 2000-2326.
 36. Páscoa, J, Bròjo, F. and Monteiro, J., *Numerical simulation of magneto-plasma thrusters for aerospace propulsion using an MHD formulation*, In Proceedings of the 14th International Conference on Emerging Nuclear Energy Systems, Lisbon, Portugal, 2009.
 37. Chelem, C. and Groll, R., *Magneto-plasma dynamic thruster modelling with coaxial induced magnetic field*, International Journal of Computational Methods and Experimental Measurements, 2016. **4**(4): pp. 380-392.
 38. Xisto, C.M., Páscoa, J.C. and Oliveira, P.J., *A pressure-based high resolution numerical method for resistive MHD*. Journal of Computational Physics, 2014. **275**(1): pp. 323-345.
 39. Greenshields, C.J., Weller, H.G., Gasparini, L. and Reese, J.M., *Implementation of semi-discrete, non-staggered central schemes in a collocated, polyhedral, finite volume framework, for high speed viscous flows*. International Journal for Numerical Methods in Fluids, 2010. **63**(1): pp. 1-21.
 40. Dedner, A., Kemm, F., Munz, C.D., Schnitzer, T. and Wesenber, M., *Hyperbolic divergence cleaning for the MHD equations*, Journal of Computational Physics, 2002. **175**(1): pp. 645-673.
 41. Takeda, H. and Yamamoto, S., *Numerical investigation of supersonic MPD viscous flows with ionization*. Japanese Society of Mechanical Engineering International Journal Series B Fluids and Thermal Engineering, 2002. **45**(2): pp. 97-101.
 42. Miki, K., Schulz, J. and Menon, S., *Large-eddy simulation of equilibrium plasma-assisted combustion in supersonic flow*. In Proceedings of the Combustion Institute, **32**, 2009: pp. 2413-2420.
 43. Bobashev, S.V. and Golovachov, Y.P., *Deceleration of supersonic flow by an applied magnetic field*. Journal of Propulsion and Power, 2003. **19**(4): pp. 538-546.
 44. MacCormack, R.W., *Flow simulation within strong magnetic fields*. AIAA Paper 2008-1070.
 45. MacCormack, R.W., *Numerical simulation of aerodynamic flow including induced magnetic and electric fields*. AIAA Paper 2008-4010.
 46. Scalabrin, L.C. and Boyd, I.D., *Development of an unstructured Navier-Stokes solver for hypersonic nonequilibrium aerothermodynamics*. AIAA Paper 2005-5203.
 47. Ait-Ali-Yahia, D. and Habashi, W.G., *Finite element adaptive method for hypersonic thermochemical nonequilibrium flows*. AIAA Journal, 1997. **35**(8): pp. 1294-1302.

-
48. Cristofolini, A., Latini, C., and Borghi, C.A., *A weighted reverse Cuthill–McKee procedure for finite element method algorithms to solve strongly anisotropic electrodynamic problems*. Journal of Applied Physics, 2011. **109**(3): 033301.
 49. Nithiarasu, P., Zienkiewicz, Sai, B.V.K., Morgan, K., Codina, R. and Vazquez, M., *Shock capturing viscosities for the general fluid mechanics algorithm*. International Journal for Numerical Methods in Fluids, 1998. **28**(9): pp. 1325-1353.
 50. Selmin, V. and Formaggia, L., *Simulation of hypersonic flows on unstructured grids*. International journal for numerical methods in engineering, 1992. **34**(2): pp. 569-606.
 51. Scalabrin, L. and Boyd, I.D., *Numerical simulation of weakly ionized hypersonic flow for reentry configurations*. AIAA Paper 2006-3773.
 52. Candler, G.V., Mavriplis, D. and Trevino, L., *Current status and future prospects for the numerical simulation of hypersonic flows*. AIAA Paper 2009-153.
 53. Gnoffo, P.A. and White, J., *Computational aerothermodynamic simulation issues on unstructured grids*. AIAA Paper 2004-2371.
 54. Nompelis, I., Drayna, T. and Candler, G.V., *Development of a hybrid unstructured implicit solver for the simulation of reacting flows over complex geometries*. AIAA Paper 2004-2227.
 55. Mazaheri, A. and Kleb, B., *Exploring hypersonic, unstructured-grid issues through structured grids*. AIAA Paper 2007-4462.
 56. Gnoffo, P.A., *Multi-dimensional inviscid flux reconstruction for simulation of hypersonic heating on tetrahedral grids*. AIAA Paper 2009-599.
 57. Ching, E.J., Lv, Y., Gnoffo, P.A., Barnhardt, M. and Ihme, M., *Shock capturing for discontinuous Galerkin methods with application to predicting heat transfer in hypersonic flows*. Journal of Computational Physics, 2019. **376**(1): pp. 54-75.
 58. Bonfiglioli, A., Grottadaurea, M., Paciorri, R. and Sabetta, F., *An unstructured, three-dimensional, shock-fitting solver for hypersonic flows*. Computers & Fluids, 2013. **73**(1): pp. 162-174.
 59. Habashi, W.G., Dompierre, J., Bourgault, Y., Fortin, M. and Vallet, M-G., *Certifiable computational fluid dynamics through mesh optimization*. Special Issue on Credible Computational Fluid Dynamics Simulation, AIAA Journal, 1998. **36**(5): pp. 703-711.
 60. Gao, S., Seguin, J., Habashi, W.G., Isola, D. and Baruzzi, G.S., *A finite element solver for hypersonic flows in thermo-chemical non-equilibrium, Part II*. International Journal of Numerical Methods for Heat and Fluid Flow, Special Issue of the International Journal of Numerical Methods in Heat & Fluid Flow, Vol. 30, No. 2, pp. 575-606, September 2019.
 61. Ben Salah, N., Soulimani, A. and Habashi, W.G., *A finite element method for magnetohydrodynamics*. Computer Methods in Applied Mechanics and Engineering, 2001. **190**(43-44): pp. 5867-5892.

-
62. Baaziz, I., Ben Salah, N. and Kaddeche, S., *Magnetic control of natural convection in the horizontal Bridgman configuration: transversal plan*. International Journal of Computational Fluid Dynamics, 2014. **28**(6-10): pp. 339-350.
 63. Ben Salah, N., Baaziz, I., Rouse, D., Zlaoui, K. and Dutil, Y., *Magnetic control of natural convection in the horizontal Bridgman configuration: symmetric and non-symmetric cross sections*. International Journal of Computational Fluid Dynamics, 2011. **25**(3): pp. 127-138.
 64. Zhang, W., Habashi, W.G., Ben Salah, N., Isola, D. and Baruzzi, G.S., *Edge-based finite element formulation of hypersonic flows under an imposed magnetic field*. AIAA Journal, 2018. **56**(7): pp. 2756-2768.
 65. David, H., *Fundamentals of finite element analysis*. McGraw-Hill, USA, 2004.
 66. Kim, K.M., Gulhan, A. and Boyd, I.D., *Modeling of electron temperature in hypersonic flows*. AIAA Paper 2011-1028.
 67. Löhner, R. and Galle, M., *Minimization of indirect addressing for edge-based field solvers*. Communications in Numerical Methods in Engineering, 2002. **18**(5): pp. 335-343.
 68. Selmin, V., *The node-centred finite volume approach: bridge between finite differences and finite elements*. Computer Methods in Applied Mechanics and Engineering, 1993. **102**(1): pp. 107-138.
 69. Isola, D., *Equivalence conditions between continuous linear finite element and finite volume discretizations of non-simplicial elements*. AIAA Paper 2017-4276.
 70. Roe, P.L., *Approximate Riemann solvers, parameter vectors and difference schemes*. Journal of computational physics, 1981. **43**(2): pp. 357-372.
 71. Candler, G.V. and MacCormack, R.W., *Computation of weakly ionized hypersonic flows in thermochemical nonequilibrium*. Journal of Thermophysics and Heat Transfer, 1991. **5**(3): pp. 266-273.
 72. Lee, J.H., *Basic governing equations for the flight regimes of aeroassisted orbital transfer vehicles*. AIAA Paper 1984-1729.
 73. Gropp, W.D., Gropp, W., Lusk, E. and Skjellum, A., *Using MPI: portable parallel programming with the message-passing interface, Vol. 1*. MIT Press, USA, 1999.
 74. Schloegel, K. and Kumar, V., *Parmetis: parallel graph partitioning and sparse matrix ordering library*. Tech. Report 97-060, Department of Computer Science, University of Minnesota, Minneapolis, 1997.
 75. Balay, S., Adams, M.F., Brown, J., Brune, P., Buschelman, K., Eijkhout, V., Gropp, W.D., Kaushik, D., Knepley, M.G., McInnes, L.C., Rupp, K., Smith, B.F. and Zhang, H., *Petsc Web Page*. 2014; Available from: <http://www.mcs.anl.gov/petsc>.
 76. Saad, Y. and Schultz, M.H., *GMRES: a generalized minimal residual algorithm for solving nonsymmetric linear systems*. SIAM Journal on Scientific and Statistical Computing, 1986. **7**(3): pp. 856-869.

-
77. Barrett, R., Berry, M.W., Chan, T.F., Demmel, J., Donato, J., Dongarra, J., Eijkhout, V., Pozo, R., Romine, C. and Van der Vorst, H., *Templates for the solution of linear systems: building blocks for iterative methods*, 2nd edition. Philadelphia, PA: SIAM Press, 1994.
 78. Saad, Y., *Iterative methods for sparse linear systems*, 2nd edition. Philadelphia, PA: SIAM Press, 2003.
 79. Zheng, X., Lu, H., Xu, D. and Cai, G., *Numerical simulation of 2D supersonic magnetohydrodynamic channel and study on Hall effect*. Chinese Journal of Aeronautics 2011. **24**(2): pp.136-144.
 80. Bisek, N., *Numerical study of plasma-assisted aerodynamic control for hypersonic vehicles*. Ph.D. dissertation, University of Michigan, USA, 2010.
 81. Habashi, W.G., Dompierre, J., Bourgault, Y., Ait-Ali-Yahia, D., Fortin, M. and Vallet, M-G., *Anisotropic mesh adaptation: towards user-independent, mesh-independent and solver-independent CFD solutions: Part I: general principles*. International Journal for Numerical Methods in Fluids, 2000. **32**(6): pp. 725-744.
 82. Dompierre, J., Vallet, M-G., Bourgault, Y., Fortin, M. and Habashi, W.G., *Anisotropic mesh adaptation: towards user-independent, mesh-independent and solver-independent CFD solutions: Part III: unstructured grids*. International Journal for Numerical Methods in Fluids, 2002. **39**(8): pp. 675-702.
 83. Wright, M.J., Prabhu, D.K. and Martinez E.R., *Analysis of Apollo command module afterbody heating Part I: AS-202*. Journal of thermophysics and heat Transfer, 2006. **20**(1): pp. 16-30.
 84. Yamamoto, Y. and Yoshioka, M., *CFD and FEM coupling analysis of OREX aerothermodynamic flight data*. AIAA Paper 1995-2087.
 85. Moreau, R., *Magnetohydrodynamics*. Springer Science & Business Media, Netherland, 1990.
 86. Bityurin, V.A. and Bocharov, A.N., *MHD heat flux mitigation in hypersonic flow around a blunt body with ablating surface*. Journal of Physics D: Applied Physics, 2018. **51**(26): p. 264001.
 87. Bityurin, V.A. and Bocharov, A.N., *Ground MHD experiments in hypersonic flows*. High Temperature, 2010. **48**(6): pp. 874-880.
 88. Ching, E.J., Lv, Y., Gnoffo, P., Barnhardt, M. and Ihme, M., *Shock capturing for discontinuous Galerkin methods with application to predicting heat transfer in hypersonic flows*. Journal of Computational Physics, 2019. **376**(1): pp.54-75.
 89. Ciucă, C., Fernandez, P.A., Christophe, A.L., Nguyen, N.C. and Peraire, J.A., *Implicit hybridized discontinuous Galerkin methods for compressible magnetohydrodynamics*. Journal of Computational Physics: X, 2020. **5**(1): 100042.

Appendix A: Vector and Tensor Identities

The inner product between two vectors is defined as

$$\mathbf{x} \cdot \mathbf{y} = \sum_{i=1}^3 x_i y_i \quad (0.1)$$

where \mathbf{x} and \mathbf{y} are two vectors, x_i and y_i are components of \mathbf{x} and \mathbf{y} , respectively.

The inner product between a vector and a second-order tensor is defined as

$$(\mathbf{x} \cdot \mathbf{T})_j = \sum_{i=1}^3 x_i T_{ij} \quad (0.2)$$

where \mathbf{x} is a vector, \mathbf{T} is a second-order tensor, x_i and T_{ij} are components of \mathbf{x} and \mathbf{T} , respectively.

The column product between two second-order tensors \mathbf{T} and \mathbf{S} is defined as

$$\mathbf{T} : \mathbf{S} = \sum_{i=1}^3 \sum_{j=1}^3 T_{ij} S_{ij} \quad (0.3)$$

where T_{ij} and S_{ij} are components of \mathbf{T} and \mathbf{S} , respectively.

The L_2 norm of a vector \mathbf{R} is defined as

$$|\mathbf{R}|_{L_2} = \sqrt{\sum_i R_i^2} \quad (0.4)$$